Temporal variability of the Earth's magnetic field and its influence on the near-Earth space environment

Olga Tsareva

Université Fédérale
Toulouse Midi-Pyrénées

THÈSE

En vue de l'obtention du

DOCTORAT DE L'UNIVERSITÉ DE TOULOUSE

Délivré par l'Université Toulouse 3 - Paul Sabatier

Cotutelle internationale : Institut de recherche spatiale de l'Académie des sciences de Russie (IKI RAN)

Présentée et soutenue par

Olga TSAREVA

Le 26 juin 2020

Variabilité temporelle du champ magnétique terrestre et son influence sur l'environnement spatial proche

---

Ecole doctorale : **SDU2E - Sciences de l'Univers, de l'Environnement et de l'Espace**

Spécialité : **Astrophysique, Sciences de l'Espace, Planétologie**

Unité de recherche :
IRAP - Institut de Recherche en Astrophysique et Planetologie

Thèse dirigée par
Philippe LOUARN, Helmi Malova et Gabriel FRUIT

Jury

M. Roch SMETS, Rapporteur
M. Matteo FAGANELLO, Rapporteur
M. Christian JACQUEY, Examinateur
M. Lev ZELENYI, Examinateur
M. Victor POPOV, Examinateur
M. Philippe LOUARN, Directeur de thèse
Mme Helmi MALOVA, Directrice de thèse
M. Gabriel FRUIT, Co-directeur de thèse

UNIVERSITY OF TOULOUSE III – PAUL SABATIER

SPACE RESEARCH INSTITUTE OF RUSSIAN ACADEMY OF SCIENCES

DISSERTATION

submitted in partial satisfaction of the requirements
for the degree of

DOCTOR OF PHILOSOPHY

in Astrophysics

by

Olga TSAREVA

30 June 2020

Temporal variability of the Earth's magnetic field and its influence on the near-Earth space environment

Paul Sabatier Toulouse III University supervisor: Philippe LOUARN
IKI RAS supervisor: Helmi MALOVA

DISSERTATION COMMITTEE:

M. Philippe Louarn, Directeur de thèse
M. Gabriel Fruit, Co-directeur de thèse
Mme Helmi Malova, Directrice de thèse
M. Christian Jacquey, Examinateur
M. Victor Popov, Examinateur
M. Lev Zelenyi, Examinateur
M. Matteo Faganello, Rapporteur
M. Roch Smets, Rapporteur

ACKNOWLEDGMENTS

I would like to express my sincere gratitude to my supervisor Dr. Philippe LOUARN for the continuous support of my Ph.D study and related research, and also for help with funding and placement to complete the dissertation. My sincere thanks also goes to my co-supervisor Dr. Gabriel FRUIT for his help from the first day in new country and my co-author Dr. Christian JACQUEY for his help with satellite data. I thank my colleagues and co-authors Dr. Victor POPOV, Dr. Lev ZELENYI and especially my second supervisor Dr. Helmi MALOVA for goal setting. Without involvement and assistance of all these people in every step throughout the process, this thesis would have never been accomplished.

I thank my Reviewers Dr. Roch SMETS and Dr. Matteo FAGANELLO for their comments and advices on this manuscript.

My special thanks to Dr. Elena GRIGORENKO who provided me an opportunity to join new team and get a scholarship. And I'm also very grateful to Dr. Anatoly and Tatiana TUR for supporting me.

This research was supported by Vernadsky Fundation and CNRS.

TABLE OF CONTENTS

LIST OF FIGURES

LIST OF TABLES

Chapter 1

Introduction

Earth has been known to produce a permanent magnetic field since the most ancient times. Since the 12th century, it was used via the compass by the sailors to help them finding their way. In the 16th century, William Gilbert, in his book "De Magnete", hypothesized that the Earth is a magnet whose poles coincide with geographic poles. Knowledge of terrestrial magnetism increased at the end of the 18th century through many observations which were carried out both in observatories and on research trips. In 1834, Carl Friedrich Gauss gave a mathematical description of the Earth's magnetic field as a function of coordinates, using the development of spherical functions, which is still used today.

As technology progressed on, it was realized that the geomagnetic field is not stable and undergoes changes on time scales from milliseconds to millions of years. Short-term changes are largely driven by solar activity. They arise due to currents in the ionosphere (electrojet) and magnetosphere and can be traced to geomagnetic storms or substorms. These rapid changes in magnetic topology (magnetospheric reconfiguration) lead to spectacular auroral activity occurring within a few tens of seconds. The long-term changes in the geomagnetic field mostly reflect changes in the Earth's core. The longest global changes are geomagnetic reversals occurring almost randomly in time, with intervals between reversals varying from 0.1 to 50 million years. Moreover, the process itself from start to finish takes several thousand years (from 2 to 12 thousand years).

The thesis is divided into two main parts. The first part, prepared jointly with my French colleagues, is devoted to a new theory of magnetospheric instability, which can cause substorms. The second part, completed together with my Russian colleagues, tells about the radiation environment during the geomagnetic reversal.

An outstanding question in space physics is the cause of magnetospheric substorms (Akasofu, 1964). A substorm is a short disturbance of the magnetosphere, larging a few hours,

during which magnetic energy is released in the tail and this also produces beam of particles precipitating in the high latitude ionosphere. It is considered that substorms in the planetary magnetospheres are triggered by instabilities developing within the magnetotail current sheet over short time scales and contributing to the explosive release of magnetic energy into heat or accelerating plasma beamlets. But the detailed mechanism of this energy conversion is still unclear.

For more than thirty years, most of the work on thin current sheets has focused on magnetic reconnection and tearing instabilities. However, it is clearly seen from in-situ observations (by THEMIS) in the near-Earth magnetotail, closer than 10 RE, that magnetospheric reconfiguration (dipolarization) can occur in a thin current sheet with a significant normal magnetic field component, strong enough to eliminate magnetic reconnection and tearing instability as the causes (Lui, 1991; Zelenyi *et al.*, 1998). Thus, considering 1-D current sheets (with zero normal magnetic field) may be appropriate to the mid-tail environment with a vanishingly small normal magnetic field component but not to the near-Earth region.

The presence of a strong normal magnetic component B_z changes the particle dynamics and a reconfiguration of the magnetic topology is more difficult to explain using standard reconnection models. In the near-Earth magnetotail the plasma sheet electrons are trapped in the 2-D magnetic bottle formed by the quasi-dipolar field. They bounce back and forth with periods of a few tens of seconds coinciding with the periods of wave activity observed at substorm breakups. The electromagnetic fluctuations in a 2D current sheet may enter into resonance with the electron bounce motion. This wave/particle interaction in a mirror geometry, like the near Earth's magnetosphere, is obviously a non-local process that cannot be treated in the frame of fluid MHD. A new kinetic formalism based upon variational principle has been developed by Pellat *et al.* (1994) to show that low frequency electrostatic modes (frequency smaller than the average ion bounce frequency) are potentially unstable in a multipole-type configuration. The same approach was taken up by Le Contel *et al.* (2000) to describe self-consistently the radial transport of particles, i.e. a parallel electric field, developing in response to the quasi-static change of the magnetic field lines, associated with substorm growth phase (the beta of the plasma is assumed to be small). However, the variational principle does not allow to precisely describe unstable modes.

A first version of kinetic theory has been proposed by Tur *et al.* (2010) for the simplest electrostatic case. An explicit integration of perturbed Vlasov equation along the trajectories of the bouncing electrons allowed to express the non local disturbances in the electron distribution function. The ion response was considered as purely local. It was shown that a 2-D current sheet with an untrapped (passing) electron population is stable regarding electro-

static modes propagating in the direction of the current density, if the electron temperature is smaller than the ion one ($T_e < 0.5\ T_i$), i. e. the electron population is more reactive to compensate the ion perturbations and the system remains stable. If the passing electron population is partly or totally removed from the system, the current sheet becomes unstable. Thus boundary conditions at the end of the current sheet (at the ionosphere in the Earth magnetotail) are crucial to trigger or not a global instability.

This study was generalized to full electromagnetic perturbations by Fruit *et al.* (2013). They showed that in addition to the temperature ratio T_e/T_i, the stability of the current sheet also depends on the stretching parameter $\varepsilon = B_0/B_1$ of the magnetic topology (see Fig. 3.1). For mild stretching condition, the plasma sheet is stable, but as the stretching parameter ϵ decreases (< 0.063 for $Te/Ti = 0.25$), either due to a plasma sheet thinning or to a sudden increase in the magnetic pressure in the lobes, the current sheet becomes explosively unstable. The warmer the electrons are, the more sensitive the electron bounce instability is to the plasma sheet stretching.

The spatial non-homogeneities are well known to trigger various drift instabilities (Hasegawa, 1975), but they were not considered in previous works in order to concentrate on the analysis of the bounce effects. In the Earth magnetotail, the cross-tail current is mainly produced by diamagnetic drift effects due to a density gradient along the tail. In a low β regime, it is well known that a straight magnetic geometry with a perpendicular density gradient supports electromagnetic drift waves propagating perpendicular to both the magnetic field and the density gradient. They are called drift-Alfvén waves (Hasegawa, 1975; Mikhailovskii, 1998; Weiland, 2012).

The thesis aims to develop the electromagnetic drift-Alfvén wave theory taking into account the electron bounce motion in a magnetic bottle. Fruit *et al.* (2017) considered the electrostatic case of this problem and concluded that the presence of bouncing electrons that enter into resonance with the waves increases the growth rate of the classical universal instability (electrostatic drift instability).

Over the last 5 million years paleomagnetic studies based on the thermoremanent magnetization of massive materials have revealed about 20 polarity transitions (Vine & Matthews, 1963; Gubbins, 1994; Korte & Mandea, 2008), which implies a transition time scale of the order of 250 000 years. As the last one, the Matuyama–Brunhes reversal, occurred about 780 000 years ago, and its duration was 7 000 years. This means that humanity, as a species that arose 240 000 years ago, has never experienced geomagnetic reversals. Therefore, it is tempting to expect a further polarity transition geologically soon.

Based on observations, Earth's magnetic field is currently weakening and the magnetic poles are shifting. The migration rate of the magnetic pole towards the geographic north was about 15 – 20 km per year at the end of the XX century, but now it has grown to 55 – 60 km per year. The south magnetic pole is not moving as fast as the north one, but this process is noticeable. The magnetic dipole moment is showing a dramatic decrease with about a 9% decay since 1840 or a 30% decay over the past 2 000 years (Glassmeier *et al.*, 2009*a*,*b*; Glassmeier & Vogt, 2010; Olson & Amit, 2006). If the current decrease continues the geomagnetic dipole field will vanish in about 2000 years.

However, paleomagnetic studies show that about 12 000 years ago, the dipole moment was 50% higher than its current value. In addition, the actual field strength is maintained almost twice as long as the average field strength. And the present magnetic field is equal to the field in the middle of the Cretaceous, when it has not been annihilated for approximately 40 mln years. Between reversals, geomagnetic excursions also occur, which are short-term (5 – 10 thousand years) deviations of virtual geomagnetic poles at a distance of more than 45° from geographical one (Gubbins, 1999). However, during excursions, the geomagnetic field soon returns to its previous state. Over the past 1 million years, 14 excursions were discovered, six of which are considered global phenomena. Thus, the hypothesis of an approaching field reversal cannot be solved so far.

During the geomagnetic field reversal the surface magnetic field strength of the Earth decreases to about 10% or less of its current value. The dipole moment attenuates significantly, however the dynamo still generates magnetic field energy in higher order multipole moments (such as the quadrupole or octupole), i. e., create a field of more complex topology.

The absence of a dipole component means that the solar wind would approach much closer to the Earth. Cosmic-ray particles that are normally deflected by the Earth's field or are trapped in its outer portions reach the surface of the planet. These particles might cause genetic damage in flora and fauna, leading to the disappearance of one species and the appearance of another.

Numerous attempts have been made to find any correlation between geomagnetic polarity transitions and faunal extinctions (Uffen, 1963; Black, 1967; Watkins & Goodell, 1967; Wei *et al.*, 2014). Apparently, the causal connections between life and the geomagnetic field are indirect and involve chains of different processes (Simpson, 1966; Doake, 1978). So this problem was considered taking into account all factors determining the conditions for life on Earth (Glassmeier *et al.*, 2009*a*,*b*; Glassmeier & Vogt, 2010; Kirkby, 2007; Kirkby *et al.*, 2011). But the results remain inconclusive.

Uffen (1963) assumed that during a geomagnetic reversal period particles from the Sun

hitting Earth are barely deflected by the magnetic field, and these particles, together with particle precipitations from the Van Allen belts, would make further life on Earth impossible. However, Sagan (1965) argued against this possibility, because, even if a geomagnetic field was totally absent, no impact of energetic particles on the biosphere should be expected, since the atmosphere effectively absorbs the primary particles of solar and cosmic origin. This statement was confirmed by measurements in Glassmeier & Vogt (2010) revealing that at altitudes from 18 to 12 km above sea level the equivalent radiation dose due to cosmic particles decreases by about a factor of two, and at altitudes from 12 to 6 km it decreases by about a factor of $7 - 10$. Therefore, the atmosphere plays the role of a reliable shield against primary cosmic particles.

However, atmospheric screening is not yet perfect; especially when it is depleted. McCormac & Evans (1969) discussed the effects of very small planetary moments on the atmosphere of planets, in particular, Venus and Mars. They pointed to the possibility of complete erosion of the atmosphere as a result of its direct interaction with the solar wind in the absence of any significant magnetic field of the planet. Wei *et al.* (2014) propose that the geomagnetic reversal could enhance the oxygen escape rate from the atmosphere and led to the catastrophic drop of its level, which can be a cause of Triassic - Jurassic extinction event.

Original hypothesis of Uffen (1963) based on the assumption that particles of the radiation belt spill into the atmosphere can also be rejected by comparing the corresponding time scales: typical residence times of energetic particles in the inner belt are of the order of years, which is very short compared with the duration of a reversal. Glassmeier & Vogt (2010) assumed that magnetic trapping of energetic particles during a polarity transition is difficult to achieve. Radiation belts, if they exist at all, should be less well developed than in the present-day dipolar configuration. Similar to the statement of Lemaire & Singer (2012) that during a reversal, the particles of highest energies trapped by radiation belts being lost first and their energy spectra become softer.

The consequences of geomagnetic reversal could also include, in addition to higher radiation dose, ozone layer exhaustion (Sinnhuber *et al.*, 2003; Melott *et al.*, 2005; Vogt *et al.*, 2007; Winkler *et al.*, 2008) and various climatic changes on Earth (Kirkby, 2007; Svensmark & Friis-Christensen, 1997).

Changes in the radiation situation on Earth, the radiation belts and the terrestrial atmosphere during the a reversal remain open issues to which a significant part of this dissertation is devoted.

Chapter 2

Earth's Magnetosphere

The bullet shaped magnetic bubble formed by the interaction of a stream of charged particles of solar wind with a magnetic field is called the magnetosphere. Into the space vacuum, the magnetosphere extends from about 60 000 km sunward and trails out more than 300 000 km away from the Sun in the magnetotail.

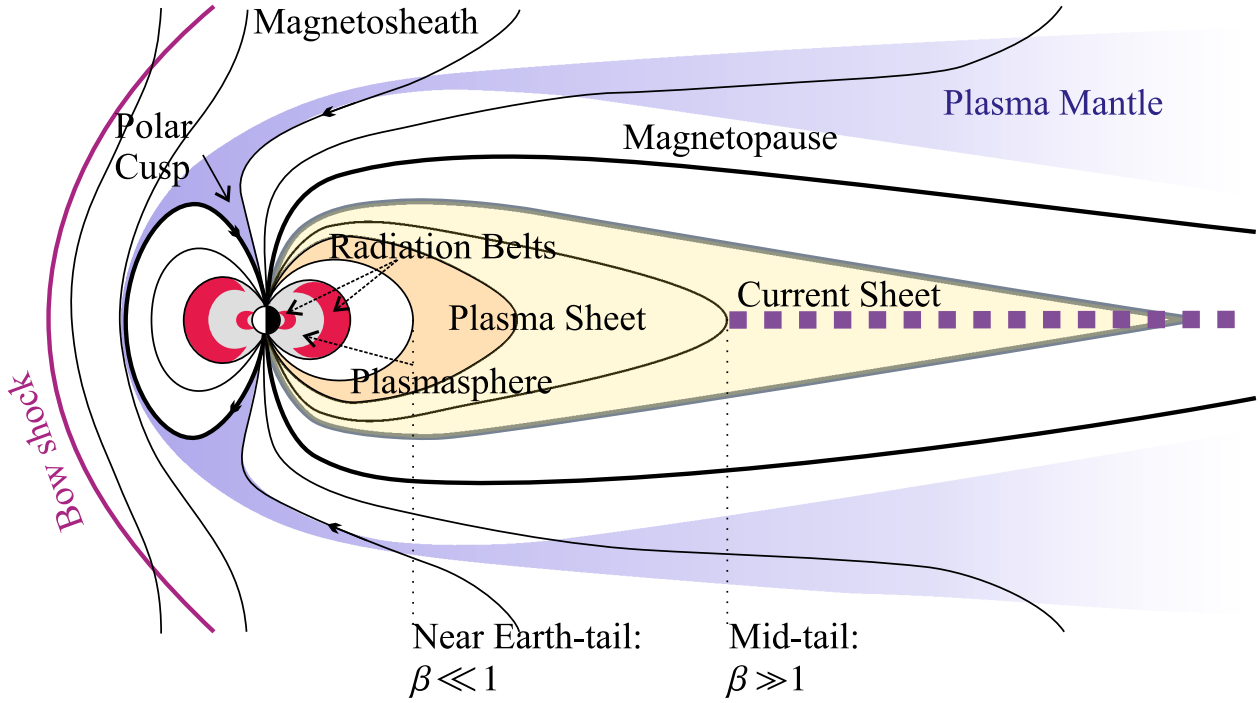

Figure 2.1: The configuration of the Earth's magnetosphere

The boundary between the planet's magnetic field and the solar wind is **the magnetopause**. It's location is determined by the balance between the dynamic pressures of the planetary magnetic field and the solar wind.

The magnetotail is the elongated magnetic field in the antisunward direction, it contains the northern and southern tail lobes with few charged particles. The two lobes are separated by **a plasma sheet**, an area where the magnetic field is weaker, and the density of charged particles is higher.

The bow shock is the shock wave generated by the solar wind, which is decelerated from supersonic to subsonic speed in front of the magnetosphere. The zone of shocked solar wind plasma is **the magnetosheath**. The solar wind plasma entering the magnetosphere forms **the plasma sheet**. The amount of solar wind plasma and energy entering the magnetosphere is controlled by the orientation of the interplanetary magnetic field (IMF), which is embedded in the solar wind.

The two **Van Allen radiation belts** are concentric, tyre-shaped belts (shown in red Fig. 2.1) of highly energetic electrons and protons trapped by the magnetic field. The inner belt is located between 1–2 Earth radii (R_E) above Earth's surface, although it is much closer over the South Atlantic. The main contribution to the radiation of the inner belt is made by protons with an energy of 1-10 MeV. The external radiation belt is located at altitudes of about 4 to 7 R_E. And the particles that contribute to the most energetic fluxes are electrons with energies of 0.1-1 MeV. Both belts are separated from each other by an empty "slot" region. NASA's Van Allen Probes (2013) detected a temporary third belt, between the slot and the outer main belt.

The filling of radiation belts can proceed slowly and continuously as a result of neutron decay of the GCR albedo, the flux of secondary particles reflected from the Earth's atmosphere, (with energies $E_p > 30$ MeV) or quickly ("pulsed") as a result of the transfer and acceleration of charged particles in the magnetosphere under the influence of various non-stationary processes: perturbations of electric and magnetic fields, quasiperiodic disturbances, dipolization of force lines, or due to dynamic changes in the dayside magnetopause. Particle injection into radiation belts can occur due to fast convection during magnetospheric substorms, and their acceleration is due to the resonance between the azimuthal drift around the Earth and perturbations of the large-scale electric field during substorms.

For protons and ions of radiation belts, the main mechanism of losses on magnetic shells $L > 4$ (corresponds to the set of the Earth's magnetic field lines, crossing the Earth's magnetic equator at a specified distance in R_E) is the ionization loss due to interaction with the upper atmosphere. The main cause of electron escape in the inner belt $L < 1.5$ is Coulomb scattering, the electrons in the outer belt $L > 3$ are lost due to cyclotron instability, and the "slot" between the belts is due to electron scattering by low-frequency electromagnetic radiation.

These radiation belts partly overlap with the plasmasphere.

The plasmasphere — the innermost part of the Earth's magnetosphere (shown in grey Fig. 2.1) — is a doughnut-shaped region of low energy charged particles (cold plasma) centred around the planet's equator and rotating along with it. Its toroidal shape is determined by the magnetic field of Earth. The plasmasphere begins above the upper ionosphere and extends outwards to plasmapause — the outer boundary of the plasmasphere varies (depending on geomagnetic conditions) from 4.5 R_E to 8 R_E. During periods of low geomagnetic activity the plasmapause typically extends to around 6 R_E, occasionally expanding beyond the boundary of the outer radiation belt, as far as 8 R_E or even further. During periods of higher geomagnetic activity the plasmapause moves closer to the inner boundary of the outer belt, to around 4.5 R_E.

The cusps — two weak points in Earth's defences — occur above the planet's north and south magnetic poles. Particles from the solar wind which leak into the magnetosphere spiral down towards the Earth along magnetic field lines. Cusps are responsible for dayside auroral precipitation.

2.1 Steady magnetic field

Earth's magnetic field has three sources: an internal magnetic field, produced by currents in Earth's outer core, an external magnetic field, produced by currents in the magnetosphere and ionosphere, and an anomalous, induced magnetic field (remnant magnetization in the crust). Carl Friedrich Gauss (1832) concluded that more than 90% of Earth's magnetic field arises from internal planet sources, and 5% from external ones.

2.1.1 Internal sources: Geomagnetic dynamo

By the 40s last century, scientists formulated three conditions for the fluid motion producing a magnetic field. First, the fluid medium must be electrically conducting (the liquid iron in the outer core). Secondly, the motion of the liquid mass of the outer core is brought about by convection, i.e. heat moves upward from the inner core of Earth to the mantle. Thirdly, the Coriolis effect caused by the rotation of the Earth twists the rising liquid mass into a spiral. The interaction of the mechanical motions of the liquid medium and electric currents creates a self-sustaining magnetic field.

The simplest possible poloidal magnetic field is dipolar. Such a field could be produced by a single loop of electric current circulating around the Earth's rotation axis in the equatorial plane.

In 1958, T. Rikitake proposed a double-disk dynamo model consisting of two identical rotating conductive disks that simulate a convective cell or vortex in a liquid external core, inductively coupled to each other through solenoid loops. Their interaction leads to a redistribution of angular velocities and excited currents, and hence magnetic fields. Thus, magnetic reversal is simulated, which is impossible in the single-disk dynamo.

The most popular model is the $\alpha\Omega$-model Parker (1955), in which the magnetic field is decomposed into two components: poloidal and toroidal components. The poloidal component of the magnetic field is generated due to helical fluid motions (α-effect), and a differential rotation (Ω-effect) stretches field lines into the toroidal field (i. e. an azimuthal field, with respect to the rotation axis). Fluctuations of the α-effect allow one to obtain a chaotic change in the polarity of the magnetic field. Dynamo based solely on the α-effect is called the α^2-dynamo. Its almost stationary field is characterized by small short-term variations (hundreds of years for the Earth) and long-term complete reversals (millions of years). The presence of a weak Ω -effect is necessary to explain the physical nature of the observed drift of geomagnetic inhomogeneities and is caused by shear flows of a large-scale velocity field. There is a closed-loop of the magnetic fields' generation. If α and Ω are large enough and the inductive effect prevails over dissipation, then the magnetic field grows and the dynamo works.

According to the Glatzmaier & Roberts (1997) model, chaotic turbulent small-scale fluid motions in the core push out and twist magnetic lines. Due to the Earth's rotation, the loops of the magnetic lines are tightened and, at the core/mantle boundary, sections of the reversal magnetic field are formed. When the sections of the reverse magnetic field prevail over the areas with the original polarity, the magnetic reversal occurs. For the first time, Glatzmaier & Roberts (1995) successfully modeled the reversal using a supercomputer and obtained a complete solution of a complex system of hydromagnetic dynamo equations consisting of heat and mass transfer, Navier-Stokes, and Maxwell equations in a rotating spherical layer.

According to their numerical model, the beginning of the pole change is expressed as a drop of the dipole field strength. Sections of the reversal magnetic field appear, similar to those formed today at the core-mantle boundary. But instead of zeroing the magnetic field completely, these sections during the transition period create a weak field with heterogeneous polarity. In general, the disappearance of the former polarity and the emergence of a new one takes 9 000 years. However, a real change in the field occurs in a short period of time, approximately 2 000 years, when the dipole energy drops sharply by several orders of magnitude. Moreover, the higher multipole components do not exhibit such extreme behavior in their magnetic energies, but only fluctuate within an order of magnitude.

2.1.2 External sources: current in space

The electrical currents in the magnetosphere and ionosphere flow in large part due to the interaction of the terrestrial magnetic field with the solar wind and therefore depend on its properties. Solar wind pressure affects the size of the magnetosphere and the strength of the magnetopause currents. The strength and orientation of the interplanetary magnetic field (IMF) control the level of interconnection between the interplanetary medium and the terrestrial field and can modify the structure of and circulation within the magnetosphere. For example, a southward direction of the interplanetary magnetic field is critical to enabling reconnection with the dayside low-latitude magnetosphere, resulting in magnetic flux transfer to the magnetotail.

The magnetopause current system (Chapman-Ferraro current) limits the size of the magnetosphere and creates a closed magnetosphere (at least for northward IMF). The tail current differs from the magnetopause current because over part of its path it flows interior to the Earth's magnetic field. The region where this occurs is called **the current sheet**. The cross-tail current (related to the tail plasma sheet with closure via tail boundary current) is mainly produced by **diamagnetic drift effects** due to a density gradient along the tail.

2.1.3 Ring current

A ring current is an electric current carried by charged particles trapped in Earth's magnetosphere. The behaviour of trapped particles can be approximated by the superposition of three types of motion: gyration around field lines, "bounce" along field lines, and azimuthal drift in rings around the Earth.

Gyration is produced by the Lorentz force, which makes charged particles move in circles around magnetic field lines. Reflection of particles at the ends of field lines is caused by the converging geometry of a dipole field. As a gyrating charged particle approaches the Earth moving along a field line, the particle encounters a magnetic mirror that reflects it. Azimuthal drift is produced by two effects: a decrease in the strength of the main field away from the Earth and a curvature of magnetic field lines. Particles of opposite charge drift in opposite directions, i. e., protons gyrate in a left-handed sense and drift westward, while electrons gyrate in a right-handed sense and drift eastward. Since the particles drift in opposite directions, they produce an electric current in the same direction as the proton drift.

A collection of charged particles trapped in the Earth's inner magnetic field and drifting as described above constitutes **a Van Allen radiation belt**.

2.1.4 Field-aligned currents

A Birkeland current is a set of currents that flow along geomagnetic field lines connecting the Earth's magnetosphere to the Earth's high latitude ionosphere. The Birkeland currents occur in two pairs of field-aligned current sheets. The sheet on the high latitude side of the auroral zone is referred to as the Region 1 current sheet and the sheet on the low latitude side is referred to as the Region 2 current sheet. These two current sheets are caused by different physical mechanisms, but they are connected through the ionosphere and form a single circuit.

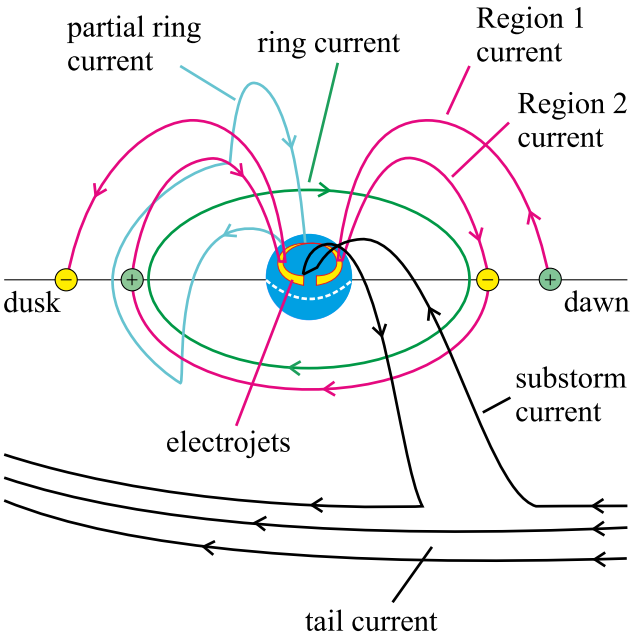

Figure 2.2: The the field-aligned current system consists of two oppositely directed, nearly parallel current sheets and drives a secondary ionospheric current system consisting of two convective electrojets.
The Region 1 current originates in the region of the interface between field lines dragged tailward by the solar wind and field lines returning to the dayside of the Earth. This interface is electrically charged — positive on the dayside and negative on the nightside of the Earth. The Region 2 current is a result of charge separation by drift in the main field.

The superposition of the Earth's main field, ring current, magnetopause current, and tail current produces a configuration of magnetic field lines quite different from that of the dipole field. On the dayside the field lines are compressed inside a boundary located typically at 10 Re. On the nightside the field is drawn out to distances probably exceeding 1 000 Re.

2.2 Variation in magnetic field

The field has variations on time scales from milliseconds to millions of years, but rapid changes mostly come from currents in the ionosphere and magnetosphere. The secular variation is the changes over periods of a year or more, reflecting changes in the Earth's core. Phenomena associated with this secular variation include geomagnetic jerk, westward drift and geomagnetic reversals.

2.2.1 Reversals of magnetic field

In 1906, geologist Bernard Brunhes first noticed that some volcanic rocks (from the Central Massif of France) were magnetized opposite to the direction of the local Earth's field. In the 1920s, Motonori Matuyama dated these rocks with reversed fields to the early Pleistocene age or older. In the 1950s, techniques for radiometric dating were improved and Cox & Doell (1960) produced the first magnetic polarity time scale. Later, Opdyke (1972) showed that the same pattern of reversals was recorded in sediments from deep-sea cores.

During the 1950s and 1960s, information of Earth's magnetic changes was mainly collected by research vessels. The obtained data plotted on a map allowed to detect remarkably regular and continuous magnetic stripes on the ocean floor. Vine & Matthews (1963) and Morley & Larochelle (1964) independently provided a simple explanation by combining the seafloor spreading theory of (Hess, 1962) with the known time scale of reversals.

The explanation for these strips is that molten basalt emerges from the ridge and spreads away symmetrically in both directions. As the basalt cools, it captures the orientation of the dominant magnetic field and carries it along on the spreading seafloor[1]. Basalt flowing out of the ridge and cooling at later times captures the subsequent field orientation. Thus the seafloor acts like a magnetic tape, capturing the alternating sequence of magnetic field orientations. Past magnetic field polarity can be inferred from data gathered from towing a magnetometer along the sea floor. (The age of any studied seafloor does not exceed 180 mln years.)

A similar technique was used to determine the virtual poles of the Earth from progressively older rocks. It revealed that the virtual poles wander over time. For many years it was thought that this "polar wandering" was a characteristic of the Earth's magnetic field. However it turned out that it evidences for continental drift. Not the magnetic poles have moved relative to the geographic poles, but the continents (Seyfert, 1987). The Morley-Vine-Matthews hypothesis was the first key scientific test of the seafloor spreading theory of continental drift. After it, the theory of plate tectonics was widely accepted.

Nowadays, it is considered proven that the Earth is changing the direction of its magnetic field. Moreover, the correlation between the frequency of polarity reversal and the tectonic activity of the planet is proved. It was found that during reversal, the magnetic field decreases significantly, but almost never vanishes. The value of the residual field is uneven on the earth's surface: it is noticeably higher in the regions of magnetic anomalies.

[1]Seafloor spreading is a process that occurs at mid-ocean ridges, where new oceanic crust is formed through volcanic activity and then gradually moves away from the ridge.

2.2.2 Geomagnetic storms

Geomagnetic storms are major magnetic disturbances occurring over several days, once or twice a month during the maximum solar cycle and several times a year during the solar minimum. They originate from the interaction between magnetosphere and coronal mass ejection (CME): large plasma bubble emitted by the sun. This has as a consequence to introduce a large number of ions into the external radiation belt and are observed from anywhere on Earth. During a storm, the intensity of the ring current increases substantially and causes perturbations of the magnetic field on average of about 100 nT.

2.2.3 Magnetospheric substorms

Magnetospheric substorm is a brief auroral and magnetic disturbance that causes energy to be released from the magnetotail and injected into the high latitude ionosphere. Substorms take place over a period of a few hours and often only a few hours apart from each other. Visually they are seen as a sudden brightening and increased movement of auroral arcs.

A substorm is traditionally divided into three phases: the growth phase, the expansion phase, and the recovery phase.

The growth phase indicates a progressive equatorward movement of the auroral oval and magnetospheric reconfiguration until the sudden onset of substorm expansions (McPherron, 1970). However, the growth phase is not a necessary substorm phase unless substorm is preceded by reconfiguration. The growth phase is terminated by the auroral breakup — a sudden brightening and activation of the most equatorward arc in the northern and southern auroral ovals.

The expansion and recovery phases reflect the poleward advance and retreat of auroral disturbance in the polar regions. Akasofu (1964) divided the expansion phase into two stages: Akasofu initial brigtening (AIB) expanding in longitude, followed by poleward expansion (PE) a few minutes later. The westward traveling surge decays into drifting bands. As the surge travels westward, there is also an enhancement of the westward electrojet. On the Earth the magnetic field suddenly decreases, sometimes up to a magnitude of 2 000 nT, which is about 3% of the total magnetic field strength in this area. The substorm expansion phase lasts about 20 min, then the final phase follows.

During the recovery phase, the brightness and strength of the aurora and currents decreases and they gradually return to their original equatorward locations.

In earlier studies, the magnetospheric substorm was explained in terms of magnetic convection driven by magnetic reconnection. Magnetic reconnection is a physical process that

may result from the development of some plasma instabilities. The Earth's magnetic field lines are merging with field lines of southward IMF. The joined field lines are swept back over the poles into the planetary magnetic tail. In the tail, the field lines from the planet's magnetic field are re-joined and start moving toward night-side of the planet (Dungey, 1961). The rate of reconnection at the dayside magnetopause exceeds the rate of magnetotail reconnection, which leads to the accumulation of energy in the magnetotail in the form of magnetic field energy. This stage of energy storage ends with the development of a tearing instability.

However, presently, due to on-site observations in the near-Earth magnetotail, there are the two primary substorm onset scenarios based on the magnetospheric location of its occurrence. Their common feature is the development of a thin current sheet in the magnetotail before the start of the expansion phase.

The mid-tail initiation scenario (Haerendel, 2000; Shiokawa *et al.*, 1997, 1998) included in near-Earth neutral line (NENL) model (Baker *et al.*, 1996) stems from the magnetic reconnection located at a distance of $\sim 15 - 30\ R_E$. Magnetic reconnection generate high-speed earthward plasma flow which is braked down by the strong magnetic field and high plasma pressure in the near-Earth region, producing an eastward inertial current to set up the substorm current wedge.

The near-Earth initiation scenario (Lui, 1991; Erickson, 1995; Roux *et al.*, 1991) with the process located at a distance of $\sim 6 - 15\ R_E$, deal with disrupting the cross-tail current in the inner plasma sheet due to some kind of instability. The current disruption (CD) model (Lui, 1996) realizing this scenario predicts that a signal on occurrence of current disruption is conveyed progressively tailward via rarefaction waves set off by plasma pressure reduction in the current disruption site. This correspondes to the poleward advance of the auroral bulge in the ionosphere (Liou *et al.*, 2002). A plasma sheet thinning and weakening may lead magnetic reconnection in the mid-tail region at a later time. But a statistical study of Miyashita *et al.* (2010) did not support the existence of rarefaction waves. Lui (2004); Rae *et al.* (2009); Kalmoni *et al.* (2015, 2017) also concluded that the near-Earth magnetotail is the source of the instability.

2.2.4 Plasma instabilities

When a space plasma is not in thermodynamic equilibrium, i. e., it is not homogeneous and does not have a Maxwellian velocity distribution, a certain amount of free energy is accumulated in the plasma and this energy can be converted into a violent plasma motion or into electromagnetic radiation.

The way a plasma can deviate from thermodynamic equilibrium has two origins:

- an anisotropy of the velocity distribution function that causses a microscopic instability;
- an inhomogeneity in pressure, density, temperature or another thermodynamic quantity that produce a macroscopic instability.

A similar distinction can be made concerning magnetohydrodynamic (MHD) instabilities and kinetic instabilities. MHD instabilities are usually associated with motions of macroscopic volumes of plasma and can be described with MHD equations. MHD instabilities that develop during a time substantially shorter or comparable with the characteristic time between particle collisions are subdivided into ideal or dissipative MHD instabilities. Kinetic instabilities essentially depend on difference in motions of different groups of particles in the same volume. These are microscopic in comparison to large-scale slow MHD motions.

A short list of some important groups of instabilities is given in Table 2.1.

Table 2.1: Some major groups of instabilities

	Electrostatic	Electromagnetic
Macroinstabilities (mainly MHD)	Current-pinch inst., Flute or interchange inst., Thermal inst., Rayleigh-Taylor inst.	Collision-free shock inst., Resistive tearing-mode inst., Sausage inst., Drift-wave inst., Collisionless tearing-mode inst.
Microinstabilities (mainly kinetic)	Two-stream and Beam-plasma inst., Ion-wave inst. Cyclotron inst., Loss-cone inst., Harris-type (velocity anisotropy) inst.	Alfvén-wave inst., Anisotropic-pressure inst., Mirror inst., Modulation inst.

As magnetospheric plasma pressure grows, the main role goes to MHD instabilities, which are powered by plasma's thermal energy. These are flute and ballooning modes, which are driven by internal pressure and magnetic field line curvature. The ballooning instability usually seen in tokamak fusion power reactors or in space plasmas acts like the elongations referred to as 'fingers' which are formed in a long balloon when it is squeezed. The narrow fingers of plasma produced by the instability are capable of accelerating and pushing aside the surrounding magnetic field in order to cause a sudden, explosive release of energy. A theoretical approach to the study of the ballooning instability is based on a complicated system of coupled equations for the poloidal Alfvén and slow magnetosonic waves bouncing back

and forth on a curved magnetic field line in a finite-pressure plasma. Favorable conditions for the instability growth emerge at a steep plasma pressure drop held by curved field lines.

The interchange instability is a type of plasma instability driven by the gradients in the magnetic pressure in areas where the confining magnetic field is curved. The name of the instability refers to the large-scale interchange motion of magnetic flux tubes without significant disturbance to the external field geometry. The instability causes flute-like structures oriented along the lines of force to appear on the surface of the plasma, and thus the instability is also known as the flute instability. The interchange instability is but a special case of the ballooning instability where the mode does not perturb the equilibrium magnetic field.

The simplest type of microscopic (kinetic) instability develops in the interaction of charged particle beams with plasma. This subclass of kinetic instability is called beam-plasma instability. It is easiest to interpret beam instability as the inverse of Landau damping effect, i. e. in the presence of a sufficiently intense electron beam in the plasma, the velocity distribution function has a second velocity maximum.

In our work, we mix both origins of instability: diamagnetic drift and electron bounce effects.

The Rayleigh–Taylor instability (Tab. 2.1) occurs at an interface between two fluids of different densities when the lighter fluid is pushing the heavier fluid. It can be electromagnetic if k has a finite component along B. The Rayleigh–Taylor instability is accompanied by the formation of the mushroom structures like those from volcanic eruptions and nuclear explosions. The Kelvin–Helmholtz instability occurs when there is a velocity shear in a single continuous fluid, or when there is a velocity difference across the interface between two fluids. This instability is responsible for some of nature's most basic structures, from waves in the ocean to clouds in the sky, and plays a major role at the magnetopause. When the two layers of the fluid are allowed to have a relative velocity, the instability is generalized to the Kelvin–Helmholtz–Rayleigh–Taylor instability.

Chapter 3

Electromagnetic drift instability

The problem of substorm dynamics is fundamentally electromagnetic in nature. The aim of this chapter is to introduce a self-consistent kinetic model that describes the resonant interaction between the bouncing electrons trapped in the Earths magnetic field and the electromagnetic perturbations created by particles themselves. This is continuation of the study of Fruit *et al.* (2017) which is limited to electrostatic disturbances. However, to make things simpler at first, the model is applicable to the Near-Earth magnetotail only where the parameter β may by assumed to be low. As a consequence, the compressional magnetic disturbanses may be negleted and we can work only with two electromagnetic variables: the electrostatic potential ϕ and the parallel magnetic potential $a_\parallel$. These two potentials are generated by a perturbed charge and parallel current density derived from the perturbed distribution functions. As noted by Le Contel *et al.* (2000), a parallel electric field affects the triggering process of auroras.

3.1 Theoretical formalism

3.1.1 Equilibrium state

The zero order state is a 2D current sheet in a low-β approximation. It aims to model the near-Earth plasma sheet at equatorial distances 8 - 12 R_E where the magnetic topology deviates substantially from the dipole field but it is not yet shaped as a stretched tail configuration. The magnetic geometry is described in a rectilinear frame (O, x, y, z) as shown in Figure 3.1, where the z-axis is south-north and the x, y-axis being in the plane defined by the current. As the plasma sheet is assumed to be invariant along the y direction, the particle distribution function depends only on the invariants of the particle dynamics, say the kinetic energy E

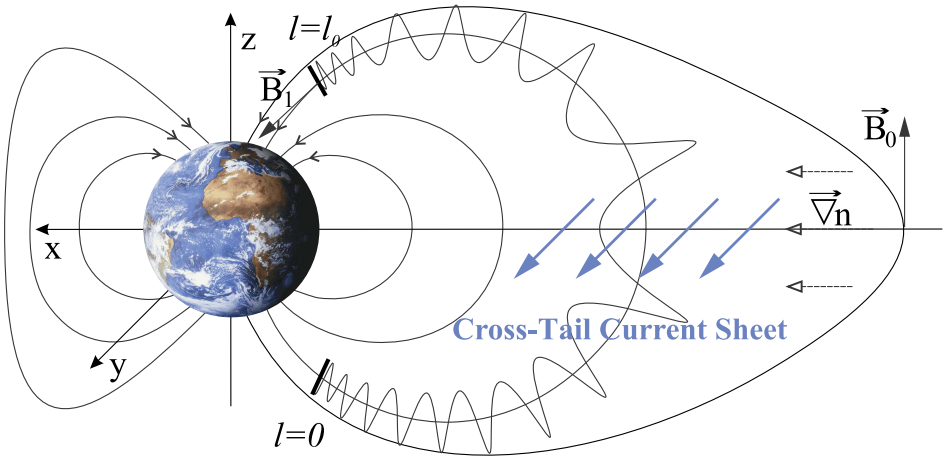

Figure 3.1: Geometry of magnetic field lines with length l_0 within a plasma sheet (dipolar model).

and the moment $P_y = mv_y + qA_y$; taking into account a diamagnetic drift in the direction of the current $\vec{u}_\alpha = u_\alpha \vec{e}_y$, a possible distribution function for each species α is

$$F_0^{(\alpha)}(\vec{r},\vec{v}) = n_0 \left(\frac{m_\alpha}{2\pi\, k_B T_\alpha}\right)^{3/2} \exp\left(\frac{-m_\alpha u_\alpha^2}{2k_B T_\alpha}\right) \times \exp\left(-\frac{E_\alpha - u_\alpha\, P_{y,\alpha}}{k_B T_\alpha}\right), \tag{3.1}$$

where m_α, T_α, q_α and n_0 are the mass, temperature, charge and density of species α.

With a magnetic potential $\vec{A} = \Psi(x,z)\,\vec{e}_y$ and introducing the thermal velocity for each species $V_\alpha = \sqrt{2k_B T_\alpha/m_\alpha}$, (3.1) can be rewritten as

$$F_0^{(\alpha)} = \frac{n_0(\Psi)}{\pi^{3/2}\, V_\alpha^3} \exp\left(-\frac{v_x^2 + (v_y - u_\alpha)^2 + v_z^2}{V_\alpha^2}\right). \tag{3.2}$$

with $n_0(\Psi) = n_0\, \exp(q_\alpha\, u_\alpha\, \Psi/(k_B T_\alpha))$. Charge neutrality at equilibrium imposes the relation

$$\frac{u_i}{k_B T_i} + \frac{u_e}{k_B T_e} = 0 \tag{3.3}$$

for a plasma composed of only one type of ions (protons) and electrons.

In principle, the magnetic potential $\Psi(x,y)$ is determined by Ampere's law relating $\Delta\Psi$ to the current density derived from (3.2). In a 2D geometry the Ψ function cannot be determined exactly and only approximations have been derived (Lembege & Pellat, 1982, for example) from the classical Harris solution (1D) $\Psi_0(x,z) = B_0 x - B_1 L \ln\cosh(z/L\exp(\varepsilon x/L))$ (in simplified parabolic geometry $\Psi_0(x,z) = B_0 x - B_1 z^2/2L$). A detailed expression for Ψ is however not required here because we simply adopt the magnetic configuration valid for $L \sim 8-10\ R_E$ in the Earth magnetotail, where L is the distance in R_E of the farthest

equatorial point of a given magnetic field line. Although invariance in y is still considered in the central plasma sheet, field lines are assumed to reach acceleration regions above the ionosphere using a quasi-dipolar model. The length of the field line is denoted by ℓ_0. Using a dipolar model at $L = 8\ R_E$, the magnitude of the magnetic field increases from roughly $B_0 \sim 60$ nT in the equatorial plane to $B_1 + B_0 \sim 60\ \mu$T at the ionosphere. A dimensionless stretching parameter $\varepsilon = B_0/(B_0 + B_1) \simeq B_0/B_1 \simeq 10^{-3}$ will be introduced later. The length of the field line is around 15.5 R_E. From this geometry we can derive orders of magnitude for some important parameters concerning both ion and electron dynamics. They are listed in the table 3.1.

Diamagnetic drift velocity may be derived from a fluid point of view. Force equilibrium in the plasma sheet requires that

$$u_i \simeq \frac{k_B T_i}{eB_0} \frac{d \ln n_0}{dx}. \tag{3.4}$$

If $L_n = |\nabla \ln n_0|^{-1}$ is the typical length scale of the density gradient along the tail, the normalized diamagnetic drift velocity reads $u_d = u_i/V_i = \rho_{Li}/(2L_n)$. From table 3.1 and with $L_n \sim R_E/2$, the typical drift velocity is equal to $u_d \sim 0.02$ or $u_i \simeq 11$ km.s^{-1} and $u_e \simeq 3$ km.s^{-1}.

Finally, the natural field-aligned coordinates system (ψ, y, χ) defined by

$$\vec{e}_\chi = \vec{B}/B \quad \vec{e}_\psi = \nabla\Psi/|\nabla\Psi| \quad \vec{e}_y = \vec{e}_\chi \times \vec{e}_\psi. \tag{3.5}$$

may be sometimes useful. Scale factors for this coordinates system are derived in Appendix A.1 where it is showed that these metric factors may be neglected in derivations since the parallel dimension ℓ_0 is assumed to be much larger than the perpendicular wavelength supposed to be of the order of the ion Larmor radius ρ_{Li} ($\rho_{Li}/\ell_0 \sim 1/1200$).

3.1.2 Perturbed distribution functions

The above equilibrium state is assumed to be perturbed linearly by an electromagnetic wave described by the two potentials $\phi(\vec{r}, t)$ and $A_{\parallel,1}(\vec{r}, t)$. In the low β approximation indeed, the perturbed magnetic field derives from a potential $\vec{A}_1 = A_{\parallel,1}\vec{e}_\chi$ with only a parallel component to the background field. We are mainly interested in drift waves propagating along the y axis with perpendicular wavelength of the order of the ion Larmor radius which is significantly smaller than the non homogeneity scale in the (x, z) plane. The perturbations are thus assumed to stay localized in the vicinity of the magnetic surface characterized by a

Table 3.1: Spatial and temporal scales characterizing particle dynamics in the Earth plasma sheet at $L = 8\ R_E$, the total density $n_0 = 1\ cm^{-3}$, $T_i = 2$ keV and $T_e = 500$ eV.

Parameter	Ion	Electron
Thermal velocity $V_\alpha = \sqrt{2k_B T_\alpha / m_\alpha}$ (km.s^{-1})	620	13000
Maximum Larmor radius $\rho_{L,\alpha} = \sqrt{k_B T_\alpha\, m_\alpha}/(eB_0)$ (km)	112	1.3
Maximum cyclotron period $2\pi m_\alpha / eB_0$ (s)	1	6×10^{-4}
Maximum bounce period $\tau_{b,\alpha} \simeq \pi/2\sqrt{1+\varepsilon}\ \ell_0/V_\alpha$ (s)	290 $\sim$ 5 min	13.6
Diamagnetic drift velocity with a density gradient scale of $L_n = R_E/2$ (km.s^{-1})	11	3

given value Ψ_0. Following other studies based on the same assumption (Antonsen & Lane, 1980; Pellat, 1990; Hurricane *et al.*, 1994), we adopt a WKB formalism and choose a spatial dependence for the perturbed particle distribution function of the form

$$f_1^{(\alpha)}(\vec{r}, \vec{w}, t) = \tilde{f}_1^{(\alpha)}(\Psi_0, \ell, k, \omega, \vec{w}) \mathrm{e}^{i(ky - \omega t)}. \tag{3.6}$$

where $\vec{w}$ is the particle velocity at time t (to be distinguished from the velocity $\vec{v}$ at former times $t' < t$), ℓ the position of the particle along the field line at time t and k the wave number along the y-direction. In the following, the amplitude will be noted simply $\tilde{f}^{(\alpha)}(\ell)$, assuming implicit any reference to Ψ_0, ω, k and $\vec{w}$. Similarly the potentials read

$$\phi_1(\vec{r}, t) = \tilde{\phi}(\ell) \mathrm{e}^{i(ky - \omega t)}, \quad A_{\parallel,1}(\vec{r}, t) = \tilde{a}_\parallel(\ell) \mathrm{e}^{i(ky - \omega t)}. \tag{3.7}$$

The linearized Vlasov equation for distribution function $f^{(\alpha)}(\vec{r}, \vec{v}, t) = F_0^{(\alpha)}(\vec{r}, \vec{v}) + f_1^{(\alpha)}(\vec{r}, \vec{v}, t)$ with $f_1 \ll F_0$ is

$$\frac{\partial f^{(\alpha)}}{\partial t} + \vec{v} \frac{\partial f^{(\alpha)}}{\partial \vec{r}} + \frac{q_\alpha}{m_\alpha} (\vec{E} + [\vec{v} \times \vec{B}]) \frac{\partial f^{(\alpha)}}{\partial \vec{v}} = 0. \tag{3.8}$$

So the perturbed distribution function $f_1^{(\alpha)}$ satisfies

$$\frac{\mathrm{d} f_1^{(\alpha)}}{\mathrm{d}t} = \frac{q_\alpha}{m_\alpha} \left[\nabla \phi_1 + \frac{\partial \vec{A}_1}{\partial t} - \vec{v} \times (\nabla \times \vec{A}_1) \right] \times \frac{\partial F_0^{(\alpha)}}{\partial \vec{v}}. \tag{3.9}$$

where $\mathrm{d}/\mathrm{d}t$ denotes the total time derivative. Using expression (3.2) for the unperturbed distribution function, an elegant solution for equation (3.9) may be formally written as (Tur

et al., 2014)

$$\tilde{f}_1^{(\alpha)}(\vec{r},\vec{w},t) = \frac{qF_0^{(\alpha)}(\vec{r})}{k_B T_\alpha}\left[-\tilde{\phi}(\vec{r},t) + \left(1-\frac{\omega_\alpha^*}{\omega}\right)\tilde{g}^{(\alpha)}(\vec{r},\vec{w},t)\right] \tag{3.10}$$

with

$$\tilde{g}^{(\alpha)} = -i\omega\int_{-\infty}^{t}\left[\tilde{\phi}(\ell') - v_\parallel\,\tilde{a}_\parallel(\ell')\right]\,\mathrm{e}^{i[\omega(t-t')-k(y-y')]}\,\mathrm{d}t', \tag{3.11}$$

and $\omega_\alpha^* = ku_\alpha$ is the drift frequency. In this last integral, $\ell' = \ell(t')$, $y' = y(t')$ are explicit functions of time, corresponding to particle position along the unperturbed trajectory at time $t' < t$, the instant t being the time of observation.

The integration of (3.11) for the trapped electron population relies on the double periodicity of the particle motion, namely the gyromotion and the bouncing between mirror points. To perform the computation a spatial form $[\tilde{\phi}(\ell), \tilde{a}_\parallel(\ell)]$ must be prescribed for the potentials. As we are interested in perturbations confined within the plasma sheet, Dirichlet conditions may be chosen at the two ends of the field line for the electrostatic potential. Thus, if $\ell = 0$ and $\ell = \ell_0$ pinpoint the boundaries, the potentials may be Fourier expanded as

$$\tilde{\phi}(\ell) = \sum_{n=1}^{\infty}\varphi_n\,\sin\left(n\pi\frac{\ell}{\ell_0}\right), \tag{3.12}$$

$$\tilde{a}_\parallel(\ell) = \sum_{n=1}^{\infty}\alpha_n\,\cos\left(n\pi\frac{\ell}{\ell_0}\right). \tag{3.13}$$

with

$$\varphi_n = \frac{2}{\ell_0}\int_0^{\ell_0}\tilde{\phi}(\ell)\sin\left(n\pi\frac{\ell}{\ell_0}\right)d\ell. \tag{3.14}$$

$$\alpha_n = \frac{2}{\ell_0}\int_0^{\ell_0}\tilde{a}_\parallel(\ell)\cos\left(n\pi\frac{\ell}{\ell_0}\right)d\ell. \tag{3.15}$$

Calculation may be carried on for each mode, but the present analysis will restrict on the fundamental mode ($n = 1$) only. From (3.12)-(3.13) it is seen that $\tilde{\phi}$ and $\tilde{a}_\parallel$ have different symmetry properties along the field line. This is consistent with the expression of

the magnetic and parallel electric fields

$$b_{\psi,1} = ik_y \tilde{a}_\parallel \, \mathrm{e}^{i(ky-\omega t)}, \tag{3.16}$$

$$e_{\parallel,1} = \left[i\omega \, - \frac{\pi}{\ell_0} \frac{\varphi_1}{\alpha_1} \right] \tilde{a}_\parallel \, \mathrm{e}^{i(ky-\omega t)}, \tag{3.17}$$

$$e_{y,1} = -ik_y \tilde{\phi} \, \mathrm{e}^{i(ky-\omega t)}. \tag{3.18}$$

With this choice of boundary conditions a non zero parallel electric field is generated at the ionospheric ends so the expected unstable modes may become important in the triggering process of auroras.

The time integration of (3.11) along the unperturbed particle orbit has been already exposed in details in section III of Fruit *et al.* (2013). Here, we only summarize the main steps of the calculation which are also similar to the ones followed in Fruit *et al.* (2017).

1. Integration along the gyromotion leads to the usual series of Bessel functions of the argument $\xi_\alpha = kv_\perp/\omega_{c\alpha}$. Since the expected perturbations oscillate around the electron bounce frequency ω_{be} which is much lower than the electron gyrofrequency ω_{ce}, the Bessel expansion may be restricted to the zero order term and no electron cyclotron resonance is taken into account. This assumption should not hold for ions, however, since the ion gyrofrequency may sometimes be comparable to ω_{be}. Nevertheless, we decide to discard them in this first approach of the drift-bounce interaction problem, and restrict the analysis to the situation where $\omega \sim \omega_{be} \ll \omega_{ci} \ll \omega_{ce}$ which is consistent with values listed in table 1. The function $\tilde{g}^{(\alpha)}$ is well proportional to the factor $\exp(i\xi_0 \sin\theta_0)$ where ξ_0 is the value of ξ_α at $t = t_0$. The rest of expression (3.11) which we noted $h^{(\alpha)}$ no longer depends on the angle θ_0 but only on l, $v_\parallel$ and $v_\perp$.

$$h^{(\alpha)}(t_0) = -i\omega \int_{-\infty}^{t_0} [\tilde{\phi}(l) - v_\parallel(t) \cdot \tilde{a}_\parallel(l)] J_0(\xi_\alpha) e^{iM(t,t_0)} dt. \tag{3.19}$$

   with $M(t, t_0) = \omega(t - t_0)$. The drift according to $\mathbf{e}_y$ due to magnetic gradient and/or curvature is neglected.

2. The integration of Eq.(3.19) over the bounce motion may be simplified by using the

periodicity of the bounce motion.

$$h_{\pm}(\vartheta) = \omega \int_0^{\vartheta} \left\{ \tilde{\phi}(\tau) \left| \begin{matrix} \sin \\ -i\cos \end{matrix} M(\tau,\vartheta) + i v_{\parallel}(\tau)\, \tilde{a}_{\parallel}(\tau) \right| \begin{matrix} \cos \\ i\sin \end{matrix} M(\tau,\vartheta) \right\} d\tau + \\ + \omega \frac{\left| \begin{matrix} \cos \\ i\sin \end{matrix} M(0,\vartheta) \right|}{\sin M(0,\tau_b)} \int_0^{\tau_b} \left\{ \tilde{\phi}(l) \cos M(\tau,\tau_b) - i v_{\parallel}(\tau)\, \tilde{a}_{\parallel}(\tau) \sin M(\tau,\tau_b) \right\} d\tau, \quad (3.20)$$

The variable τ represents the time an electron takes to move from the lower mirror point to the current abscissa point. It's therefore a disguised spatial variable. The time ϑ taken by the electron to reach the abscissa point l.

3. Integration along the electron bounce motion is more involved. Noting the electron's Larmor radius is small compared with the transverse wavelength. Consequently, $\xi_e \ll 1$ and $J_0(\xi_e) \approx 1$.

$$h_{\pm}^{(e)}(\vartheta) = \omega \int_0^{\vartheta} \left\{ \tilde{\phi}(\tau) \left| \begin{matrix} \sin \\ -i\cos \end{matrix} \omega(\vartheta-\tau) + i v_{\parallel}(\tau)\, \tilde{a}_{\parallel}(\tau) \right| \begin{matrix} \cos \\ i\sin \end{matrix} \omega(\vartheta-\tau) \right\} d\tau + \\ + \omega \frac{\left| \begin{matrix} \cos \\ i\sin \end{matrix} \omega\vartheta \right|}{\sin \omega\tau_b} \int_0^{\tau_b} \left\{ \tilde{\phi}(l) \cos \omega(\tau_b-\tau) - i v_{\parallel}(\tau)\, \tilde{a}_{\parallel}(\tau) \sin \omega(\tau_b-\tau) \right\} d\tau, \quad (3.21)$$

4. Integration along the electron bounce motion requires to specify a model for the parallel motion. To make things tractable analytically, this parallel motion is assumed to be purely harmonic. Noting μ the magnetic moment, the parallel velocity takes the simple form:

$$v_{\parallel}(t) \;=\; v_m \sin \omega_b t = \sqrt{\frac{2(E-\mu\, B_0)}{m_e}} \sin\left(\pi \frac{t}{\tau_b}\right). \quad (3.22)$$

From this it is easy to derive the particle position along the field line

$$\ell(t) = \frac{\ell_0}{2}\left[1 - \sqrt{\frac{E-\mu\, B_0}{\mu\, B_1}} \cos \omega_b t\right], \quad (3.23)$$

and two equivalent expressions for the magnetic field :

$$B(\ell) = B_0 + B_1 \left(\frac{2\ell}{\ell_0} - 1\right)^2 = B_1 \left[\frac{E + \mu\, B_0}{2\mu\, B_1} + \frac{E - \mu\, B_0}{2\mu\, B_1} \cos 2\omega_b t\right]. \tag{3.24}$$

The bounce period is then given by

$$\tau_b = \pi \frac{\ell_0}{2} \sqrt{\frac{m_e}{2\mu\, B_1}(1+\varepsilon)}. \tag{3.25}$$

It depends only on μ and not on the energy of the particle. This result comes from the initial assumption of harmonic motion. More complex parallel motions should lead to more realistic relationship $\tau_b(E, \mu)$ but a numerical integration would be likely necessary.

From this simple model describing the electron parallel bounce motion, however, it is possible to compute analytically the integral (3.21)

$$h_{\pm}^{(e)}(\vartheta) = \phi \left\{ \begin{vmatrix} J_0(\zeta) \\ 0 \end{vmatrix} + \sum_{n=1}^{\infty} (-1)^n J_{2n}(\zeta) \begin{vmatrix} S_{2n} \cos \\ -iD_{2n} \sin \end{vmatrix} 2n\omega_b \vartheta \right\} + \\ + i\frac{v_m}{2}\, a_{\parallel} \sum_{n=1}^{\infty} (-1)^n \left[J_{2n-1}(\zeta) + J_{2n+1}(\zeta)\right] \begin{vmatrix} D_{2n} \cos \\ -iS_{2n} \sin \end{vmatrix} 2n\omega_b \vartheta, \tag{3.26}$$

where

$$\zeta = \frac{\pi}{2} \sqrt{\frac{E - \mu B_0}{\mu B_1}} \quad \text{and} \quad \begin{vmatrix} S_{2n} \\ D_{2n} \end{vmatrix} = \frac{\omega}{\omega + 2n\omega_b} \pm \frac{\omega}{\omega - 2n\omega_b}. \tag{3.27}$$

So one gets (see equations (61) and (62) in Tur *et al.* (2014)):

$$\begin{aligned} g_{+}^{(e)} &= \varphi_1 \left[J_0(\zeta) - J_2(\zeta) \left(\frac{\omega}{\omega + 2\omega_b} + \frac{\omega}{\omega - 2\omega_b}\right) \cos 2\omega_b t\right] - \\ &- i\frac{v_m}{2} \alpha_1\, J_1(\zeta) \left(\frac{\omega}{\omega + 2\omega_b} - \frac{\omega}{\omega - 2\omega_b}\right) \cos 2\omega_b t, \end{aligned} \tag{3.28}$$

$$\begin{aligned} g_{-}^{(e)} &= i\varphi_1\, J_2(\zeta) \left(\frac{\omega}{\omega + 2\omega_b} - \frac{\omega}{\omega - 2\omega_b}\right) \sin 2\omega_b t - \\ &- \frac{v_m}{2} \alpha_1\, J_1(\zeta) \left(\frac{\omega}{\omega + 2\omega_b} + \frac{\omega}{\omega - 2\omega_b}\right) \sin 2\omega_b t. \end{aligned} \tag{3.29}$$

To get these expressions we have inserted the particle position $\ell(t')$ given by (3.23)

into the perturbed potentials (3.12-3.13) and then used the following classical Bessel expansions (up to the second order terms because $J_n(\zeta)$ is a fast decreasing function with index n):

$$\cos(\zeta \cos \omega_b t') \approx J_0(\zeta) - 2J_2(\zeta)\, \cos(2\omega_b t') \tag{3.30}$$

$$\sin(\zeta \cos \omega_b t') \approx 2J_1(\zeta)\, \cos(\omega_b t') \tag{3.31}$$

The difference between g_+ and g_- is related to the symmetry with respect to the parallel velocity, g_+ (resp. g_-) being a even (resp. odd) function of $w_\parallel$. This may help the future integration over $w_\parallel$ (see next section).

5. Although the ion gyrofrequency $\omega_c^{(i)}$ may sometimes be comparable to ω_{be}, we decide to discard ion cyclotron effects in the first approach of the drift-bounce interaction problem. Since ions bouncing period are slower than electrons $\omega_{bi} \ll \omega_{be}$, we may adopt a purely local response for the ions. In other terms, the perturbation period $\omega^{-1} \sim \tau_{be}$ is short compared to any time scale of the parallel ion motion. This means physically that ions remain almost at the same position along the field line during one wave period.

$$h_+^{(i)}(l) = \tilde{\phi}(l) J_0(\xi_i), \tag{3.32}$$

$$h_-^{(i)}(l) = -w_\parallel \tilde{a}_\parallel(l) J_0(\xi_i). \tag{3.33}$$

The ion perturbation function in this approximation is

$$g_+^{(i)} = J_0(\xi_i)\, \mathrm{e}^{i\xi_i \sin\theta}\, \sin\left(\pi \frac{\ell}{\ell_0}\right)\, \varphi_1, \tag{3.34}$$

$$g_-^{(i)} = -w_\parallel\, J_0(\xi_i)\, \mathrm{e}^{i\xi_i \sin\theta}\, \cos\left(\pi \frac{\ell}{\ell_0}\right)\, \alpha_1, \tag{3.35}$$

where θ is the gyro-angle at the present time t.

It is convenient for further computations to normalize the argument ξ_i in the following manner :

$$\xi_i = k \frac{m_i\, w_\perp}{eB(\ell)} = \sqrt{2\epsilon^2\, k^2\, \rho_{Li}^2}\, \frac{\tilde{w}_\perp}{\tilde{B}(\ell)}, \tag{3.36}$$

$\tilde{w}_\perp$ is the perpendicular velocity normalized to the ion thermal speed, $\tilde{B}$ is the normalized field to its maximum value B_1 and $\rho_{Li} = \sqrt{m_i\, k_B T_i}/eB_0$ is the thermal ion Larmor radius in the equatorial plane.

3.1.3 Charge density and parallel current perturbations

In this section, we derive the resulting perturbation in the charge density $\tilde{\rho}$ and in the parallel current density $\tilde{j}_\parallel$, in order to get the dispersion relation for the drift Alfvén modes :

$$\tilde{\rho}(\ell) = q_i \int \tilde{f}^{(i)}(\ell, \vec{w})\, \mathrm{d}\vec{w} + q_e \int \tilde{f}^{(e)}(\ell, \vec{w})\, \mathrm{d}\vec{w}, \tag{3.37}$$

$$\tilde{j}_\parallel(\ell) = q_i \int w_\parallel\, \tilde{f}^{(i)}\, \mathrm{d}\vec{w} + q_e \int w_\parallel\, \tilde{f}^{(e)}\, \mathrm{d}\vec{w}. \tag{3.38}$$

Before inserting (3.10) into these expressions, note that the background distribution function (3.2) takes the following form :

$$F_0(\vec{w}) = \frac{n_0(\Psi_0)}{\pi^{3/2}\, V_\alpha^3}\, \mathrm{e}^{-u_\alpha^2/V_\alpha^2}\, \mathrm{e}^{-2w_y\, u_\alpha/V_\alpha}\, \mathrm{e}^{-E/k_B T_\alpha}. \tag{3.39}$$

In the context of the Earth's magnetotail, and according to table 3.1, typical ratios between diamagnetic drift velocity u_α and thermal velocity $V_\alpha = \sqrt{2k_B T_\alpha/m_\alpha}$ are 0.02 for ions and $2{\cdot}10^{-4}$ for electrons, thus the quantities u_α^2/V_α^2 and $2w_y\, u_\alpha/V_\alpha$ are small compared to 1 and may be neglected. The distribution function F_0 then reduces to a standard maxwellian function of temperature T_α. The drift frequency $\omega_\alpha^* = k u_\alpha$ is not assumed, however, to be small compared to ω. As we are primarily interested in drift-bounce effects on the electrons, the perturbation frequency ω is expected to be close to the electron bounce frequency $\omega_{be} \sim 0.2\ \mathrm{s}^{-1}$ whereas the wavelength is of the order of the ion Larmor radius (112 km). Drift-bounce effects may become interesting to investigate when u_i is of the order of $\rho_{Li}/\tau_{be} \sim 10$ km/s, which is plausible in a region of strong density gradient across the magnetic shells ($u_d \sim 0.01$ and gradient length scale $L_n \sim 2R_E$).

With this simplification and from equations (3.10) and (3.39), the charge and current densities take the following form

$$\begin{aligned}
\tilde{\rho} &= n_0\, e^2 \left[-\left(\frac{1}{k_B T_i} + \frac{1}{k_B T_e} \right) \tilde{\phi} + \sum_{i,e} \frac{2}{\pi^{3/2}\, V_\alpha^3} \times \right. \\
\times & \qquad \left. \frac{\omega - \omega_\alpha^*}{\omega} \int \tilde{g}_+^{(\alpha)}\, \frac{\mathrm{e}^{-E/k_B T_\alpha}}{k_B T_\alpha}\, w_\perp\, \mathrm{d}w_\perp\, \mathrm{d}w_\parallel\, \mathrm{d}\theta \right],
\end{aligned} \tag{3.40}$$

$$\begin{aligned}
\tilde{j}_\parallel &= n_0\, e^2 \sum_{i,e} \frac{2}{\pi^{3/2}\, V_\alpha^3} \frac{\omega - \omega_\alpha^*}{\omega} \times \\
\times & \qquad \int \tilde{g}_-^{(\alpha)}\, \frac{\mathrm{e}^{-E/k_B T_\alpha}}{k_B T_\alpha}\, w_\parallel\, w_\perp\, \mathrm{d}w_\perp\, \mathrm{d}w_\parallel\, \mathrm{d}\theta.
\end{aligned} \tag{3.41}$$

We have used cylindrical coordinates $(w_\perp, \theta, w_\parallel)$ along the local magnetic field and the integration domain runs from 0 to ∞ for both components.

As for the potentials, the charge and current densities should be expanded in Fourier series as in (3.12-3.13). Only the first harmonic ($n = 1$) is considered in this study:

$$\left| \begin{array}{l} \rho_1 \\ j_1 \end{array} \right. = \frac{2}{\ell_0} \int_0^{\ell_0} \left| \begin{array}{l} \tilde{\rho}(\ell) \ \sin \\ \tilde{j}_\parallel(\ell) \ \cos \end{array} \right. \left(\frac{\pi \ell}{\ell_0} \right) \mathrm{d}\ell. \tag{3.42}$$

Taking the Fourier transform of (3.40-3.41) one gets

$$\begin{aligned} \varrho_1 &= \frac{n_0 \, e^2}{k_B T_e} \left[- \left(1 + \frac{T_e}{T_i} \right) \varphi_1 + \right. \\ &\qquad \left. + \left(1 - \frac{\omega_e^*}{\omega} \right) A_{e,\rho} + \frac{T_e}{T_i} \left(1 - \frac{\omega_i^*}{\omega} \right) A_{i,\rho} \right], \qquad (3.43) \\ j_1 &= \frac{n_0 \, e^2}{k_B T_e} \left[\left(1 - \frac{\omega_e^*}{\omega} \right) A_{e,\parallel} + \frac{T_e}{T_i} \left(1 - \frac{\omega_i^*}{\omega} \right) A_{i,\parallel} \right], \qquad (3.44) \end{aligned}$$

with

$$\begin{aligned} A_{\alpha,\rho} &= \frac{4}{\pi^{3/2} \, V_\alpha^3 \, \ell_0} \int_0^{\ell_0} \mathrm{d}\ell \, \sin \left(\pi \frac{\ell}{\ell_0} \right) \int_0^\infty \mathrm{d}w_\parallel \, \mathrm{e}^{-w_\parallel^2 / V_\alpha^2} \times \\ \times & \int_0^\infty \mathrm{d}w_\perp \, w_\perp \, \mathrm{e}^{-w_\perp^2 / V_\alpha^2} \int_0^{2\pi} \mathrm{d}\theta \, \tilde{g}_+^{(\alpha)}(\ell, w_\perp, w_\parallel, \theta), \qquad (3.45) \\ A_{\alpha,\parallel} &= \frac{4}{\pi^{3/2} \, V_\alpha^3 \, \ell_0} \int_0^{\ell_0} \mathrm{d}\ell \, \cos \left(\pi \frac{\ell}{\ell_0} \right) \int_0^\infty \mathrm{d}w_\parallel \, w_\parallel \, \mathrm{e}^{-w_\parallel^2 / V_\alpha^2} \times \\ \times & \int_0^\infty \mathrm{d}w_\perp \, w_\perp \, \mathrm{e}^{-w_\perp^2 / V_\alpha^2} \int_0^{2\pi} \mathrm{d}\theta \, \tilde{g}_-^{(\alpha)}(\ell, w_\perp, w_\parallel, \theta). \qquad (3.46) \end{aligned}$$

As $g_\pm^{(\alpha)}$ are linear combinations of φ_1 and α_1, equations (3.43) and (3.44) can also be written in the following matrix form:

$$\begin{pmatrix} \varrho_1 \\ \mu_0 \, j_1 \end{pmatrix} = \mathcal{M} \begin{pmatrix} \varphi_1 \\ \alpha_1 \end{pmatrix} \tag{3.47}$$

Matrix $\mathcal{M}$ will be explicitly detailed in the next section. Beforehand we wish to explain how to get the dispersion relation for the drift-Alfvén modes, which still remains the aim of this long development.

Following previous works on this topic (Hasegawa, 1975; Weiland, 2012), this equation is simply obtained via the quasi-neutrality condition $\tilde{\rho} \approx 0$ (since $\omega \ll \omega_p$) and parallel

Ampere's law $\mu_0\,\tilde{j}_\parallel = -[\Delta\vec{a}_1]_\parallel$. As the perpendicular wavelength of the order of the thermal ion Larmor radius is much shorter than the length of the field line, it is usual to neglected the parallel contribution to the laplacian and according to Appendix A.1, we write the Ampere's law for the first Fourier harmonic as $\mu_0\,j_1 = k^2\,\alpha_1$.

Thus, the dispersion relation is obtained by canceling the following determinant :

$$\left|\mathcal{M} - \begin{pmatrix} 0 & 0 \\ 0 & k^2 \end{pmatrix}\right| = 0. \tag{3.48}$$

3.2 Electromagnetic drift wave dispersion relation

3.2.1 Electron contribution to the dispersion relation

Let's focus on equations (3.45) and (3.46) for the electrons. We must perform an integration over the velocity space domain on which electrons are trapped. Notice first that $g_\pm^{(e)}$ does not depend on the gyro-angle θ, the integral over θ simply gives a factor 2π. Second, instead of working with variables $w_\perp$ and $w_\parallel$, it is more convenient to use energy E and magnetic moment μ, which are invariant of motion. Thus,

$$w_\perp\,\mathrm{d}w_\perp\,\mathrm{d}w_\parallel = \frac{B}{m_e^2}\frac{\mathrm{d}E\,\mathrm{d}\mu}{w_\parallel}. \tag{3.49}$$

Only electrons with $E/(B_0+B_1) < \mu < E/B(\ell)$ can reach the abscissa ℓ along the field line and contribute to the charge/current density at that point. For example the integral (3.45) may be written more explicitly as

$$A_{e,\rho} = \frac{8}{\pi^{1/2}V_e^3\ell_0}\int_0^{\ell_0}\mathrm{d}\ell\,\sin\left(\pi\frac{\ell}{\ell_0}\right)\int_0^\infty \mathrm{d}E\,\mathrm{e}^{-E/k_BT_e}\times\int_{\mu_{\min}}^{E/B(\ell)}\mathrm{d}\mu\frac{B(\ell)}{m_e^2}\frac{\tilde{g}_+^{(e)}(\ell)}{w_\parallel}. \tag{3.50}$$

Integrals over ℓ and μ can be switched but the integration domain should be changed accordingly. For a given μ, the electron travels only between the two mirror points, or equivalently, the time τ defined by $\mathrm{d}\ell = v_\parallel\mathrm{d}\tau$ goes from 0 to τ_b. Equation (3.50) may thus be rewritten as

$$A_{e,\rho} = \frac{8}{\pi^{1/2}m_e^2\,V_e^3\ell_0}\int_0^\infty \mathrm{d}E\,\mathrm{e}^{-E/k_BT_e}\int_{\mu_{\min}}^{\mu_{\max}}\mathrm{d}\mu\times\int_0^{\tau_b}\mathrm{d}\tau\,B(\tau)\,\cos(\zeta\,\cos(\omega_b\tau))\,\tilde{g}_+^{(e)}(\tau). \tag{3.51}$$

With the use of expansion (3.30), expressions (3.28) of $g_+^{(e)}$ and (**??**) for $B(\tau)$, the integration over the time variable τ and over the energy E can be performed analytically as it has already been done in Tur et al. 2014. We do not reproduce the details here. Introducing the

dimensionless quantity

$$x = \pi \frac{\tau_{b,max}}{\tau_b} = \pi \sqrt{\frac{\mu}{E}(B_0 + B_1)} \tag{3.52}$$

and a normalized wave frequency to the minimum electron bounce frequency :

$$q = \omega\, \tau_{b,max} = \omega \times \frac{\pi\, \ell_0}{2} \sqrt{\frac{m_e}{2k_B T_e}(1+\epsilon)}, \tag{3.53}$$

the electron contribution to the charge and current densities may be written as

$$A_{e,\rho} = \mathcal{E}_1(q)\, \varphi_1 + i \frac{V_e}{2} \mathcal{E}_2(q)\, \alpha_1, \tag{3.54}$$

$$A_{e,\parallel} = iV_e\, \mathcal{E}_3(q)\, \varphi_1 + \frac{V_e^2}{2} \mathcal{E}_4(q)\, \alpha_1, \tag{3.55}$$

with

$$\mathcal{E}_1 = \int_{\pi}^{\pi/\sqrt{\epsilon}} \left[\Gamma_0(x) + \Gamma_1(x)\, W\left(\frac{q}{2x}\right) \right] \mathrm{d}x, \tag{3.56}$$

$$\mathcal{E}_2 = \int_{\pi}^{\pi/\sqrt{\epsilon}} \left[1 - \epsilon \frac{x^2}{\pi^2}\right]^{1/2} \Gamma_2(x)\, \frac{q}{2x} W\left(\frac{q}{2x}\right) \mathrm{d}x, \tag{3.57}$$

$$\mathcal{E}_3 = \int_{\pi}^{\pi/\sqrt{\epsilon}} \left[1 - \epsilon \frac{x^2}{\pi^2}\right]^{1/2} \Gamma_3(x)\, \frac{q}{2x}\, W\left(\frac{q}{2x}\right) \mathrm{d}x, \tag{3.58}$$

$$\mathcal{E}_4 = \int_{\pi}^{\pi/\sqrt{\epsilon}} \left[1 - \epsilon \frac{x^2}{\pi^2}\right] \Gamma_4(x)\, \frac{q^2}{4x^2}\, W\left(\frac{q}{2x}\right) \mathrm{d}x. \tag{3.59}$$

where the Γ's terms are real functions of the variable x listed in the appendix A.2 and W is a complex function related to the plasma dispersion Z:

$$W(z) = 1 + \frac{2z^2}{\pi^{1/2}} \int_{-\infty}^{\infty} \frac{t\, \mathrm{e}^{-t^2}}{t - z}\, \mathrm{d}t = 1 + 2z^2(1 + z\, Z(z)). \tag{3.60}$$

The important result lies in the resonant denominators at $\omega = \pm 2\omega_b(\mu)$ describing the resonance with the electron bounce motion, as they appear in (3.28) or (3.29). This can be viewed as a generalization of Landau damping calculation when integrating over the energy and magnetic moment. As the background distribution function is Maxwellian it is appropriate to introduce the Fried and Conte function Z (Fried & Conte, 1961). The argument of the Z-function $q/(2x) = \omega\tau_b/(2\pi) = \omega/(2\omega_b)$ is analogous to the more classical ratio $\omega/(k_\parallel V_e)$ in an open field line geometry.

We may notice that $A_{e,\rho}$ and $A_{e,\parallel}$ are functions of the complex frequency ω only. The

imaginary part is evaluated using the classical Landau prescription rule. Standard numerical procedure may be used to evaluate (3.56-3.59).

3.2.2 Ion contribution to the dispersion equation

Let us consider now the ion contribution. Expressions (3.34-3.35) for the perturbed distribution functions show that the natural variables are still $w_\perp$ and $w_\parallel$. First, we get rid of the gyro-angle variable θ by using the result

$$\int_0^{2\pi} \mathrm{e}^{i\xi_i \sin\theta} \mathrm{d}\theta = 2\pi\, J_0(\xi_i), \tag{3.61}$$

then from (3.45-3.46), the integration over the parallel velocity is straightforward while the integration over the perpendicular velocity may be performed by using the classical formula

$$\int_0^\infty x\, J_0^2(x\sqrt{2a})\, \mathrm{e}^{-x^2}\, \mathrm{d}x = \frac{1}{2} I_0(a)\, \mathrm{e}^{-a}. \tag{3.62}$$

Hence, referring to (3.36) for ξ_i, the ion contribution to charge and current densities may be written as

$$A_{i,\rho} = \mathcal{I}_s\, \varphi_1, \qquad A_{i,\parallel} = -\frac{V_i^2}{2} \mathcal{I}_c\, \alpha_1, \tag{3.63}$$

with

$$\mathcal{I}_s = 2 \int_0^1 I_0 \left(\frac{\epsilon^2 k^2 \rho_{Li}^2}{\tilde{B}^2(l)} \right) \mathrm{e}^{-\epsilon^2 k^2 \rho_{Li}^2 / \tilde{B}^2(l)} \sin^2 \pi l\, \mathrm{d}l \tag{3.64}$$

and a similar expression for $\mathcal{I}_c$ with a permutation in the sine/cosine functions.

This expression generalizes the usual calculation performed in a straight and homogeneous magnetic field geometry (Bellan, 2008). Here the calculation takes into account explicitly the non homogeneity of the magnetic field. One important feature to note is that the ion contribution depends on the wavenumber k only and is therefore purely real.

3.2.3 Dispersion relation for drift-Alfvén waves

Gathering all the equations written so far, we can write the charge and current perturbations as the already stated matrix form (see equation (3.47)) and after some last simplifications

the dispersion relation (3.48) reads

$$\begin{vmatrix} \frac{T_e}{T_i}\left(1-\frac{\omega_i^*}{\omega}\right)\mathcal{I}_s(k)+\left(1-\frac{\omega_e^*}{\omega}\right)\mathcal{E}_1(\omega)-\left[\frac{T_e}{T_i}+1\right] & i\left(1-\frac{\omega_e^*}{\omega}\right)\mathcal{E}_2(\omega) \\ i\left(1-\frac{\omega_e^*}{\omega}\right)\mathcal{E}_3(\omega) & -\frac{m_e}{m_i}\left(1-\frac{\omega_i^*}{\omega}\right)\mathcal{I}_c(k)+\left(1-\frac{\omega_e^*}{\omega}\right)\mathcal{E}_4(\omega)-2\frac{m_e}{m_i}k^2\rho_{Li}^2\tilde{c}_A^2 \end{vmatrix} = 0, \tag{3.65}$$

where $\tilde{c}_A = B_0/\sqrt{\mu_0 n_0 m_i}/V_i$ is the normalized Alfvén velocity in the equatorial plane ($B = B_0$).

Note that the top left element of the matrix corresponds to the electrostatic case considered in Fruit *et al.* (2017). The lower right term may be simplified by discarding the ion contribution proportional to $m_e/m_i \ll 1$. This approximation is often used in the literature (Weiland, 2012). It is however difficult to compare this dispersion relation to the one derived, for instance by Weiland (2012) in a straight magnetic field geometry with no end points and no bouncing electrons. The latter is not a simple limiting case of the presently investigated problem. But formally we may just verify that if one takes $\mathcal{E}_1 = 0$, $\mathcal{E}_2 = 2i$, $\mathcal{E}_3 = i$ and $\mathcal{E}_4 = -2$, eqs. (3.43) and (3.44) have similar expressions as the one derived in Weiland provided that $\omega = k_\parallel V_e$. The classical dispersion relation for drift Alfvén waves is given in the sec. A.3.

Actually equation (3.65) should be viewed as a new dispersion relation yielding new drift-bounce Alfvén modes in a magnetic bottle configuration. It is neither obvious that these new modes don't have a fluid equivalent as the non-local interaction between bouncing electrons and electromagnetic fluctuations cannot be reproduced in fluid models. The problem is clearly kinetic in nature.

3.3 Results

Equation (3.65) is numerically solved for different density gradient slopes, Alfvén velocities and L-shells. Neglecting the thickness of the ionosphere, the farthest mirror point on the field line coincides with the ground footpoint. Before investigating a parametric study let us consider a representative example of the dispersion relation. The Alfvén velocity is fixed to $c_A = 2V_i$ and the magnetic ratio $\varepsilon = 10^{-3}$ corresponding to an L-shell around 8 R_E. Figure 3.2 show the dispersion curves drawn for the density gradient slope $L_n = R_E/2$. Top (resp. bottom) panel displays the real part of the normalized frequency $\omega_r\tau_{be}$ (resp. the imaginary part $\gamma\tau_{be}$ or growth rate) as a function of the real wave number $k_\perp\rho_{Li}$. Three modes are found to propagate along the y-axis. Two of them have a positive real frequency while the

third one has a negative real frequency. It simply means that the latter propagates in the negative y direction (electron drift). From the sign of the imaginary part one notices that two propagating modes are damped and only one is unstable with a quite strong growth rate of the order of the bounce frequency. The unstable mode (red line) propagates in the positive y direction (ion drift). It is helpful to introduce the wave impedance normalized to the Alfvén velocity (Onishchenko *et al.*, 2009) to get a better understanding of the nature of the propagating modes:

$$w.i. = \left| \frac{e_y}{b_\psi \, c_A} \right| \propto \frac{\phi_1}{\alpha_1 \, c_A} \tag{3.66}$$

that can be computed directly in terms of ω and k_y using the dispersion relation (**??**). This parameter should be equal to one for a pure Alfvén wave and is expected to remain close to unity for an alfvénic mode. Figure 3.3 shows the normalized wave impedance for the three modes computed on Figure 3.2 using the same pattern. The wave impedance remains less than 5 for the mode propagating in the negative y direction (eastward) while it increases strongly with the frequency for the unstable mode. We can conclude that the system supports the propagation of waves with similar polarization and characteristics as Alfvén waves but they are also strongly damped. On the other side the unstable mode has little to do with Alfvén waves actually. It is more similar to an electrostatic drift wave with a strong wave impedance. This is consistent with the fact that the instability develops mainly on the plasma inhomogeneity independently of magnetic perturbations. As we are mostly interested by this instability, the rest of the discussion will focus on this unstable solution only.

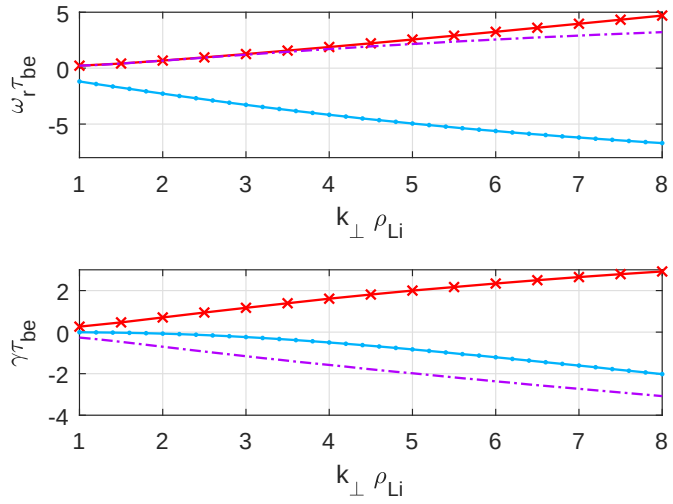

Figure 3.2: Normalized frequency (top) $\omega_r \tau_{be}$ and growth rate (bottom) as a function of normalized wave number $k_\perp \rho_{Li}$, solutions of dispersion relation (3.65) with typical near-Earth plasma sheet parameters : $T_i = 2$ keV, $T_e = 500$ eV, $n_0 = 1 \; cm^{-3}$, $c_A/V_i = 2$ and $L_n = R_E/2$. Only one mode is driven unstable (red line), the two others are damped.

The dispersion curves drawn for the unstable wave mode are shown in Figures 3.4 and 3.5 for several values of the density gradient slope L_n but with a fixed value of the Alfvén

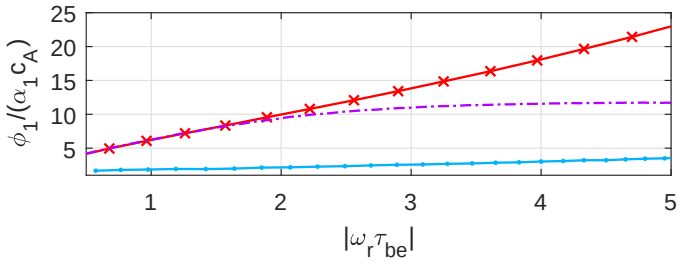

Figure 3.3: Wave impedance $\varphi_1/\alpha_1 c_A$ as a function of the frequency $|\omega_r \tau_{be}|$ for the three modes on fig. 3.2. The eastward propagating damped mode (blue line) is mainly alfvénic whereas the unstable mode (red line) and the other damped mode are more similar to electrostatic waves (drift wave).

velocity $c_A = 2V_i$ and a fixed $\epsilon = 10^{-3}$. To stay with the limits of validity our the model, the frequency should be less than the typical ion cyclotron frequency $\omega_{ci}\tau_{be} \sim 10$ which imposes the wavelength to stay of the order of the ion Larmor radius ($k_\perp \rho_{Li} \sim 2\pi$). For mild density gradient, the real frequency ω_r can be approximated by a linear function whose slope depends on the diamagnetic drift velocity u_i. The phase velocities of the waves are $v_{ph}|_{L_n=\{0.25,0.5,2\}R_E} = \{6.5, 4, 2.4\}$ km/s where the ion drift velocity are $u_i|_{L_n=\{0.25,0.5,2\}R_E} = \{22; 11; 2.7\}$ km/s. So the two velocities are of the same order of magnitude, but apparently there is no simple linear relationship between v_{ph} and u_i.

Concerning now the growth rate of the instability, we can see from Fig. 3.5 that γ increases with $k_\perp$ for all values of L_n. Actually if the curves are continued to higher values of $k_\perp$, it can be checked that γ reaches a maximum and then decreases. But this maximum growth rate is obtained for an irrelevant value of either the wavenumber for the frequency. It is probably due to the simplifications adopted in the model, especially the fact that ion cyclotron effects are not considered, whereas they should play a definitive role in this range of frequencies/ wavenumbers.

More interestingly is the variation of γ with the density gradient scale L_n. For very weak diamagnetic drift velocity corresponding to L_n above 2 R_E the growth rate remains harmless for sensible wavenumbers. In this case the mode grows too slowly to destabilize the current sheet in tens of seconds and we may conclude that the plasma sheet is stable. As the density gradient is steepening the growth rate becomes of the same order of the real frequency revealing a very fast instability. The maximum growth rate is obtained for $L_n = 0.25\ R_E$ corresponding to a normalized diamagnetic drift velocity $u_d \sim 0.02$. For higher drift velocity we observe a drop in the maximum growth rate which corresponds to much smaller wavenumber. For instance, at a wavelength of the order of one Larmor radius ($k_\perp \rho_{Li} = 2\pi$), the e-folding time $2\pi/\gamma$ of the instability is about 25 minutes for $L_n = 2.5\ R_E$, a too long time to really destabilize the magnetic structure, but it drops to

30 s for $L_n = 0.25\ R_E$.

Comparison with the pure electrostatic drift instability (Fruit *et al.*, 2017) shows that growth rates of the electromagnetic drift modes are lower than that of electrostatic drift waves with the same diamagnetic drift velocity. For example, for wave number ~ 0.02/km and the diamagnetic drift velocity $u_i \sim 11$ km/s ($u_d \sim 0.02$), corresponding to the density gradient slope $L_n = 0.5\ R_E$ the amplitude growth rate of the electrostatic drift waves is ~ 0.08/s and that of the electromagnetic drift wave is ~ 0.05/s. In other words, the perturbation in the parallel current produces a kind of stabilization effect on the drift instability.

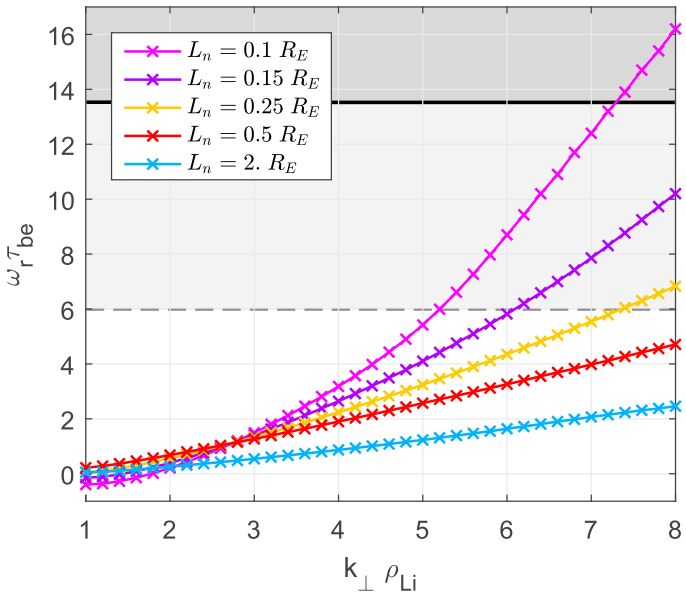

Figure 3.4: Normalized frequency $\omega_r \tau_{be}$ as a function of wave number $k_\perp \rho_{Li}$ for the electromagnetic drift unstable mode with the near-Earth (at $L = 8\ R_E$) plasma sheet parameters: $T_i = 2$ keV, $T_e = 500$ eV, $n_0 = 1\ cm^{-3}$, $c_A/V_i = 2$ and varying density gradient slope L_n. The frequencies in the shaded region are influenced by the ions' cyclotron movement, neglected by theory ($\omega \ll \omega_{ci}$) .

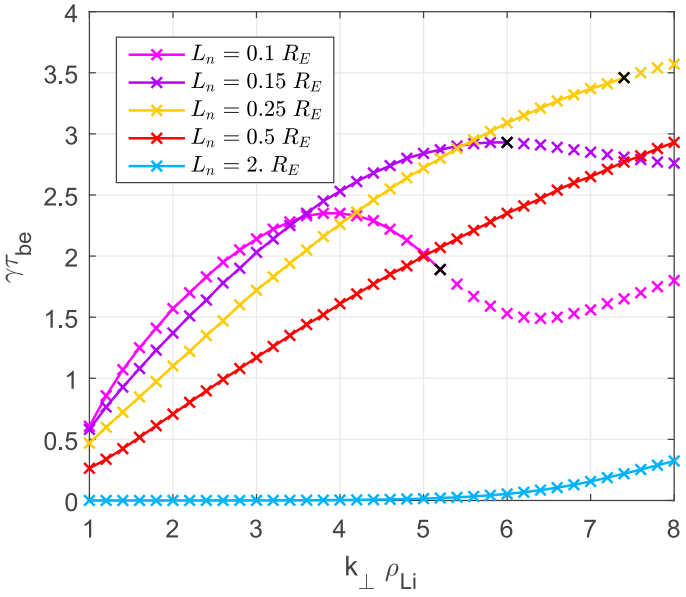

Figure 3.5: Growth rate $\gamma \tau_{be}$ as a function of wave number $k_\perp \rho_{Li}$ for the electromagnetic drift unstable mode with the near-Earth (at $L = 8\ R_E$) plasma sheet parameters: $T_i = 2$ keV, $T_e = 500$ eV, $n_0 = 1\ cm^{-3}$, $c_A/V_i = 2$ and varying density gradient slope L_n.

Let us now investigate the influence of parameters such as the Alfvén velocity c_A or the stretching constant $\varepsilon = B_0/B_1$ on the boundary between stable and unstable wave modes. We may choose this boundary at a normalized growth rate of 0.5. With a typical bounce period of 14 s (see table I) modes with growth rate less than $\gamma\tau_{be} = 0.5$ have e-folding time longer than 3 minutes and we may consider those as stable as they do not contribute to the rapid destabilization of the plasma sheet observed during a usual substorm onset.

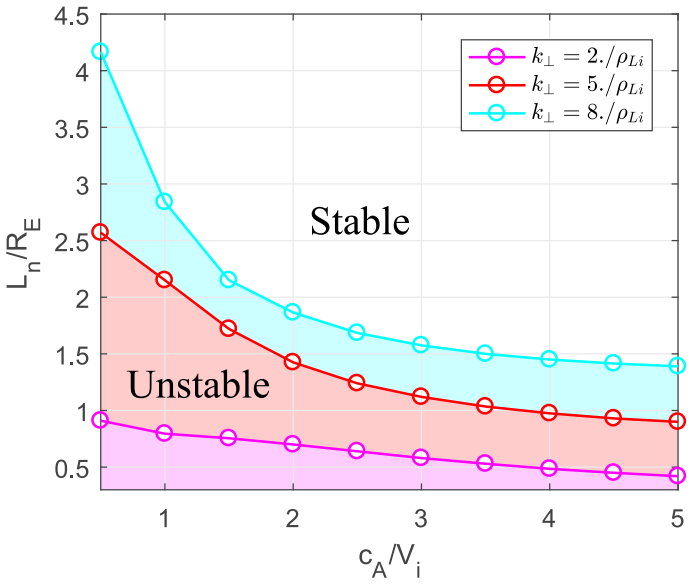

Figure 3.6: The density gradient slope L_n as a function of the Alfven speed c_A with $\gamma\tau_{be} = 0.05$, $\varepsilon = 1.1 \cdot 10^{-3}$ on $L = 8\ R_E$ and varying wave number $k_\perp$. The plasma parameters in the shaded region correspond to the unstable mode.

Figure 3.6 displays in the $L_n - c_A$ plane the instability threshold $\gamma\tau_{be} = 0.5$ for a few representative wavenumbers and $L = 8\ R_E$. The shaded area corresponds to unstable mode. It means for instance that for the Alfvén velocity $c_A = 2V_i$, the electromagnetic drift mode becomes potentially unstable for the equilibrium of the sheet if the density gradient scale is smaller than 1.87 R_E for a wavelength of 0.75 times the ion Larmor radius ($k_\perp\rho_{Li} = 8$) but it should be smaller than 0.7 R_E for a larger wavelength of the order of 3 Larmor radii ($k_\perp\rho_{Li} = 2$). Thus, perturbations with smaller perpendicular wavelengths are more likely to be driven unstable. The ratio of the Alfvén velocity to the ion thermal speed also modifies the position of the instability threshold. The plasma sheet tends to be harder to destabilize when the c_A/V_i is high. On the contrary for low ratio $c_A/V_i < 1$. i.e. with denser and hotter ions, a much milder density gradient is sufficient to excite the electromagnetic drift instability.

Figure 3.7 shows the same instability threshold $\gamma\tau_{be} = 0.5$ but in the (L_n, L) plane for $c_A/V_i = 2$. Changing the L-shell acts principally on the stretching parameter $\epsilon = B_0/B_1$ given the fact that B_1 is the value of the magnetic field at the ground. It is noticeable

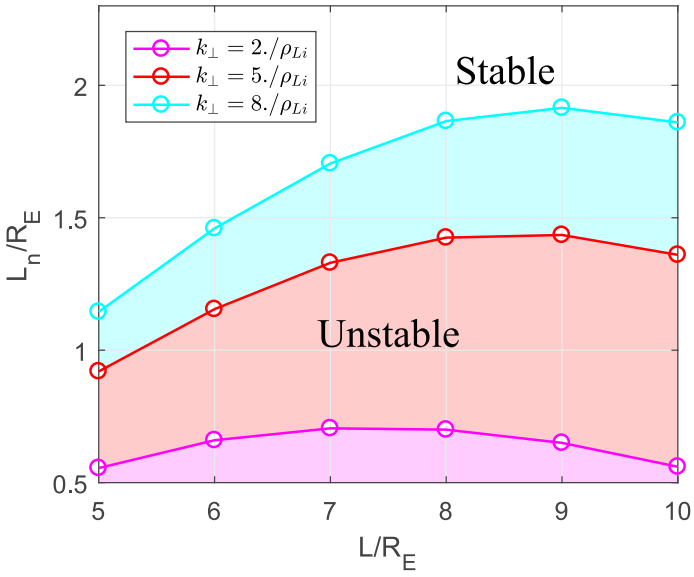

Figure 3.7: The density gradient slope L_n as a function of the magnetic L-shell with $\gamma\tau_{be} = 0.05$, $c_A = 2V_i$ and varying wave number $k_\perp\rho_{Li}$.

that the instability threshold adopts a parabolic profile versus L with a maximum localized in the near-Earth region of the magnetotail. The maximum of the parabola corresponds to the optimal magnetic shell on which the probability of instability onset at low density gradient is higher. Mode with wavenumber $k_\perp \rho_{Li} = 8$ are likely to become unstable at $L = 9\ R_E$ whereas modes with smaller wavenumber $k_\perp \rho_{Li} = 2$ are driven unstable with a steeper density gradient at a closer shell ($L = 7\ R_E$) to the Earth. Obviously this result also depends on the Alfvèn velocity, but one can check that the position of the maximum is only sligthly shifted away from the Earth when c_A/V_i is increased. An interesting outcome of this parametric analysis is to show that a progressive increase of the density gradient leads to an instability developing first at $L \sim 7 - 9\ R_E$ which is consistent with observations of near Earth substorm onset (Roux *et al.*, 1991).

Chapter 4

Observational analysis

In the previous chapter, we developed the electromagnetic drift-Alfvén wave theory taking into account the electron bounce. Previously, Watt & Rankin (2009) showed that Alfvén waves with short perpendicular scales initiated in the drift-kinetic warm ($V_{Te}/V_A > 1$) magnetotail can accelerate electrons to form aurora. By in-situ measurements, Hull *et al.* (2016) also confirmed, Alfvénic nature of auroral acceleration during onset and expansion of a substorm.

In the Earth magnetotail, the cross-tail current is mainly produced by diamagnetic drift effects due to a density gradient along the tail. In addition to an electrostatic potential (i. e. an electrostatic case considered by Fruit *et al.* (2017)), we also included a parallel component of perturbed magnetic potential. As noted by Le Contel *et al.* (2000), a parallel electric field affects the triggering process of auroras.

This theory leads to interesting results since electromagnetic drift waves are shown to be unstable provided that the diamagnetic drift velocity is sufficiently large. The predicted periods of the unstable waves are of the order of the electron bounce periods and the growth rates correspond to a few tenths of the period. Our objective is to compare these theoretical results with the observations. For this purpose, we analyze observations performed by the Time History of Events and Macroscale Interactions during Substorms (THEMIS) during the onset of a modest substorm.

In this chapter, we consider in section 4.1 ground-based data from the network of THEMIS all-sky imagers (ASIs) to establish a substorm onset timing on a selected auroral arc with a spatial wave-like structure. In section 4.2 an analysis of the magnetic fluctuations recorded by three THEMIS spacecraft located in the near-Earth magnetotail is performed. An estimate of the growth rate of the instability is assessed from a Hilbert-Huang transform. Finally section 4.3 compares the results of this data analysis to the kinetic model in the small-β regime with

a discussion of the importance of these electromagnetic drift waves in the triggering process of a magnetospheric substorm.

4.1 Auroral Development

We select an isolated weak substorm occurring on 03 February 2008 around 05:00 UT. The event has been recorded by the optical array of All-Sky-Imagers (ASI) covering the auroral oval across Canada and by three THEMIS spacecraft located in the near Earth current sheet at $\sim 10\ R_E$. This event is very similar to a classical substorm, with the difference that the onset is not followed by the classical fully-developed auroral expansion. In this respect, it can be called a small susbtorm. The fact that the activation remains modest is one of the criteria that we used to select the event. The idea is to take advantage of a longer linear phase of the triggering process than for a powerful substorm and, thus, to ease the characterization of the initial instability. The second criterium is the excellent location of TH-A, TH-D and TH-E that appear to be magnetically connected to the first auroral intensification (see later) and, thus, at or close to the active site in the near-Earth magnetotail.

Figure 4.1 shows the optical signature depicted by a mosaic generated by ASIs only from stations (from right to left) Sanikiluaq (SNKQ), Gillam (GILL), Ft. Smith (FSMI), Ft. Simpson (FSIM) and Inuvik (INUK) between 05:00 and 05:04 UT. The ASIs are white light auroral imagers responding to the green emission of aurora produced at about 110 km altitude (557.7 nm). The ASIs capture images at a 3 s cadence and provide up to 1 km spatial resolution at zenith. But at the edges of the camera fields of views (FOVs) the ASIs' lens system produces substantial distortions. The ASIs' FOV cover the auroral oval across Canada and Alaska. The magnetic footprints of spacrecraft TH-A, TH-D and TH-E, as inferred from Tsyganenko T96 model Tsyganenko (1995), are indicated. They are located at the very edge of the field of view of GILL camera. To some extents, it would have been appropriate to use the observations of the adjacent eastward station (SNKQ), but unfortunately an optical artefact has blurred the image at this particular time. In the Fig. 4.1 the onset arc is quite equatorward and marked with a red dotted line along which the east-west keogram (Fig. 4.3) is made. In near-Earth initiation scenario the substorm expansion phase commences with a plasma process initiated on magnetic field lines linked typically to the most equatorward auroral arc (Akasofu, 1964; Roux *et al.*, 1991; Lui & Murphree, 1998; Perraut *et al.*, 2003).

Figure 4.2 shows the optical signature observed by the Gilliam (GILL) station between 04:54:30 and 05:02:30 UT. Before 04:54:30, there is no indication of auroral light when the image taken 1 minute later (04:55:30) shows an activation at or close to the magnetic foot-

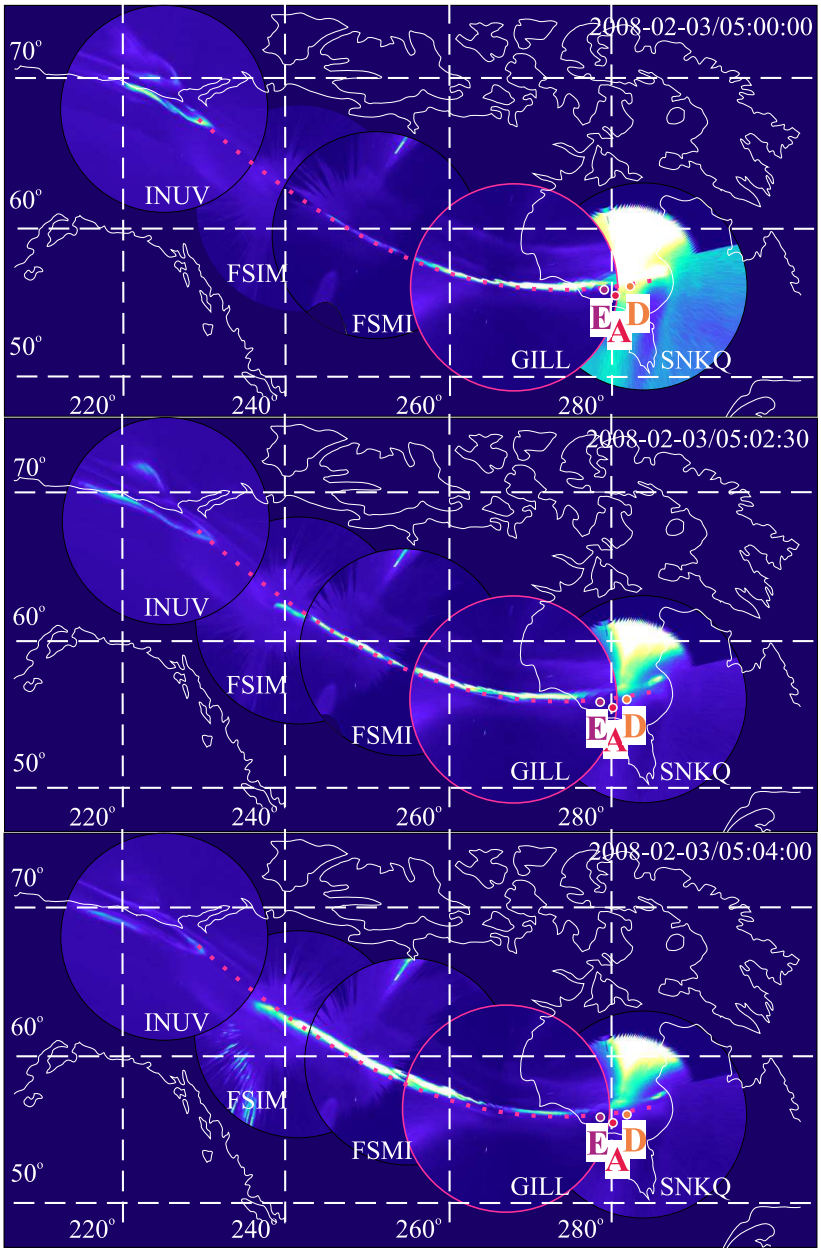

Figure 4.1: Collage of all-sky image mosaics in the geodetic coordinates (the azimuthal equidistant projection). Stations displayed from right to left are SNKQ, GILL, FSIM, FSMI, INUK. The dashed white lines indicate LOT and LAT reference lines. The red dotted line indicates the onset arc, from where auroral east-west keogram were made later. The red circle indicates the field of view of GILL ASI. The fieldline footprints of the TH-A, TH-D and TH-E spacecraft locations are mapped by using the T96 model. "A, D, E" indicate the footprints of different THEMIS satellites.

prints of TH-A, TH-D and TH-E. The auroral activation then follows the classical two-stage scenario of the auroral breakup described by Akasofu (1964).

The first stage, the Akasofu initial brightening (AIB), corresponds to an increase in the auroral intensity along an arc located at the onset latitude, without a poleward expansion. It is observed on these images from 04:55:30 to about 05:01:30. A wavy structure develops along the auroral arc, visible at 04:57:30 and later. The second stage is the Poleward expansion (PE). It is defined as the first auroral poleward motion that follows AIB, and lasts typically $5 - 10$ minutes. As seen in the Figure, PE starts between 05:01:30 and 05:02:30.

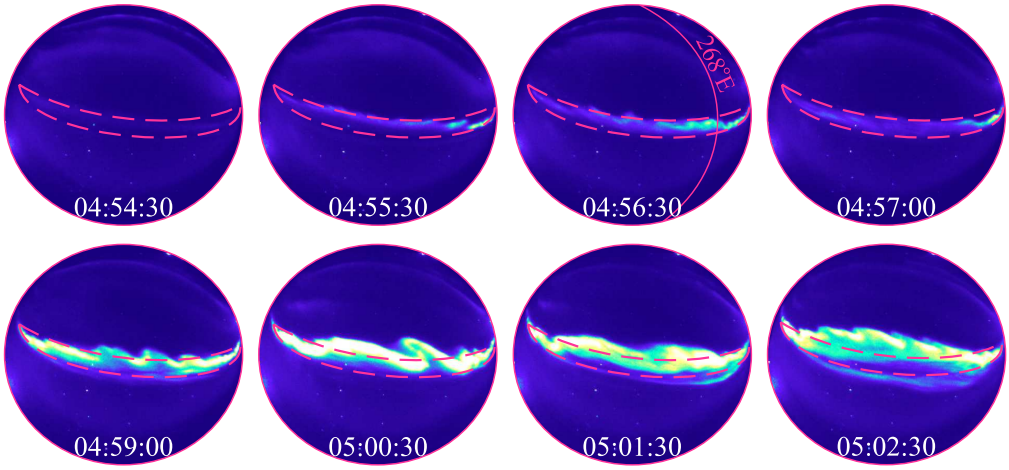

Figure 4.2: Auroral wave-like structure along the onset arc during the weak substorm observed at Gillam ASI (56.35° LAT, 265.34° LON) on 3 February 2008, in the raw (CCD) coordinates. AIB starts at 04:54:24 UT. It becomes visually observed at 04:55:30 UT. This brightening is widen in longitude within the red box. After 05:00:20 UT the aurora starts expand poleward out the red box, as can be seen at a later time (05:02:30 UT).

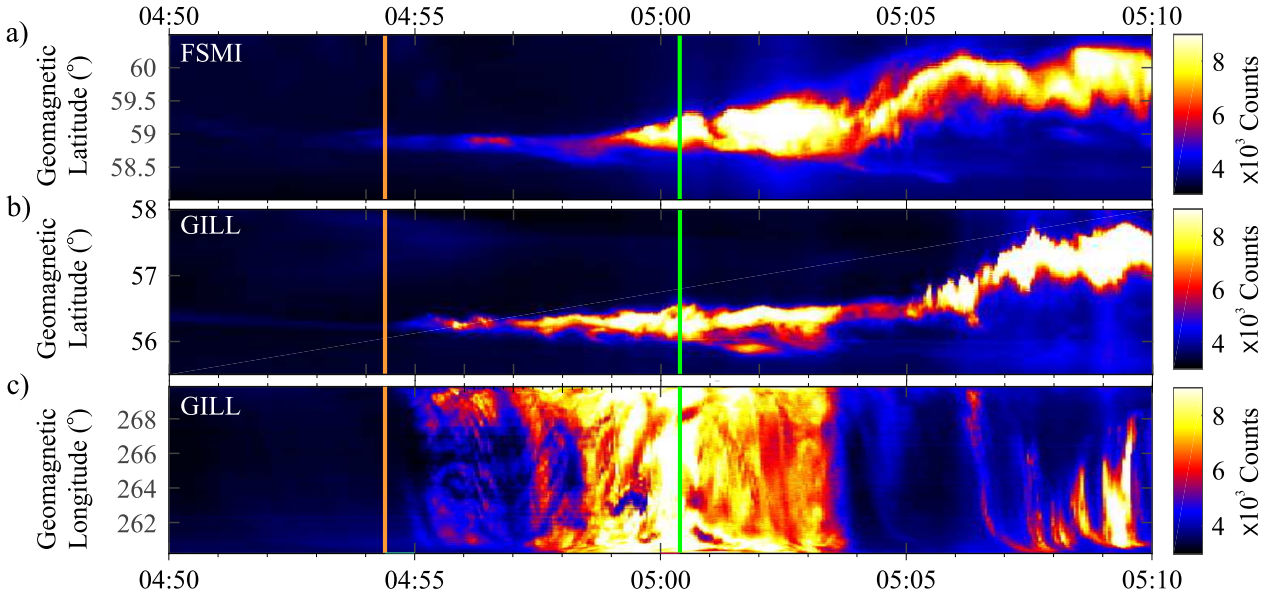

Figure 4.3: (a,b) North-south keograms at 250° and 268° of geomagnetic longitudes FSMI and GILL to show auroral brightening and poleward propagation. The orange and green vertical lines mark the AIB and initiation of PE. (c) East-west keogram along a line of geomagnetic latitude to track periodic azimuthal structure along the onset arc but at slightly different latitudes.

To get further information on spatial and time development of the auroral activation, Figure 4.3 shows the North-South and East-West keograms of the auroral arc on a larger time

interval, from 04:50 to 05:10 UT. They have been computed at a longitude of 268° and a latitude of ∼ 56.2° respectively (indicated by red lines in Figure 3). As seen in the North/South keogram, the first auroral light is precisely detected at 04:54:25, which correspond to AIB. The light then intensifies until ∼ 05:01:00, at about the same latitude. This also corresponds to a progressive westward expansion of the auroral arc. This first concerns GILL station only (see panel b), from 04:54:24 to ∼ 04:56. The arc is then successively detected by the different stations (Fig. 4.4) adjacent to GILL (FSMI, FSIM and INUV) so that, at 05:01:00, the arc extends on about 40° in longitude. At 05:00:20 and later, the arc expands in latitude with a fast poleward motion starting at ∼ 05:05. In general, these observations are consistent with the near-Earth initiation scenario of the substorm expansion, with plasma processes initiated on magnetic field lines linked to the most equatorward auroral arc (Akasofu, 1964; Roux *et al.*, 1991; Lui & Murphree, 1998; Perraut *et al.*, 2003).

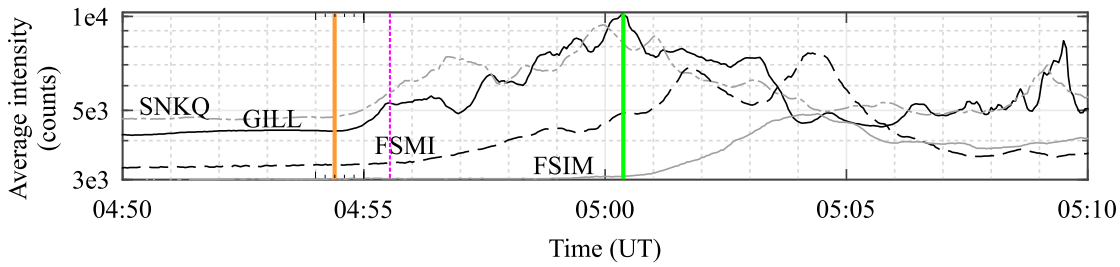

Figure 4.4: Temporal evolution of the average intensity along the onset arc seen by the all sky imagers at SNKQ, GILL, FSIM and FSMI (in unit of ASI detector). The orange and green vertical line marks the AIB and PE time.

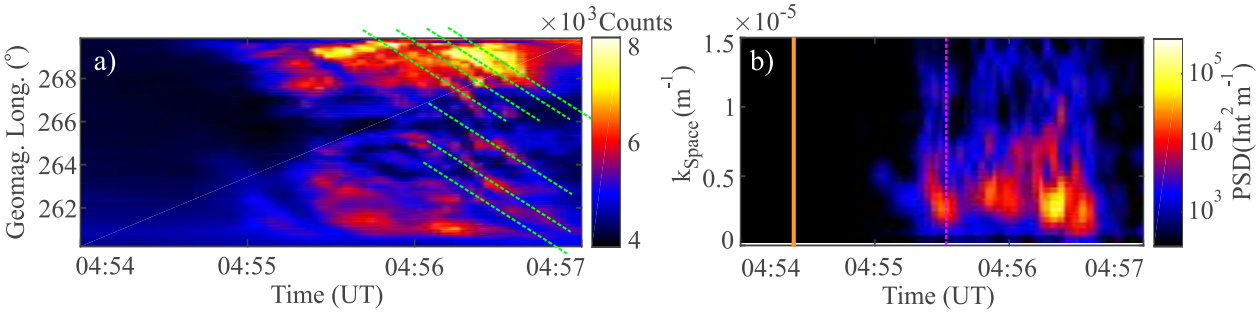

Figure 4.5: (a) Zoom: East-west keogram along a line of geomagnetic latitude. (b) Power Spectral Density (PSD) as a function of azimuthal wave number in the magnetosphere, k_{Space}. Dashed lines are drawn to guide the eyes and show the propagation of auroral structures.

The detailed analysis reveals that the arc develops as a wave-like structure during the first minutes following AIB. It can be seen at 04:56:30, for example, in Figure 4.2. This is shown with details in Figure 4.5 where a zoom of the East/West keogram is presented.

At 04:55:30 UT, $\sim$ 1.1 min after AIB and at longitude of $\sim 268°$, the wave-like structure appeared near the eastern edge of the FOV of GILL. Its characteristics can be determined around 04:56:30 when it develops in longitudes, from 264° to 268°. The wave-like structure propagates westward, with a drift of $\sim 4-5°$/minute, meaning $\sim 4-5$ km/s (1° of longitude corresponds to 62 km at GILL latitude). The longitudinal distance between two maxima of intensity is $\sim 0.8°$ which corresponds to a wavelength of $\sim$ 49 km. This can be determined with more details by computing the Power Spectral Density (PSD) of the keogram (Figure 4.5, panel b). Between 04:56:00 and 04:56:40, clear maxima of the PSD are obtained for k values ranging from 0.3 to 0.4×10^{-5} m^{-1}, which corresponds to wavelength of $\sim 1500 - 2000$ km in the magnetosphere. The period of the waves is $\sim 12 - 15$ s. The results of auroral data analysis are summarized in the Tab. 4.1. Additional calculations of these values can be found in the Section A.4.

Table 4.1: Spatial and temporal scales of the observed waves at 04:55:15 – 04:56:45 UT

Parameter	Ionosphere	Magnetosphere
Wavelength $\lambda_\perp$ (km)	49.4 ± 6.2	1647 ± 206
Speed $v_\perp$ (km/s)	~ 3.8	~ 127
Wave period (s)	~ 13	~ 13

This interpretation of the auroral sequence is supported by complementary observations (not shown). The signatures of Auroral Kilometric Radiation measured by GEOTAIL (not shown) confirm the onset timing. The detailed analysis of the individual high resolution magnetogram reveals the the substorm electrojet was initiated just eastward of the GILL station (in the vicinity of the Sanikiluaq and Kuujjuaq stations) and expanded very rapidly westward.

4.2 Magnetotail dynamics

In the present section, we consider the observations made by the three inner THEMIS satellites (TH-A, TH-D and TH-E) orbiting in the near-Earth magnetotail. As already mentioned, their magnetic footprints are located in the immediate vicinity of the area where the first auroral light is observed. The position of the three satellites is shown in Figure 4.6. They are located $\sim$ 1 R_E from each other, around the central position: $X_{GSM} \sim -10$ R_E, $Y_{GSM} \sim 1$ R_E and $Z_{GSM} \sim -3$ R_E. The average magnetic field seen by each satellite at 05:54:00, just before activation, is also presented. The measurement of a positive Bx_{GSM} shows that the

central part of the current layer is probably located south of the satellites and, therefore, that the current layer is significantly south of the normal position of the magnetic equator. The magnetic field is also strongly tilted in the Y direction, by almost $\sim 30°$. Given this distortion, we can consider that TH-A and TH-E are approximately at the same magnetic longitude, TH-A closer to the earth than TH-E, and that TH-E and TH-D are on the same L-shell, TH-D being at west of TH-E.

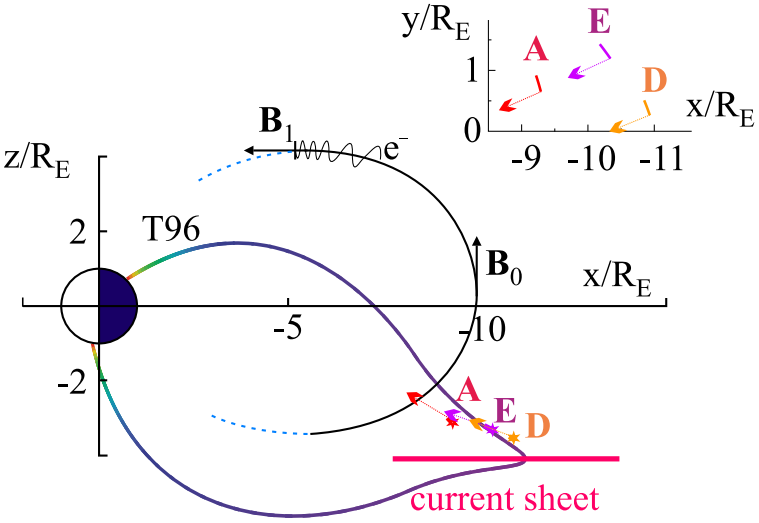

Figure 4.6: The locations of the THEMIS satellites in the GSM X-Z plane. The colored arrows indicate the magnetic field vectors at the substorm onset.

The magnetic field and the pressure are presented in Figures 4.7. For a few tens of minutes from $\sim$ 04:30, the magnetic field and the pressure gradually increased. This can be interpreted as an accumulation of magnetic energy in the magnetotail, as can be expected during the growth phase of a substorm. A plateau is reached around 04:50. The magnetic pressure is then maximum. This also corresponds to a minimum of the ion density and a maximum of the potential of the satellites (data not shown). The three satellites are then in the lobes, north of the current sheet. It is also an indication that the current sheet has strengthened and is thinner.

The first indication of high frequency magnetic fluctuations, with periods from a few seconds to a few tens of seconds, is observed by TH-A, a little before 04:54:30, and therefore simultaneously with the first auroral light. These fluctuations with magnitude of $\sim$ 4 nT are observed on the three components of the magnetic field. They are associated with a strong decrease in the Bx_{GSM} component, of the order of 15 nT, between 04:55 and 05:00. At the same time, the By_{GSM} component decreases by $\sim$ 5 nT and, thus, the Y distortion relaxes. The magnetic pressure decreases by $\sim$ 40%, from 0.7 nPa to 0.4 nPa. We conclude that

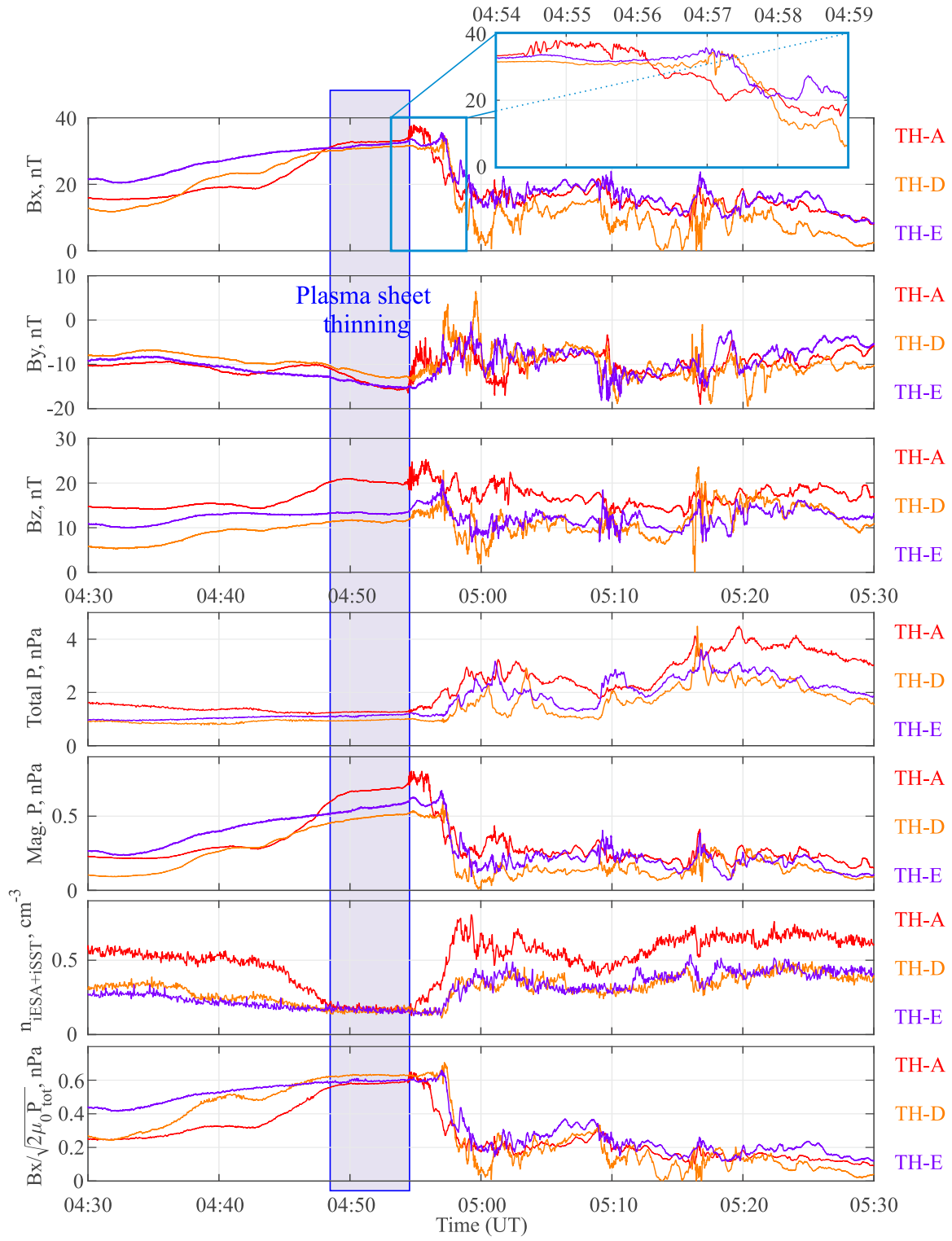

Figure 4.7: Upper 3 panels: Three components of the magnetic field in geocentric solar magnetospheric coordinates from TH-A, TH-D and TH-E satellites. Lower panels: The total (ion $p_i = k_B T_i n_i$ (ESA+SST) plus magnetic $p_m = B^2/(2\mu_0)$) and magnetic pressures, the ion density from ESA and SST, the profiles of $Bx/B_{lobes} = Bx/\sqrt{2\mu_0 P_{tot}}$ as indicator of the current sheet location in the normal (thickness) direction.

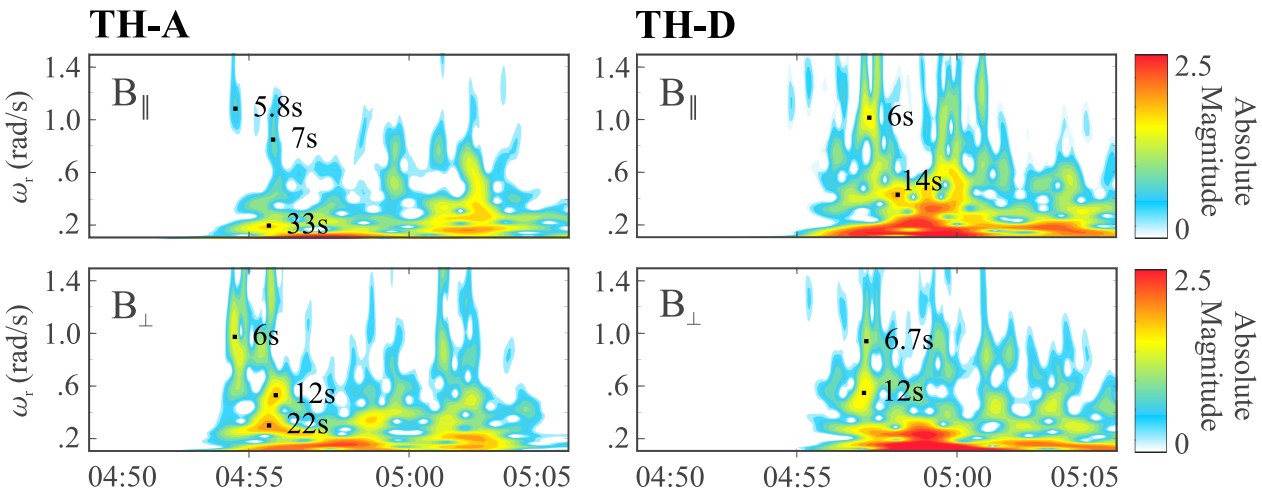

Figure 4.8: Frequency and time decomposition of parallel ($B_{\parallel}$) and perpendicular ($B_{\perp}$) magnetic field by wavelet analysis for TH-A and TH-D.

a magnetic dipolarization takes place from 04:55 to 05:00. A part of the magnetic energy accumulated in the plasma sheet has thus been dissipated while magnetic fluctuations of short periods have been generated.

The same time sequence is observed $\sim$ 2 minutes later by TH-E and TH-D. These two satellites simultaneously detect the high frequency magnetic fluctuations around 04:57:00, then each later observes the relaxation of the magnetic configuration. Detailed analysis shows, however, that TH-E and TH-D already observed a small changes of the magnetic field, starting from $\sim$ 04:54:30. These preliminary signs of plasmasheet small changes are not detected by TH-A, which observes the high frequency fluctuations suddenly. The fluctuations observed at $\sim$ 04:54:30 by TH-A therefore really mark the beginning of a destabilization. The destabilization is immediately detected by TH-E and TH-D, even if these two satellites see the high frequency fluctuations 2 minutes later.

In terms of timing and location, the instability of the current layer is thus triggered in the vicinity of TH-A, at 04:54:24, to gradually propagate tailward. This perfectly coincides with the AIB at $\sim$ 04:54:30, followed by the arc polarward motion and expansion in longitude. We thus conclude that the destabilization starts almost exactly at 04:54:24, at or extremely close to TH-A, and that the observed evolutions are temporal by nature. One notes that two activations characterized by the generation of high frequency oscillations are observed later, at $\sim$ 05:10 and 05:17. Both of them are also followed by slow decreases of Bx and thus dipolarizations. They are, however, modest compared to the first.

In Figure 4.8, the wavelet transform of the components parallel and perpendicular to the mean field are shown. At the start of the activation, around 04:55 (TH-A), the $B_{\perp}$ fluctuations

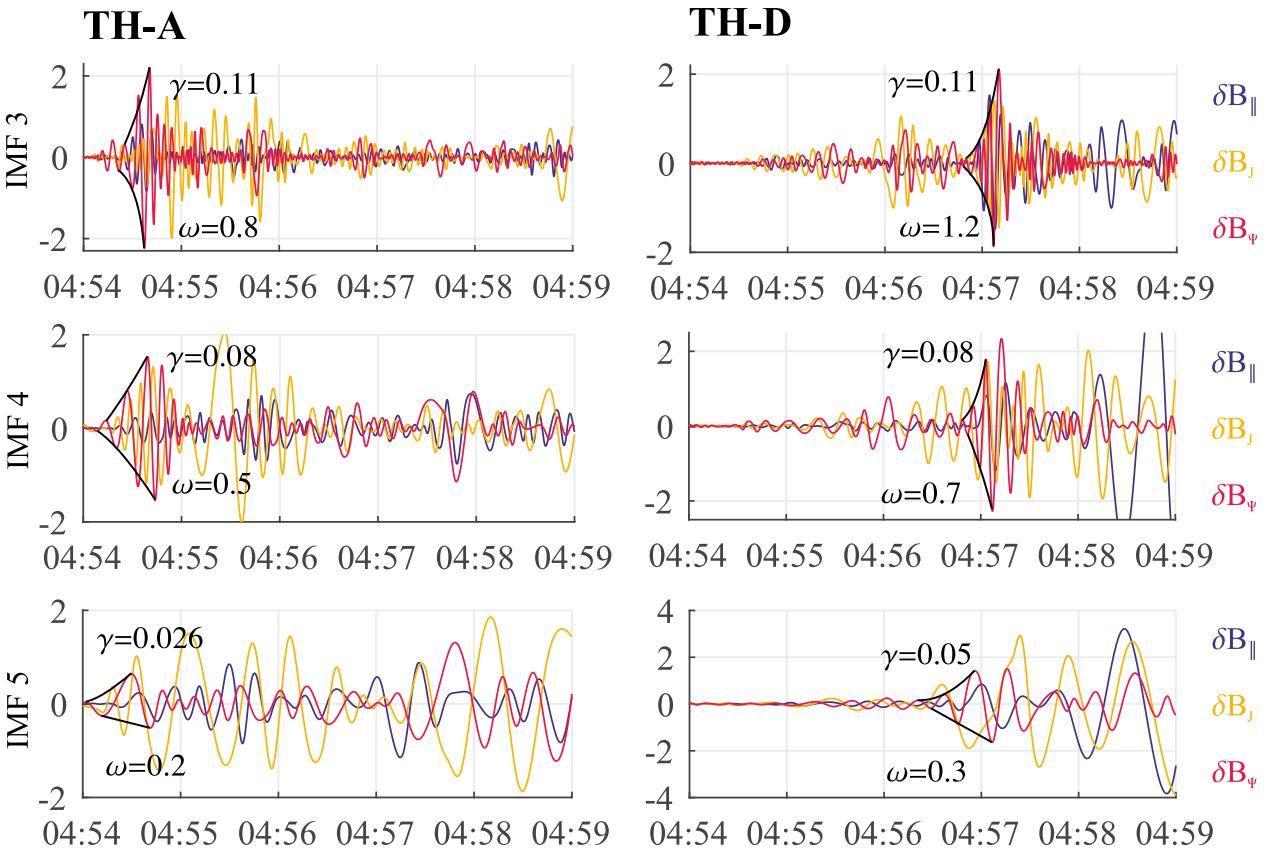

Figure 4.9: Hilbert-Huang wavelet transform for TH-A, TH-D and TH-E in the natural field-aligned coordinates system.

show three spectral peaks, centered at periods of 6 s, 12 s and 22 s. It is interesting to note that these periods are of the same order as those observed in the auroral flux. The peaks last for a few tens of seconds to $\sim$ 2 minutes at periods larger than 20 s. Smaller peaks are also observed at 04:59 and 05:01:30. The parallel component is systematically smaller than the perpendicular one. The fluctuations thus present a dominant perpendicular polarization. The same phenomenology is observed with TH-D, with a delay of $\sim$ 2 minutes. In particular, one notes the strong peak centered at periods of 12 s, seen on $B_\perp$ only at 04:57. At the same time, a peak is observed around 20 s with TH-D.

A complementary view of the nature of the oscillations can be obtained by applying a Hilbert-Huang Transform (HHT) to the fluctuations. They are projected in a natural frame [1]

[1] The natural field-aligned coordinates system $(\vec{e}_\psi, \vec{e}_J, \vec{e}_\parallel)$ defined by

$$\vec{e}_\parallel = \vec{B}/B, \quad \vec{e}_J = \vec{J}/J, \quad \vec{e}_\psi = \vec{e}_J \times \vec{e}_\parallel, \tag{4.1}$$

where $\vec{B}$ and $\vec{J}$ are vectors of magnetic field and the normal current density projection on XY-plane at 04:30 UT. The current density along the normal to the three THEMIS spacecraft plane $(\vec{j}_n)$ can be calculated

more suitable for comparison with theoretical calculations. The three components $\delta B_{\parallel}$, δB_Y, and δB_Ψ are considered. δB_Y is defined as the projection of $B_\perp$ in the X-Y GSM plane and δB_Ψ is perpendicular to both $\delta B_{\parallel}$ and δB_Y. The HHT is an iterative procedure that extracts oscillatory-like features from the data. Compared to Fourier or wavelet analysis, HHT is better adapted to process non-stationary and non-linear data. The HHT relies on an empirical mode decomposition (EMD), which decomposes a signal into intrinsic mode functions (IMFs). B_Y definition, an IMF is any function with the same number of extrema and zero crossings, whose envelopes are symmetric with respect to zero. The Hilbert transform is then applied to the IMFs to generate an energytimefrequency spectrum. This is used here to estimate the growth rate of the oscillation.

In figure 4.9, several IMFs are shown. According to the HHT procedure, each successive IMF contains components of longer periods than the proceedings. The peak amplitude of the magnetic field perturbations is observed at 04:54:40 by TH-A and at 4:57:00 by TH-D (and TH-E). The highest peaks are seen in the δB_Ψ component. Oscillations with periods of 7.8 s and 12.5 s are identified in the fluctuations observed by TH-A, with growth rates of 0.11 s^{-1} and 0.08 s^{-1}, respectively. Periods of 5.2 s and 8.9 s are observed from TH-D measurements, with again growth rates of 0.11 s^{-1} and 0.08 s^{-1}. (TH-E measurements are not much different from TH-D ones.)

To summarize the observations, exactly at the time of the auroral activation, at 04:54:24 (AIB), TH-A located closest to the Earth detects magnetic fluctuations of high amplitude ($\sim$ 4 nT), with periods of 6 s , 12 s and 22 s. Using HHT, their growth rates are estimated to be in the range $0.05-0.1$ s^{-1}. Modulations of similar periods characterize the wave-like evolution of the auroral arc. These modulations move west at a speed of $\sim$ 120 km/s (projected at $L \sim 10$), with a wavelength of $\sim$ 1700 km. The generation of these fluctuations also marks the beginning of a dipolarization. The same phenomena are observed 2 minutes later by TH-D and TH-E, which suggests a tailward (or polarward in the ionosphere) propagation of the active region.

4.3 Comparison with the kinetic theory

The HHT method can be applied to all the fluctuations observed by the 3 THEMIS satellites, between 04:54:00 and 05:02, which makes it possible to determine additional oscillatory components and to estimate both their periods and the growth rates. This is compared to

as $\mu_0 \vec{j}_n = \nabla_1 B_2 - \nabla_2 B_1$, where $\nabla_1 B_2 = 1/(N w_1) \sum_\alpha B_{\alpha 2} r_{\alpha 1}$ and $\nabla_2 B_1 = 1/(N w_2) \sum_\alpha B_{\alpha 1} r_{\alpha 2}$ are the two components of the gradient of magnetic field within the spacecraft plane, $w_{1,2,3}$ are three nonnegative eigenvalues of volume tensor $R_{jl} = 1/N \sum_{\alpha=1}^{N} r_{\alpha j} r_{\alpha l}$.

the theoretical predictions in Figure 4.10, for values of the parameter that are consistent with the present observation (Tab. 4.2).

Table 4.2: Spatial and temporal scales characterizing particle dynamics in the Earth plasma sheet at $L = 10$ ($B_0 = 11$ nT). They are deduced from observations (see section 4.4)

Parameter	Ion	Electron
Temperature T_α (keV)	4	1.4
Thermal velocity $V_\alpha = \sqrt{2k_B T_\alpha / m_\alpha}$ (km.s^{-1})	875	22000
Larmor radius $\rho_{L,\alpha} = m_\alpha V_\alpha / (eB_0)$ (km)	830	12
Cyclotron period $2\pi m_\alpha / eB_0$ (s)	6	3×10^{-3}
Half bounce period $\tau_{b,\alpha} \simeq \pi/2\sqrt{1+\epsilon}\, \ell_0 / V_\alpha$	2.7 min	6.38 s
Alfvén velocity $c_A = B_0/\sqrt{\mu_0 n_0 m_i} = 640$ km/s		

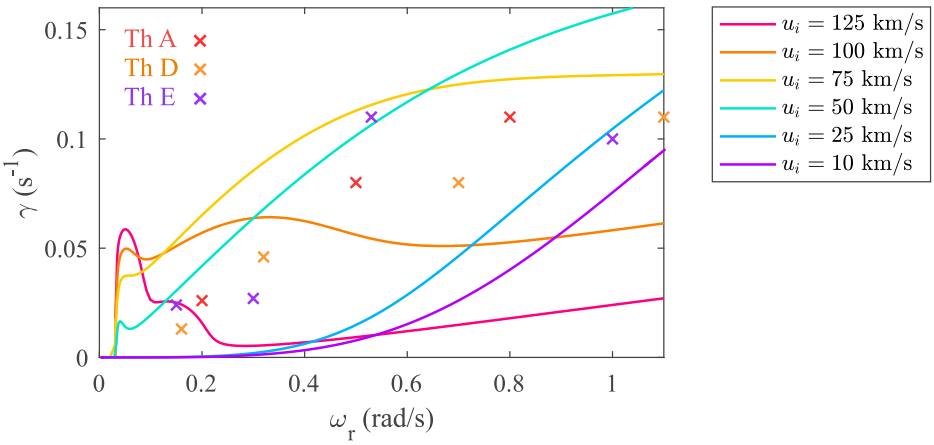

Figure 4.10: Growth rate γ as function of frequency ω_r for varying ion density diamagnetic drift. The exponential growth rates of the peak amplitude of the δB_Ψ perturbations observed by TH-A TH-D and TH-E spacecrafts are marked with crosses.

The first remark is that the growth rates estimated from the observations compare well with their theoretical predictions. There are however two possibilities of interpretation. The first is to note that the estimates are all between the two theoretical curves corresponding to drift of 25 and 50 km/s (in blue). This suggests that a drift of ~ 40 km/s, typically, would be enough to trigger the instability. The second possibility is, on the contrary, to consider much higher drifts. As seen in the figure, for $\omega > 0.5$ s^{-1}, drifts between 75 and 100 km/s (in yellow and orange) will also be compatible with the estimates and, for $\omega < 0.5$ s^{-1}, drifts of $100 - 125$ km/s (in orange and red) are acceptable as well. To discuss the consequences of these two choices, one can consider the dispersion curves in Figure 4.11.

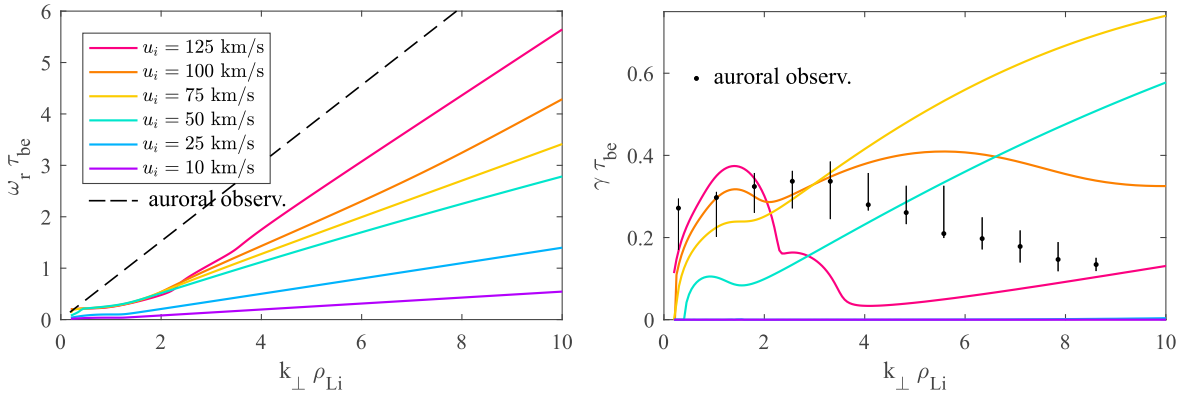

Figure 4.11: Normalized frequency $\omega_r \tau_{be}$ and growth rate $\gamma \tau_{be}$ as functions of wave number $k_\perp \rho_{Li}$ for the electromagnetic drift unstable mode with the near-Earth (at $L = 10$) plasma sheet parameters (in model Tab. 4.2) and varying ion diamagnetic drift. Auroral observation curves obtained in the Section A.4

This mode propagates in the direction of the ion drift (the positive y direction here), at phase speed close to the ion drift. In normalized quantities, the frequencies between 0.6 and 1 correspond to $\omega\tau_{be}$ between 3.8 and 6.4. For a drift of ~ 40 km/s, this implies $k\rho_{Li}$ between 15 and 23, or wavelengths between 230 and 350 km in the magnetosphere ($\sim 7 - 10$ km in the ionosphere). This is a factor 2 to 3 times less than the Larmor radius at the equator, which does not conform to the model's assumptions. For a drift of ~ 100 km/s, $k\rho_{Li} \sim 8-15$ which corresponds to wavelengths between 350 to 620 km in the magnetosphere ($\sim 10 - 20$ km in the ionosphere). It is still less than the Larmor radius, but by a factor of 1 to 2 which is more in line with the limits of the model. For low frequencies, $\omega \sim 0.2$ rad/s ($\omega\tau_{be} \sim 1.3$), we will have $k\rho_{Li} \sim 4.5$ and a wavelength of ~ 1160 km in the magnetosphere (38 km in the ionosphere) if the drift is ~ 40 km/s. For 100 km/s, $k\rho_{Li} \sim 3$, corresponding to 1750 km in the magnetosphere (58 km in the ionosphere). As already mentioned, this is the typical scale of the oscillations of the auroral arc.

If we change some plasma parameters (Tab. 4.3) to make the azimuthal magnetospheric wavelength comparable to the ion gyroradius $\rho_{Li} = 1703$ km (according (Kalmoni *et al.*, 2015)), our dispersion relation can reproduce the characteristic linear relationship between angular frequency and spatial scales of auroral wave-like signatures. In this case, together with magnetic field ($B_0 = 6$ nT) we reduced the total density ($n_0 = 0.035$ cm^{-3}) in order to keep the regime in the near-Earth plasma sheet low-beta ($\beta \sim 0.55$).

For values of modified parameters (Tab. 4.3), dispersion curves are presented in figure 4.12.

The assumption of a drift threshold of ~ 40 km/s therefore leads to wavelength estimates

Table 4.3: 3 parameters that were changed in the model.

Parameter	In satellite observations (Fig. 4.10)	Modified (Fig. 4.12)
Total density n_0 (cm^{-3})	0.14	0.035
Ion temperature T_i (keV)	4	5
z-component of magnetic field B_0 (nT)	11	6
Ion larmor radius $\rho_{Li} = m_i V_i/(eB_0)$ (km)	830	1703
$\beta = 2\mu_0 n_0 T_e/B_0^2$	0.65	0.55
Alfvèn speed $c_A = B_0/\sqrt{\mu_0 n_0 m_i}$ (km)	640	700

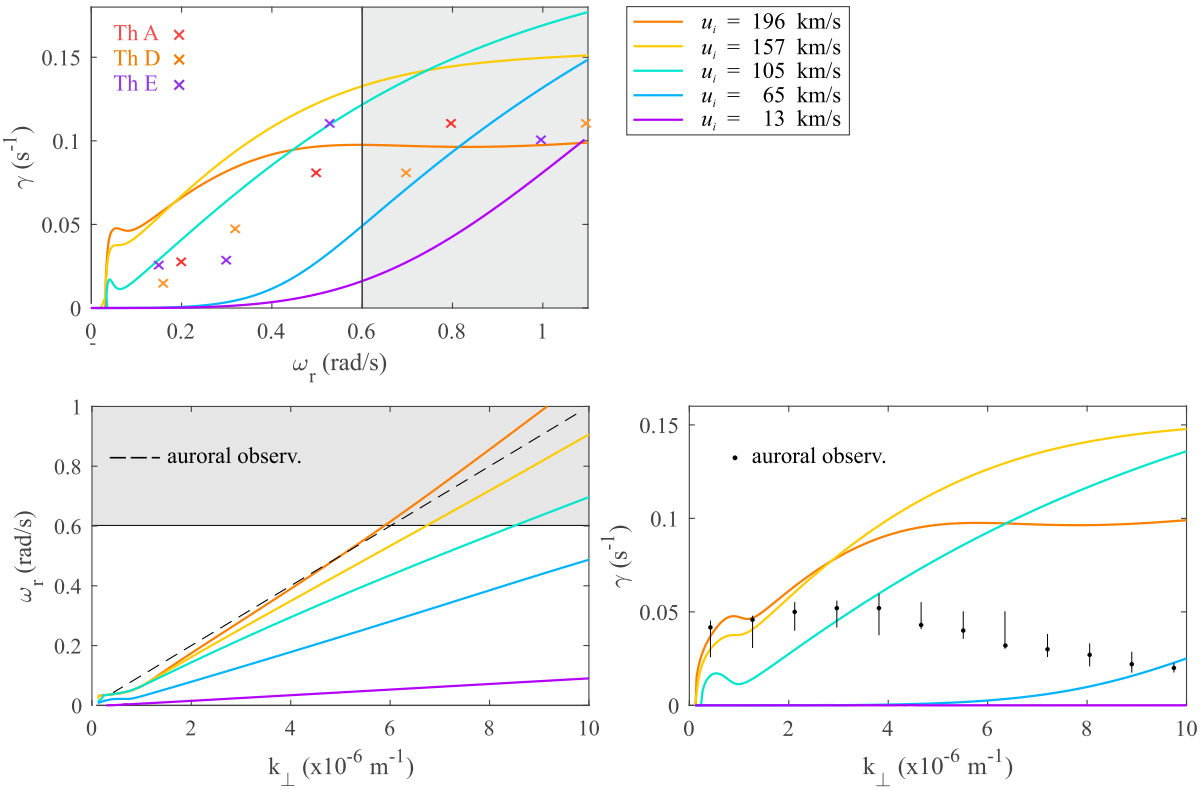

Figure 4.12: Growth rate γ as function of frequency ω_r for varying ion density diamagnetic drift. Normalized frequency $\omega_r \tau_{be}$ and growth rate $\gamma\tau_{be}$ as functions of wave number $k_\perp \rho_{Li}$ for corresponding ion diamagnetic drift. The frequencies in the shaded region are influenced by the ions' cyclotron movement, neglected by theory ($\omega \ll \omega_{ci}$). Auroral observation curves obtained in the Section A.4

that do not conform to the limits of the model. It does not prove, however, that this is not possible. On the other hand, the assumption of a threshold at $\sim$ 100 km/s leads to estimates

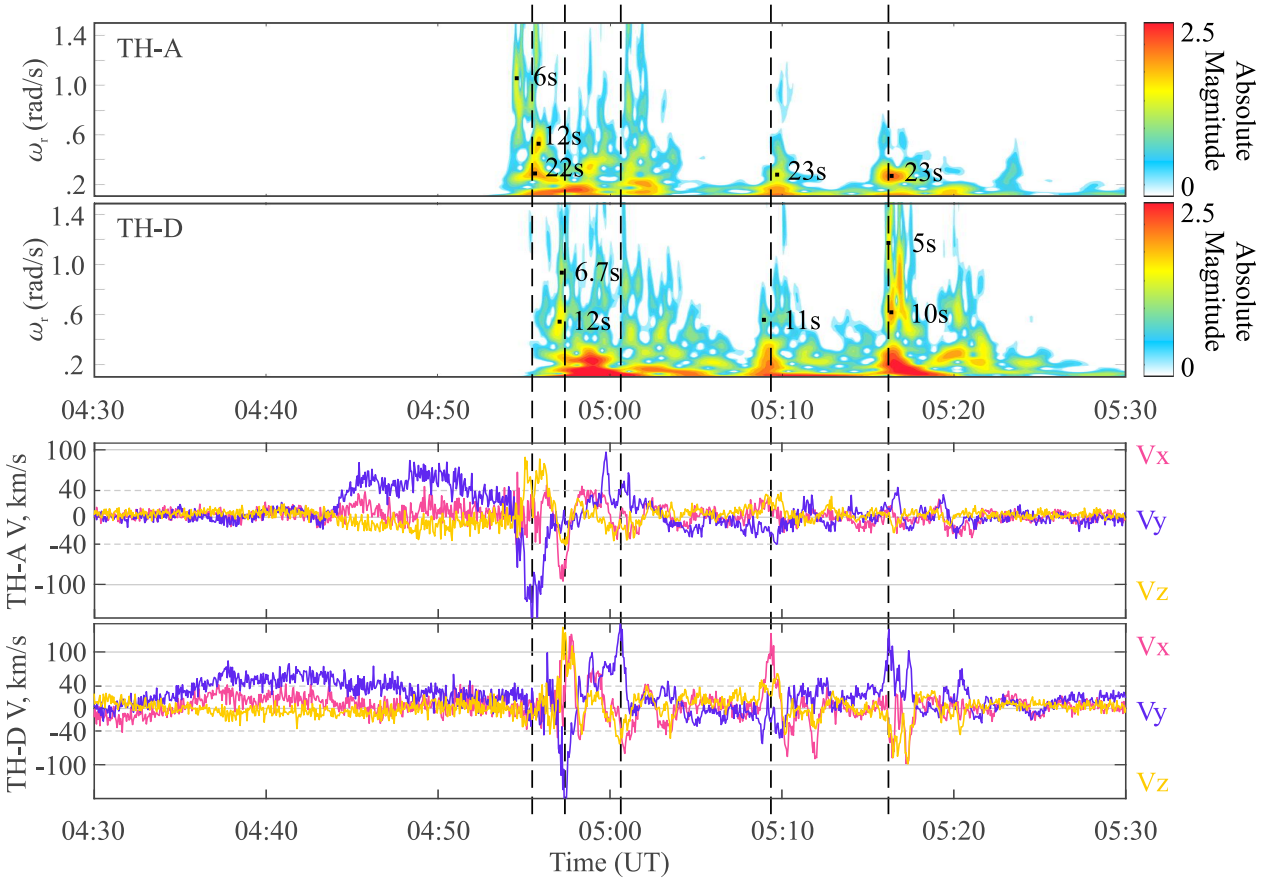

Figure 4.13: Comparison between magnetic fluctuations ($B_\perp$) and ion velocity, from 04:30 to 05:30. Upper panels: wavelet transform of the magnetic fluctuations. Lower panel: Ion velocity.

of wavelengths at low frequencies close to the observations of oscillations of the auroral arc and, more generally, to estimates more in agreement with the limitations of the model.

One way to resolve the dilemma is to analyze how variations in ion drift velocity, or more simply $V_\perp$, correlate with the appearance of magnetic fluctuations. This is shown in Figure 4.13 for the period 04:30–05:30. The wavelet analysis shows that the fluctuations are organized into 3 or 4 short bursts, lasting 1 to 3 minutes each (depending on the periods). As seen in Figure 4.13, the variations of $V_\perp$ present the same time organization. Obviously, there is a correspondence between the bursts in fluctuations and the time intervals of large $V_\perp$. For TH-A as for TH-D, the first burst is correlated with the first observation of $V_\perp$ greater than 100 km/s, around 04:55 (TH-A) and 04:57 (TH-D). It should be noted that in these 2 cases, Vy is initially negative, which is opposite to the direction of the current in the sheet. A simple explanation is that the satellites initially in the lobes are entering the layer. The observed drift is then mainly a magnetic gradient drift, in the negative Y direction.

This indicates, however, that the layer is particularly thin and that the diamagnetic drift is expected to be particularly important at that time. Deeper in the sheet, the measured drift is in the positive Y direction as expected for diamagnetic effect. Two other bursts are observed simultaneously by TH-A and TH-D, at $\sim$ 05:09 and 05:17, each one being correlated with an increase in $V_\perp$. They reach 100 km/s for TH-D when they remain more limited for TH-A. Not surprisingly, the magnetic fluctuations are also more intense for TH-D, in particular around 05:17.

$V_\perp$ is here interpreted as a proxi of the drift. A fine analysis of the distribution functions would be necessary to better quantify the fraction which would be linked to the diamagnetic effect. In conclusion, observations show that there is a strong link between increases in $V_\perp$ and the appearance of magnetic fluctuations which is consistent with the model of the electromagnetic drift-bounce instability.

Is it possible to identify a threshold beyond which the instability starts. In Figure 4.13, the 40 km/s and 100 km/s thresholds are plotted. As already discussed, these are the drifts for which the theoretical frequency/growth rate curves best explain the observations. Clearly, the 40 km/s threshold is very often approached or exceeded without the generation of fluctuations. In particular, before substorm onset, from 04:37 to 04:52, while TH-A and TH-D are in the plasma sheet, $V_\perp$ is close to $70-80$ km/s without magnetic fluctuations nor auroral arcs being observed. Conversely, by considering a threshold of $90-100$ km/s, the time intervals of strong drifts remarkably correlate with the magnetic fluctuations. In addition, the theory then remarkably predicts both the observed frequencies and growth rates.

4.4 Conclusion

To assess the interest of a new theory of kinetic instability in 2D current sheets, we compared the theoretical predictions with the observations made by THEMIS during a low intensity substorm. The theory considers the amplification of electromagnetic waves by a combined effect of ion drift and interaction with electrons performing bounce motion in the current sheet (electromagnetic drift-bounce instability). The theory is adapted to low β regimes ($\beta < 1$). The selected event (February, 3, 2008, around 05:00) corresponds to a modest auroral activation that can be interpreted as a small substorm. It is interesting by the excellent magnetic connection between the location of the first auroral light, observed by GILL station, and TH-A, TH-D and TH-E, located in the near-Earth magnetotail at $\sim$ 10 R_E.

With perfect timing, the first auroral light corresponds to the first magnetic fluctuations

observed by the satellite closest to Earth (TH-A). Two minutes later, as the auroral arc has developed, the fluctuations are observed by the more distant satellites (TH-D and TH-E). The analysis of the fluctuations shows that they contains oscillatory components with periods ranging from 7 s to 20 s. This is also the domain of the pulsation of the auroral arc (13 s). The dominant polarization of the fluctuations is perpendicular to the average magnetic field, the Ψ component (component normal to the magnetic shell) being often the largest. By applying HHT method, the growth rates of the oscillatory components are estimated. They vary between 0.05 s^{-1} and 0.1 s^{-1} depending on their periods. It is not possible to estimate the wavelengths with the present observation, the only indication is that the auroral arc has a wave-like structure with a characteristic length of 1700 km. Finally, the fluctuations are organized into bursts lasting 1 to 3 minutes, which correspond precisely to the time intervals during which the ion $V_\perp$ (the combination of all drifts) exceeds $90 - 100$ km/s.

The theoretical predictions agree remarkably well with these observations. Considering values of the plasma parameters consistent with the observation, the theory indeed predicts that electromagnetic drift waves are unstable, at the observed frequencies, growth rates, and polarity, for drift exceeding 90 km/s.

This work could be improved from a theoretical point of view by taking into account the curvature drift effects and by generalizing to a full electromagnetic situation ($\beta > 1$). From an observational point of view, the model needs to be confirmed with more cases, using THEMIS, MMS and also CLUSTER to better estimate the wavelengths and the polarization. It is also necessary to examine finely the distribution functions to asses to what extent the measured $V_\perp$ can be interpreted as a diamagnetic drift. The last point is obviously to understand how these waves may dissipate part of the current contained in the sheet and therefore a part of the accumulated magnetic energy. Note, however, that in the present case, these fluctuations constitute the first sign of destabilization of the layer and therefore of triggering of the substorm.

Chapter 5

Radiation environment during geomagnetic reversal

The present magnetic epoch (the period between magnetic polarity changes), which is known as the Brunhes epoch, started about 780 thousand years ago, after the Matuyama epoch (Gubbins, 1994; Jacobs, 1994; Gubbins & Kelly, 1995; Soler-Arechalde *et al.*, 2015). Detailed research has established that short periods of polarity changes, so-called episodes, occurred inside the epochs. For example, during the Matuyama epoch, the Jaramillo episode is known to have happened about one million years ago, in which the magnetic field reversal lasted for about 60 thousand years, a relatively short time interval. The magnetic reversals are thought to occur chaotically (Jacobs, 1994). The periods between them can last from several dozen thousand years to several million years. The reversal itself can last from 100 years (with a dipole inclination decay of about 2° per year according to Sagnotti *et al.* (2014)) up to approximately 5-10 thousand years (Glassmeier *et al.*, 2009*a*,*b*; Glassmeier & Vogt, 2010).

As a rule, the magnetic field reversals occur against the background of a significant weakening of the geomagnetic field, which started before the polarity changes. Prior to the polarity change, the amplitude of secular variations increases (Gubbins & Kelly, 1995; Hoffman, 1992). The motion of the virtual magnetic pole (the line connecting the North and South Magnetic Poles) during the reversals is rather chaotic but occurs within a limited longitude band. During the reversals, Earth's magnetic field (also called paleomagnetic) is most likely multipole and can be described by models based on the geomagnetic dynamo mechanism (Jacobs, 1994; Kida & Kitauchi, 1998; Olson *et al.*, 2009; Sheyko *et al.*, 2016). In several papers, magnetic field models are used to reconstruct the structure of the magnetosphere during the geomagnetic field reversals and to assess their impact on the circumterrestrial space (for example, using magneto-hydrodynamic (MHD) models as presented in papers (Glassmeier

& Vogt, 2010; Vogt *et al.*, 2004; Glassmeier *et al.*, 2004; Stadelmann *et al.*, 2010)). It should be noted, however, that the effect of the geomagnetic field reversals on the global structure of the magnetosphere, on the system of electric currents in it and on the magnetospheric plasma content is far from fully understood.

That a new magnetic field reversal is possibly starting now can be inferred from magnetic field changes over the last hundred years. The figure 5.1 suggests that a significant shift in the location of the magnetic poles (the points on the conventional surface of Earth at which the magnetic field is strictly normal to the surface) is occurring during this period: the North and South Poles have shifted by more than 2000 km and 1000 km, respectively. Here, the change in the location of the 'geomagnetic' poles of the central and shifted dipoles (the points at which the dipole axis crosses Earth's surface) is not very large. At the same time, the magnetic dipole moment has decreased by 7.5%, while the contribution from the high-order harmonics of the magnetic field, in contrast, has increased by $\sim$ 50%. In the preceding several centuries, the rate of the weakening of the dipole field was 5% per century (Merrill & McFadden, 1999). These data enable us to suggest that the reversal process will not appear to be a literally 'dipole overturn', but a transformation of the dipole into a multipole (and eventually the formation of a new dipole with the opposite location of the poles).

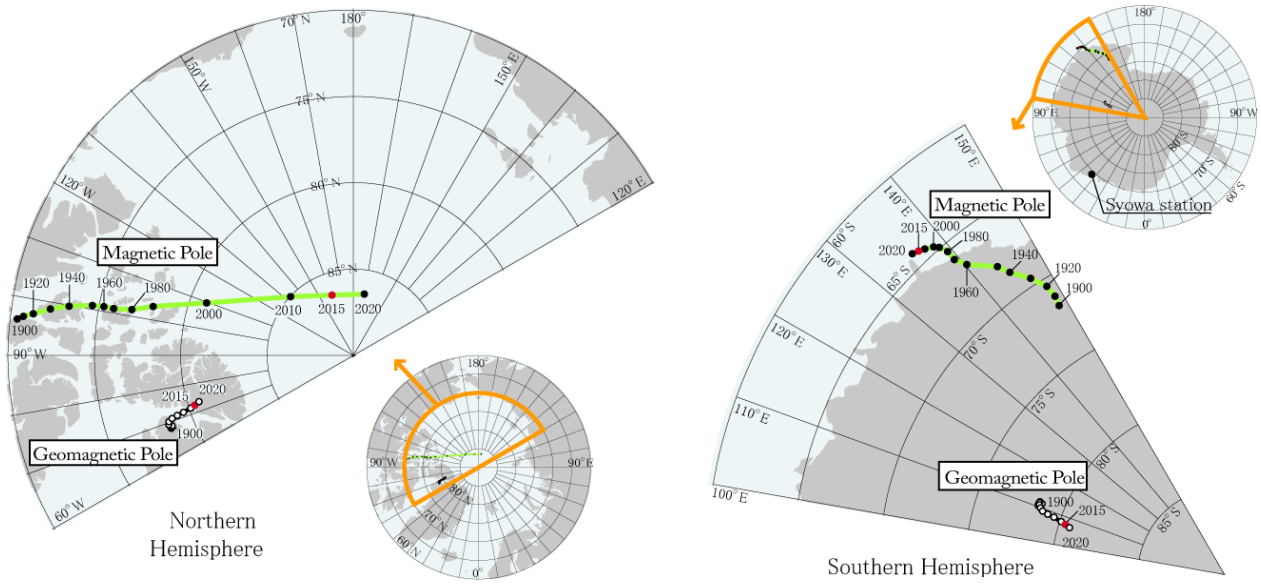

Figure 5.1: Changes in the locations of north and south magnetic poles.

A detailed picture of magnetic field behavior during reversals is absent because of the complexity of analysis of paleomagnetic data and the long timescales of these events (Merrill & McFadden, 1999; Valet & Meynadier, 1993). The geomagnetic field is known to have a quadrupole component, in addition to the dipole one, as well as higher-order multipoles.

There is some evidence that the total energy of the magnetic field does not vary significantly during reversals, i. e., part of the energy of the dipole magnetic field can be redistributed among higher-order multipole moments (Williams & Fuller, 1981; Clement & V., 1985; Clement, 1991). However, the amplitudes of these components rapidly decrease with distance, and in the case of diminishing of the dipole component during reversal, the quadrupole component will become dominant. Some data (see, for example, Clement & V. (1985)) suggest that during certain reversals with dipole decay, the quadrupole component could dominate and its amplitude increase by about 10% compared to the presentday level. Such was a possible magnetic field configuration during the Jaramillo reversal (Clement & Kent, 1984).

Geomagnetic reversal is a relatively rare event that has never occurred during the era of homo sapiens on Earth, so its inevitable advent clearly causes some trouble and poses the question of the radiation hazard for humans during the reversal. The issues of the cosmic radiation hazard for the bio- and technosphere, the 'blow-off' of Earth's atmosphere to outer space, ozone layer disappearance and other elements of a possible ecological catastrophe, which are frequently discussed in the literature and by the mass media, are beyond the scope of the present study.

In this part of thesis, we study the flux levels of galactic and solar cosmic ray (GCR & SCR) protons and the radiation safety on Earth and in the circumterrestrial space during magnetic reversal using the most realistic scenario (a decrease in the magnetic dipole field by 10% or to zero during the reversal). To justify the reversal regime, we construct a geomagnetic dynamo model to estimate the general trend in the changes of the geomagnetic field multipolar components. Based on extrapolation of the field decomposition coefficients, we estimate when the reversal will begin, the dipole field will vanish, and later the sign of the magnetic field will change across Earth's entire surface. Using a numerical model of Earth's magnetosphere during the reversal and by integrating trajectories of GCR/ SCR particles, we estimate radiation doses at altitudes of 400 and 100 km, as well as on the ground level. We also estimate the regions of precipitation of energetic particles onto Earth's surface.

5.1 Cosmic rays

An important factor affecting the formation of the upper atmosphere and ionosphere of Earth and undoubtedly impacting the biosphere is the incoming flux of galactic cosmic rays (GCRs) — atomic nuclei accelerated to energies from 10^9 to 10^{20} eV. GCRs consist of 90% protons, 7% alpha-particles, and 3% charged nuclei with $Z > 2$ and electrons. In the whole, Earth's

magnetic field deflects charged particles; therefore, only particles with energies exceeding some threshold value can enter the atmosphere. For example, at a latitude of 50° north, the magnetic cut-off (the threshold energy of particles) is 0.66 GeV for protons, and 1.3 GeV for alpha-particles. The magnetic cut-off value depends on the latitude: it is higher at the equator than near the magnetic poles. Charged particles with energies below the threshold ones are mostly captured by the magnetosphere and are distributed inside it by filling the magnetospheric structures: Van Allen belts, the plasma sheet of the tail, the ring current, etc.

At altitudes on the order of several dozen kilometers from the ground, primary cosmic rays strongly interact with atomic nuclei of the air to produce pions (π), kaons (K), nucleon-antinucleon pairs, hyperons, and other elementary particles. The charged pions ($\pi^{\pm}$) produced either decay to form muons and neutrinos or further interact with nuclei. At ultrahigh energies of the primary particles ($E > 10^5$ GeV), the number of secondary progeny particles that form so-called extensive air showers (EASs) in nuclear and electronphoton cascades in Earth's atmosphere becomes as high as $10^6 - 10^9$. Thus, the impinging of GCRs into the atmosphere can initiate the development of cascades of nuclear active particles, as well as electronphoton cascades. The maximum muon generation occurs at altitudes of $\sim$ 10–20 km. Fluxes of high-energy muons are weakly absorbed in the atmosphere; therefore, secondary cosmic radiation at sea level mostly consists of muons (the hard component with an intensity of $J_\mu = 0.82 \times 10^{-2}$ cm^{-2} s^{-1} sr^{-1}), electrons, and photons (the soft component with an intensity of $J_v = 0.31 \times 10^{-}2$ cm^{-2} s^{-1} sr^{-1}).

The spatial distribution of these fluxes in the terrestrial magnetosphere depends on the geomagnetic field configuration, and their value is determined by solar activity and the perturbed state of the geomagnetic field. The GCR intensity is established to change by a factor of two in counter phase with the solar activity. This is due to the fact that during periods of maximum solar activity, the perturbed heliospheric magnetic field deflects charged particles incoming from deep space. During the solar activity minimum, the cosmic radiation intensity is about $J \sim 0.2$ cm^{-2} s^{-1} sr^{-1}, and during the solar maximum, it is $J \sim 0.08$ cm^{-2} s^{-1} sr^{-1}. Nuclear interactions of the GCR particles with atmospheric atoms ultimately change its composition and density. The atmosphere characteristics also change due to precipitation of particles captured in the Van Allen radiation belts. Thus, to analyze and forecast the atmospheric state, the spatial distribution and energy spectra of GCR particle fluxes should be known. To do this, numerical models have been elaborated that take into account the change in charged particle fluxes, depending on the solar activity. Such models should be used jointly with the model of charged particle penetration into Earth's magnetosphere.

The terrestrial magnetosphere is a target not only for GCRs, but also for solar cosmic rays (SCRs), which are accelerated charged particles ejected from the Sun by solar flares or during decays of prominences. The ejected particles (protons, electrons, and light nuclei with an energy from 0.1 MeV to several hundred MeV and even several dozen GeV) can reach Earth's orbit after interacting with the interplanetary medium. The effect of SCR on Earth's magnetosphere mainly appears either at high altitudes [for example, in the orbit of the International Space Station (ISS)] or indirectly through filling of the Van Allen belts, magnetospheric storms, polar precipitations of particles, etc. The intruding SCRs into the ionosphere at polar latitudes can lead to additional ionization and corresponding worsening of short-wavelength radio communications. There is evidence that SCRs can significantly damage the terrestrial ozone layer. Enhanced fluxes of SCRs can also be important sources of radiation hazard for astronauts and equipment on board space vehicles. As for the radiation hazard on Earth, most SCRs, being less energetic than GCRs, are cutoff by Earth's magnetic field and are absorbed in the atmosphere; therefore, SCRs cannot significantly affect the terrestrial radiation background.

5.2 Geomagnetic dynamo model

The magnetic field evolution during the reversal can be calculated using dynamo models (Jacobs, 1994). As there is no clear understanding of the flow of matter in Earth's interior, the dynamo models can reproduce different scenarios of the magnetic field evolution during the reversals, depending on the assumed behavior of matter in the liquid core of Earth. Estimates show that the diminishing of the geomagnetic field during reversal results in an increased GCR flux in the inner magnetosphere and an enhanced GCR/SCR flux intensity near Earth, in particular at altitudes of the trajectories of space satellites and the ISS.

To study geomagnetic field reversal regimes, we have used a nonlinear $\alpha\Omega$-dynamo model described in Popova (2016*b*) [see equations (1), (2)], taking into account that the radius restricting the outer liquid core of Earth, where the magnetic field generation takes place, is about 1/3 of the planet's radius. We have analyzed the parametric space for the dipole and quadrupole field proceeding from the low-mode approximation (Popova, 2016*a*).

It should be noted that the low-mode approximation is one of the possible means of obtaining simplified models to clarify the physics of the magnetic field generation in celestial bodies. It is assumed that the excited magnetic field of a star or a planet can be described by a comparatively small number of parameters, which enables one to substitute the dynamo equations with a suitably chosen dynamical system of equations of not-too-high an order.

Such an approach was first proposed in Ruzmaikin (1981) and further elaborated in papers Kitiashvili & Kosovichev (2008, 2009); Nefedov & Sokolov (2010); Sokoloff *et al.* (2008); Sobko *et al.* (2012); Popova (2013).

The analysis of the dynamo equations in our case showed that if the dipole field demonstrates chaotic reversals, the quadrupole field is not constant and also evolving in a certain way in time, such that the strength of the quadrupole field at the instant of the dipole field reversal is random.

The study showed that the dynamo model reproduces the reversal regime under conditions when the value of some of the governing parameters fluctuates. In this model, the governing parameters include the amplitudes of differential rotation, the alpha-effect, and meridional flows. Notice that direct measurements of these physical characteristics are difficult, and in the models mainly their distribution with depth in the liquid core is estimated.

The alpha-effect manifests itself in the degree of mirror asymmetry of the convection, i. e., in the dominance of right eddies over left ones in one hemisphere, and vice versa in the other hemisphere. This left-and-right asymmetry arises in a stratified medium due to the action of the Coriolis force. Hoyng (1993) suggested a qualitative explanation of how chirality fluctuations lead to the appearance of a long-term evolution of the geomagnetic field accompanied by numerous reversals. The results obtained in Hoyng (1993) were confirmed in study of Sobko *et al.* (2012) proceeding from the low-mode approximation.

As model of Popova (2016*b*) takes into account meridional flows — the global convective flows of matter in the liquid outer core of Earth — we have checked how such flows can affect the reversal process. The analysis revealed that in the magnetic field vascillation regime (i. e., oscillations around a nonzero time average value), a drastic decrease in the meridional circulation amplitude by about 30% leads to magnetic field reversal.

Figure 5.2a plots the theoretical dependence of Earth's dipole field amplitude $B(t)$ as a function of time t based on the solution of the dynamo equations [26] for the regime of random reversals caused by meridional flow fluctuations. The timescale in this figure spans the interval from 0 to 2 mln years. The figure shows that large fluctuations of the meridional flows leading to the reversal are rare, about once every several hundred thousand years. Figure 2b depicts the velocity $V(t)$ of the meridional flow of matter as a function of time t under the assumption that in the main part of the magnetic field generation region the meridional flows are directed oppositely to the magnetic field vector. Since in this paper we focus on the qualitative picture of magnetic field reversal mechanism, the meridional flows in Fig. 5.2 are remained in model units.

In our model, the value of the quadrupole magnetic field during the reversal of the dipole

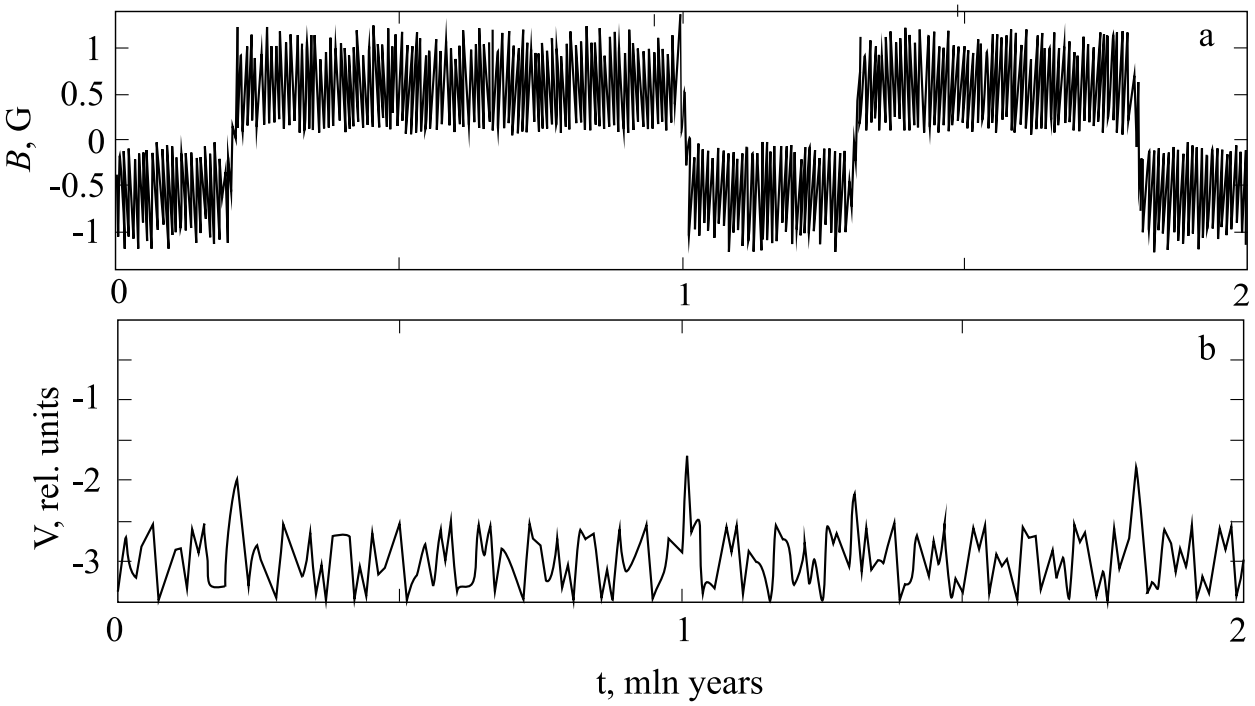

Figure 5.2: Mean dipole magnetic field strength on Earth's surface (a) and the velocity of the meridional motion of matter (b) as a function of time for the chaotic reversal regime.

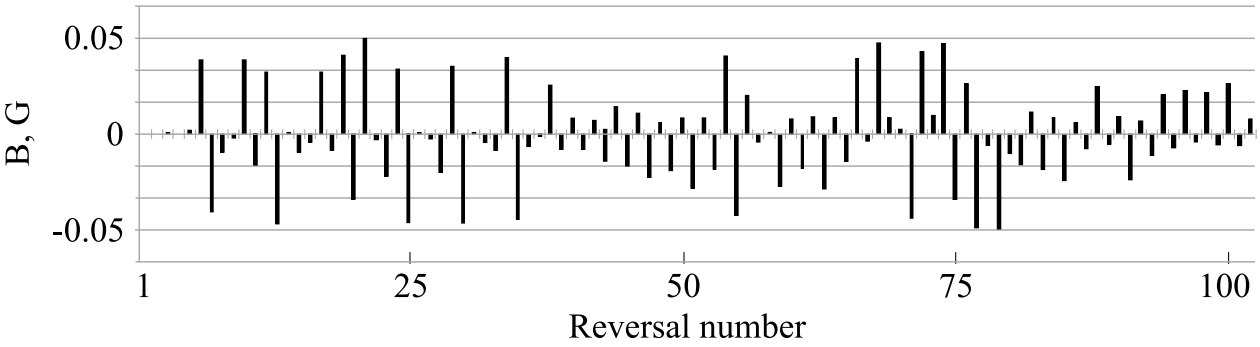

Figure 5.3: Maximum quadrupole field values on Earth's surface calculated in the geomagnetic dynamo model during 102 reversals.

field is random. Figure 5.3 demonstrates the dispersion of the maximum quadrupole field amplitudes B across Earth's surface as the dipole field crosses zero for 102 consecutive reversals. It is seen that the quadrupole geomagnetic field strength on Earth's surface does not exceed approximately 0.05 G.

5.3 Problem setup. Numerical model

Our task is to study numerically the geomagnetic field evolution, to calculate the spectral change in the SCRs/GCRs penetrating into Earth's magnetosphere until they enter the atmosphere, and to estimate the radiation hazard at the ground level. To this end, we consider a spherical model region around Earth, in which the magnetic field $\vec{B}_{Earth}$ can be represented as a superposition of two components: the dipole one and the quadrupole one, taken with different weight coefficients. A layout of the model with Earth's quadrupole magnetosphere is shown in Fig. 5.4. Calculations have been carried out in the solar-magnetospheric coordinate system, in which the X-axis points from Earth's center towards the Sun, the Y-axis is directed from the morning to the evening, and the Z-axis is coincident with the magnetic dipole axis prior to the reversal and is directed to the north.

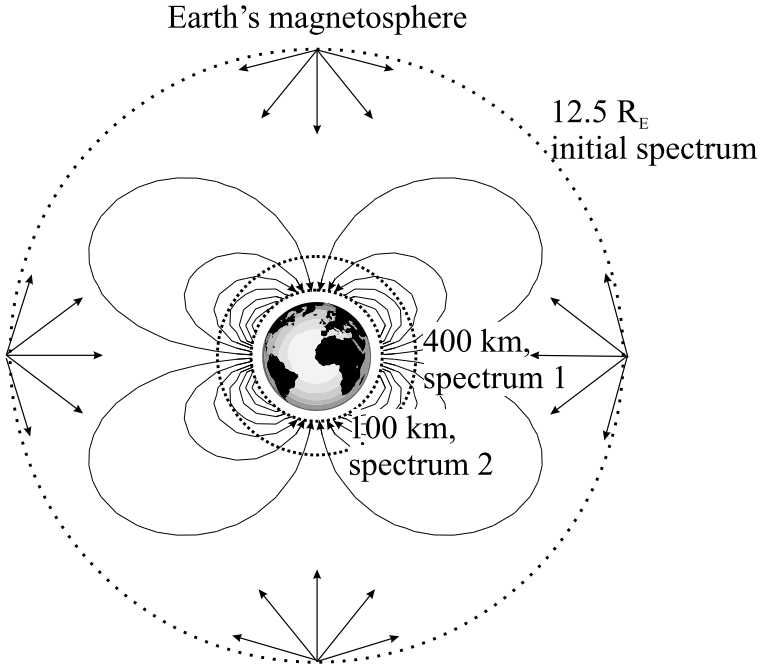

Figure 5.4: Layout of Earth's paleomagnetosphere. Shown are lines of force of the quadrupole magnetic field. The dashed curves indicate three levels at which particle energy spectra are calculated. At a distance of 12.5 R_E from Earth, the geomagnetic filed effect is small compared to the solar wind field; therefore, it is possible to set the initial GCR source on this conditional sphere with a given radius. The ISS trajectory passes at a distance of 400 km above the ground, (spectrum 1 GCR). In this region, part of the charged particle flux is cut off by Earth's magnetic field. Marked is the atmospheric boundary located 100 km above the ground (spectrum 2 GCR). The arrows show the directions of velocities of traced model particles.

An axially symmetric magnetospheric model is used, in which the ring and tail currents, as well as the effects of the radiation belts, can be ignored. The interplanetary magnetic field ($\vec{B}_{IMF}$) in this model is not taken into account ($\vec{B}_{IMF} = 0$). Model particles imitating SCR and GCR protons are ejected towards Earth from a spherical surface with a radius of 12.5 R_E centered on Earth (the approximate location of the present-day magnetopause in the

head part of the magnetosphere). The initial energy distribution from 10 MeV to 100 GeV corresponds to the GCR and SCR spectra (Nymmik, 1993). Each particle was randomly ejected inside a cone with the axis passing through the starting point and Earth's center at opening angle $\pi/2$ and was traced in the given magnetic field $\vec{B}$, constant in time, ignoring electrical fields. Therefore, the particle's velocity module is conserved ($|v| = const$), and the equation of motion of such a relativistic particle in SI units has the form

$$\begin{cases} \dfrac{d\vec{r}}{dt} = \vec{v}, \\ m\dfrac{d}{dt}\vec{v} = Ze\sqrt{1 - \dfrac{|v|^2}{c^2}}[\vec{v} \times \vec{B}]. \end{cases} \tag{5.1}$$

The motion equations are numerically integrated by the standard 4th-order Runge-Kutta method. This tracing enabled calculation of energy spectra of particles at distances of 400 km from Earth's surface, where the ISS trajectory passes, and at 100 km above the ground where the atmosphere boundary is located. The radiation hazard at ground level due to secondary particles from protons passing through the atmosphere was estimated. To validate the method, modeling in the present-day dipole field was carried out and the results were compared with radiation flux measurements performed at various altitudes in 2015.

Two reversal scenarios have been employed. The first assumed that the geomagnetic field at the reversal moment represents a superposition of the residual dipole field with a strength of 10% of the present-day value and the quadrupole field. The second one assumed Earth's magnetic field to be purely quadrupole at the reversal moment. The geomagnetic field $\vec{B}_{Earth}$ was specified using the IGRF-12 model Thébault *et al.* (2015*a*,*b*). The magnetic field potential U satisfies the Laplace equation $\Delta U = 0$, which has a solution in the form of a harmonic series:

$$U(r, \theta, \phi) = \sum_{n=0}^{\infty} \sum_{m=0}^{n} \frac{1}{r^n} \left[a_n^m \cos(m\phi) + b_n^m \sin(m\phi)\right] P_n^m(\cos\theta). \tag{5.2}$$

After normalizing the radial distance to Earth's radius R, we introduced the coefficients $g_n^m = a_n^m/R^{n+2}$ and $h_n^m = b_n^m/R^{n+2}$ to obtain

$$U(r, \theta, \phi) = R\sum_{n=1}^{\infty} \sum_{m=0}^{n} \left(\frac{R}{r}\right)^{n+1} \left[g_n^m \cos(m\phi) + h_n^m \sin(m\phi)\right] P_n^m(\cos\theta). \tag{5.3}$$

Here r, θ, ϕ are geocentric coordinates, $g_n^m(t)$ and $h_n^m(t)$ are the Gauss coefficients generally depending on time t, and P_n^m are the Legendre polynomials of the nth power and mth order normalized according to the Schmidt rule:

$$P_n^0(x) = P_{n,0}(x), \tag{5.4}$$

$$P_n^m(x) = \left(\frac{2(n-m)!}{(n+m)!}\right)^{1/2} P_{n,m}(x), \tag{5.5}$$

where

$$P_{n,m}(\cos\theta) = \sin^m\theta \frac{d^m}{d(\cos\theta)^m} P_n(\cos\theta). \tag{5.6}$$

The corresponding magnetic field components $\vec{B} = -\vec{\nabla}U$ are expressed as

$$B_r = -\frac{\partial U}{\partial r}, \quad B_\theta = -\frac{1}{r}\frac{\partial U}{\partial \theta}, \quad B_\phi = -\frac{1}{r\sin\theta}\frac{\partial U}{\partial \phi}, \tag{5.7}$$

$$B_r = \sum_{n=1}^{\infty}\sum_{m=0}^{n}\left(\frac{R}{r}\right)^{n+2}(n+1)\left[g_n^m\cos(m\phi) + h_n^m\sin(m\phi)\right]P_n^m(\cos\theta), \tag{5.8}$$

$$B_\theta = -\sum_{n=1}^{\infty}\sum_{m=0}^{n}\left(\frac{R}{r}\right)^{n+2}\left[g_n^m\cos(m\phi) + h_n^m\sin(m\phi)\right]\frac{\partial P_n^m(\cos\theta)}{\partial\theta}, \tag{5.9}$$

$$B_\phi = -\frac{1}{\sin\theta}\sum_{n=1}^{\infty}\sum_{m=0}^{n}\left(\frac{R}{r}\right)^{n+2} m\left[-g_n^m\sin(m\phi) + h_n^m\cos(m\phi)\right]P_n^m(\cos\theta). \tag{5.10}$$

As described above, we represent the geomagnetic field as a superposition of the dipole and quadrupole components:

$$\vec{B} = \vec{B}_{dip} + \vec{B}_{qp}. \tag{5.11}$$

The first three terms of the magnetic dipole $\vec{B}_{dip}$ decomposition have the form

$$B_r^{dip} = 2\left(\frac{R}{r}\right)^3\left(g_1^0\cos\theta + \left(g_1^1\cos\phi + h_1^1\sin\phi\right)\cdot\sin\theta\right), \tag{5.12}$$

$$B_\theta^{dip} = -\left(\frac{R}{r}\right)^3\left(-g_1^0\sin\theta + \left(g_1^1\cos\phi + h_1^1\sin\phi\right)\cdot\cos\theta\right), \tag{5.13}$$

$$B_\phi^{dip} = -\left(\frac{R}{r}\right)^3\left(-g_1^1\sin\phi + h_1^1\cos\phi\right). \tag{5.14}$$

The magnetic quadrupole $\vec{B}_{qp}$ can be represented as follows:

$$B_r^{qp} = 3\left(\frac{R}{r}\right)^4 \left\{ g_2^0 \frac{(3\cos^2\theta - 1)}{2} + \left(g_2^1 \cos\phi + h_2^1 \sin\phi\right) \frac{\sqrt{3}}{2} \sin 2\theta + \right. \tag{5.15}$$

$$\left. + \left(g_2^2 \cos 2\phi + h_2^2 \sin 2\phi\right) \frac{\sqrt{3}}{2} \sin^2\theta \right\}, \tag{5.16}$$

$$B_\theta^{qp} = -\left(\frac{R}{r}\right)^4 \left\{ -g_2^0 \frac{3}{2} \sin 2\theta + \left(g_2^1 \cos\phi + h_2^1 \sin\phi\right) \sqrt{3} \cos 2\theta + \right. \tag{5.17}$$

$$\left. + \left(g_2^2 \cos 2\phi + h_2^2 \sin 2\phi\right) \frac{\sqrt{3}}{2} \sin 2\theta \right\}, \tag{5.18}$$

$$B_\phi^{qp} = \sqrt{3}\left(\frac{R}{r}\right)^4 \left\{ \left(g_2^1 \sin\phi - h_2^1 \cos\phi\right) \cos\theta + \left(g_2^2 \sin 2\phi - h_2^2 \cos 2\phi\right) \sin\theta \right\}. \tag{5.19}$$

The coefficients g and h as functions of time during the period from 1900 till 2020 are known from the IGRF-12 model. Presently, the dipole coefficients g_1^0, g_1^1, h_1^1 decrease with time, and the quadrupole ones, $g_2^0, g_2^1, h_2^1, g_2^2, h_2^2$, increase. We have extrapolated the leading dipole coefficient up to the year 4500 (Fig. 5.5). The figure suggests that by the year 3580 the leading dipole coefficient will have vanished, i. e., assuming a constant dipole field decay rate, magnetic field reversal should occur.

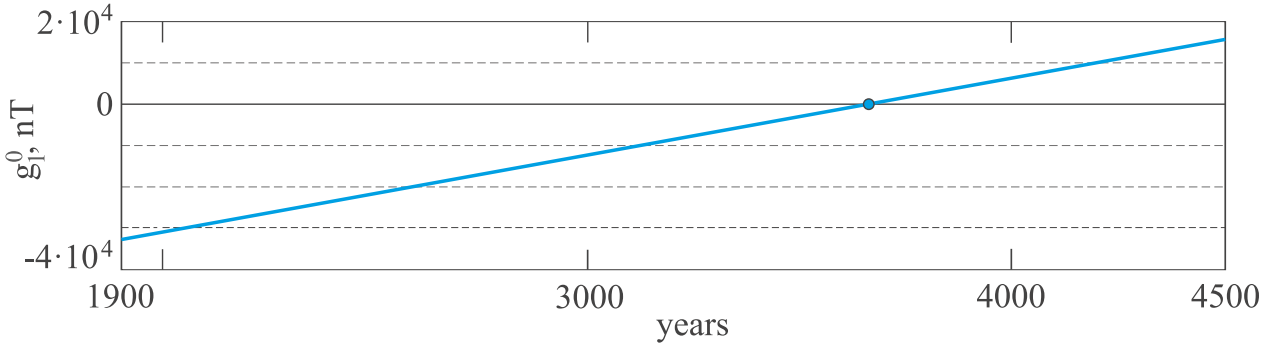

Figure 5.5: Extrapolation in time of the leading dipole coefficient g_1^0.

Figure 5.6 depicts the surface magnetic field module as a function of latitude and longitude. All fields were then computed with the Gauss coefficients obtained for the year 2015. Figure 6a plots multipole components of the geomagnetic field through the 5th order, and Fig. 5.6b shows multipoles without the dipole component. As noted above, the higher the order of the multipole component, the faster it decays with distance. Therefore, we restricted ourselves by considering a combination of the first two components: the dipole and quadrupole ones. Figure 5.6c demonstrates the field containing only the dipole and quadrupole, and Fig. 5.6d shows the quadrupole field (it is assumed that during the mag-

netic reversal expected around the year 3600 the dipole field will have fully disappeared). It can also be noted that the magnetic field strengths with multipoles up to the 5th order inclusive (Fig. 5.6a) and up to the 2nd order inclusive (Fig. 5.6c) do not differ significantly. We will also consider a superposition of the 10% dipole and quadrupole fields. Such a reversal with the incomplete disappearance of the dipole component has been assumed in Vogt *et al.* (2004); Stadelmann *et al.* (2010).

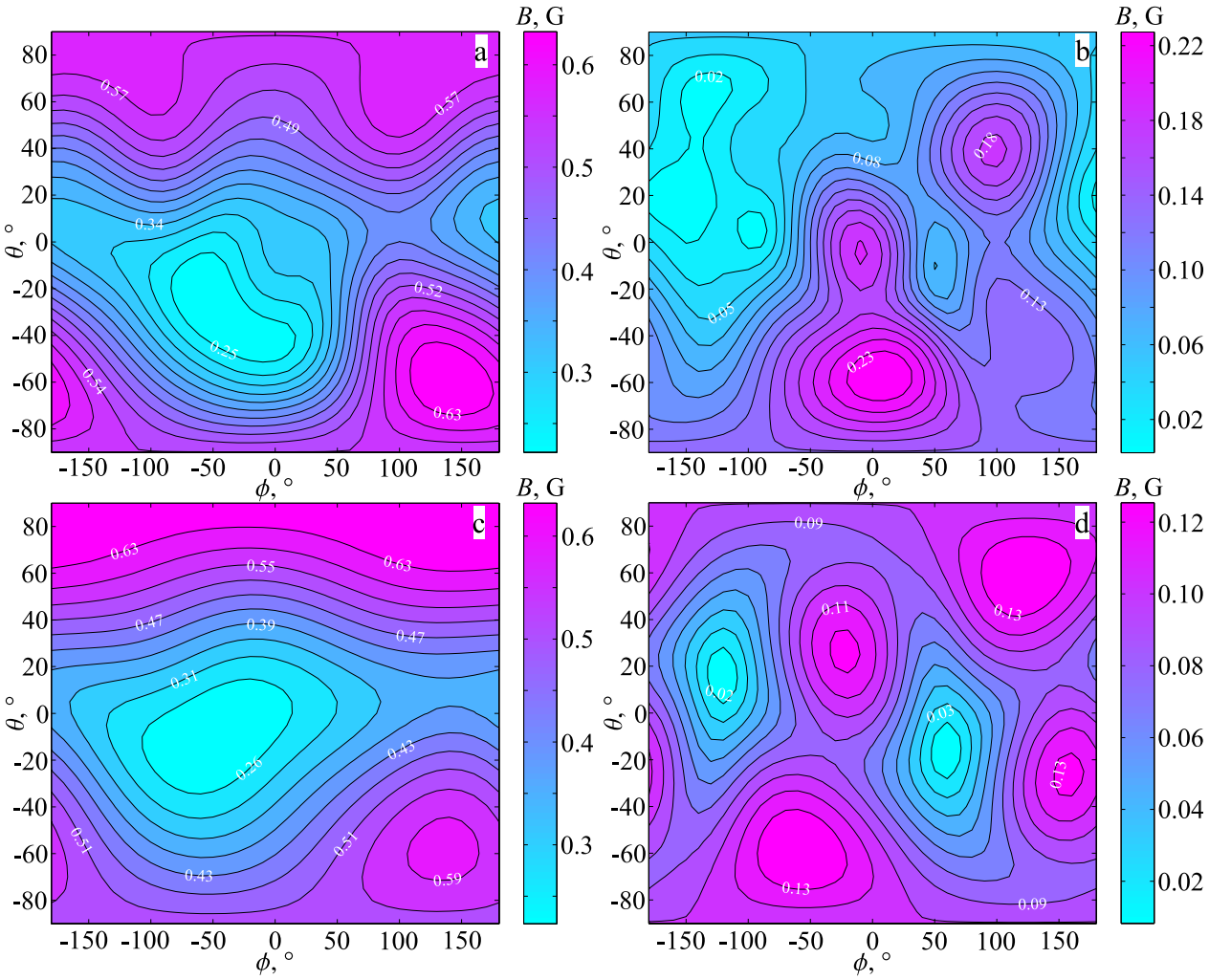

Figure 5.6: Magnetic field induction B [G] distribution across latitude θ and longitude ϕ with coefficients as of 2015: (a) the multipole magnetic field up to the 5th order inclusive; (b) the same multipoles but without the dipole component; (c) superposition of the dipole and quadrupole; (d) quadrupole.

5.4 Radiation in the near-Earth space and on the ground

As the GCR particle energies are on average a few orders of magnitude higher than those of SCRs and most of them (92%) are protons, we will assume that the radiation environment near Earth is mainly determined by GCR protons and EAS particles produced by the interaction of GCR protons with the atmosphere. Figure 5.7 presents the model logarithmic spectra of the GCR particles (protons p^+, electrons e^-, helium ions $^4_2He^+$, and oxygen ions $^{16}_8O^+$) outside Earth's magnetosphere. It is seen that the flux density of GCR protons with energies above 30 MeV significantly exceeds those of other GCR particles. Therefore, we have ignored in the present work contributions from GCR electrons and heavy ions to the radiation environment on Earth. It is also known (Antonov, 2007) that protons with energies below the pion creation threshold ($\sim$ 300 MeV) lose energy in atmospheric interactions for ionization and excitation of atomic nuclei in the air. With decreasing energy, the effective cross section of proton ionization losses increases. As a result, all low-energy protons are rapidly decelerated and absorbed. Thus, to estimate the radiation dose on Earth's surface, only GCR protons with energies above 300 MeV will be considered.

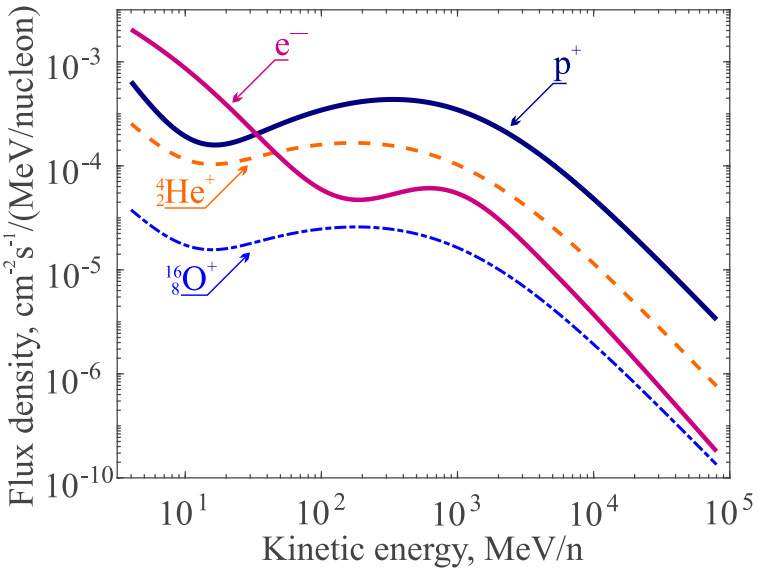

Figure 5.7: Mean differential spectra of GCR particles: protons (p^+), electrons (e^-), helium ions ($^4_2He^+$) and oxygen ions ($^{16}_8O^+$) at a distance of 12.5 R_E outside the magnetosphere.

The radiation situation in the ISS orbit is somewhat different: it requires taking into account the effect of GCR and SCR protons. The electron flux density has been ignored again, because electrons are much less dangerous than protons due to different mechanisms of their impact on humans (Antonov, 2007).

To verify the model particle energy spectra, a comparison of the calculated and observed spectra in the present-day magnetic field (2015) was performed, in particular, with measurements carried out at the ISS (2015). The differential GCR proton spectrum was calculated

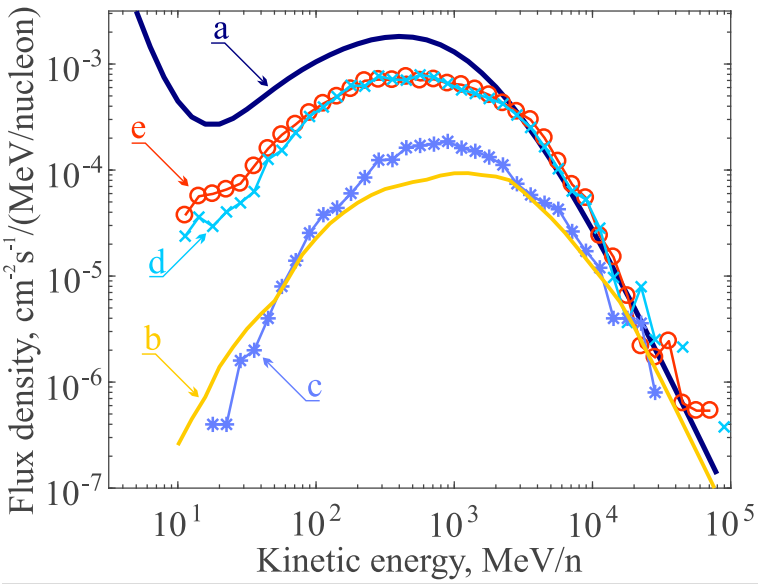

Figure 5.8: Experimental mean differential spectra of GCR protons at the solar activity minimum: in Earth's orbit outside the magnetosphere (curve a), in the ISS orbit at latitude $\theta = 51.6°$ (curve b reflects observational data), and the spectra calculated at the altitude of 400 km and latitudes $\theta = 50° - 55°$ for the present-day field configuration (curve c) and at the reversal moment: 10% dipole + present quadrupole (curve d) and pure quadrupole (curve e).

at different distances from the Earth using the model with the corresponding source spectra on the 12.5 R_E sphere. The calculated spectrum was compared at the altitude of 400 km and latitudes $50° - 55°$ with the ISS data obtained at the 400 km altitude and $\theta = 51.6°$ latitude. The obtained spectrum is presented in Fig. 5.8. The figure demonstrates that the calculated spectrum (curves c) corresponding to present-day conditions is in a rather good agreement with the ISS data (curves b), i. e., the simulated geomagnetic cutoff of primary cosmic-ray (GCR and SCR) corresponds to the observed energy spectrum. Thus, we can conclude that the model quite adequately calculates the high-energy particle fluxes penetrating into Earth's magnetosphere from interplanetary space.

Figure 5.9 displays regions available for GCR protons at an altitude of 100 km above sea level before field reversal (Fig. 5.9a) and during the reversal: the reversal scenario shown in Fig. 5.9b includes 10% of the dipole field and the quadrupole field at the present value, while in Fig. 5.9c only the quadrupole field is present. The primary cosmic rays freely reach the planet's atmosphere in irradiated zones, i.e., in a closed magnetosphere model (that is, field lines are not allowed to pass through the magnetopause), their energy spectra don't change in these areas.

Clearly, the disappearance of the dipole component should change not only the 'geography' of particle precipitation but also the number of particles. The increase in the number of protons and their precipitation zone area at the moment of field reversal suggests a worsening of the radiological hazard in the circumterrestrial space. In Fig. 5.9c (pure quadrupole), one can also see the penetration of particles into the South Atlantic Anomaly (SAA) region — the region with the weakest modern geomagnetic field, less than 0.32 G at sea level. The

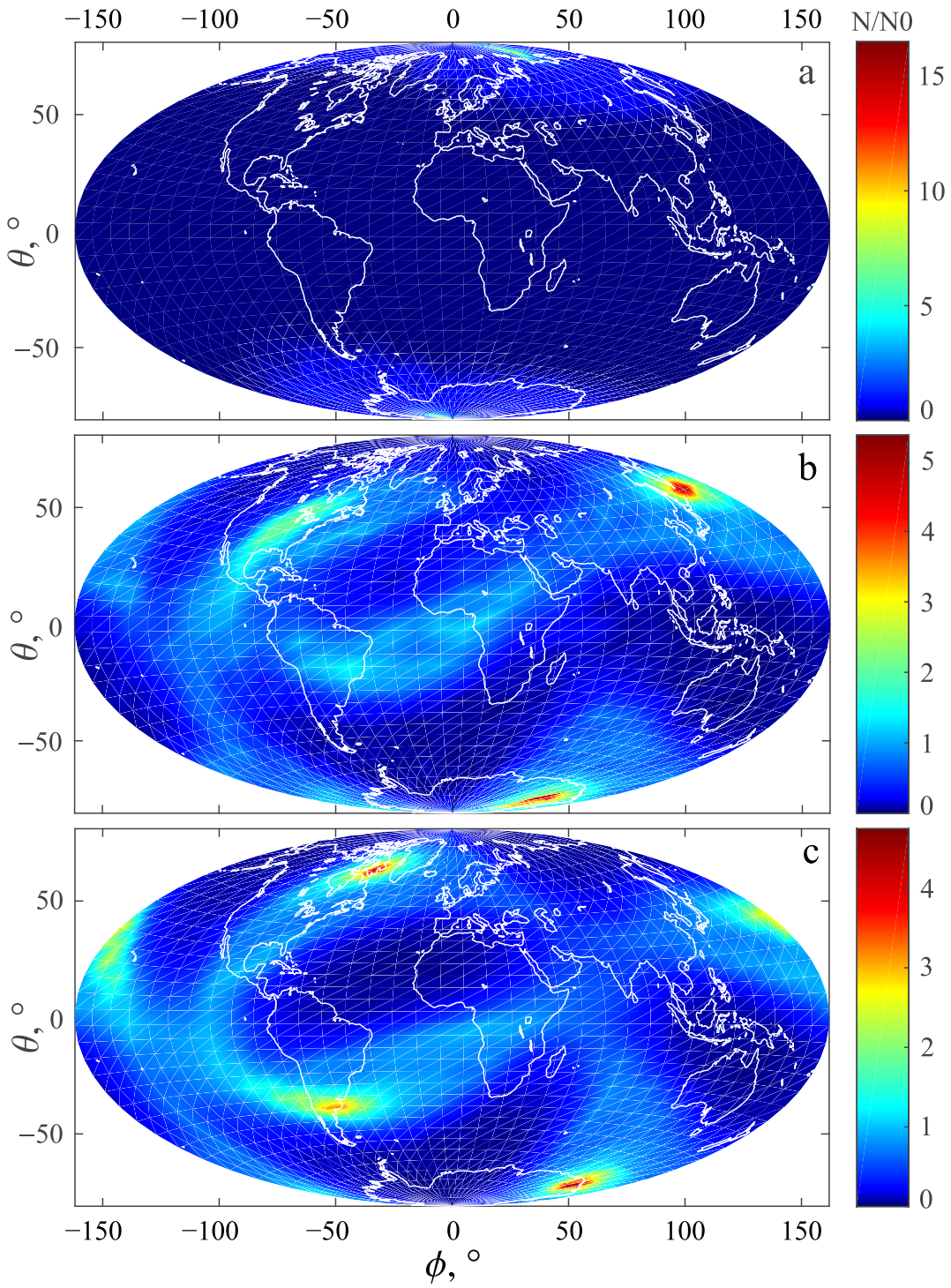

Figure 5.9: N is the total number of GCR protons hitting Earth's atmosphere boundary (100 km) for a given magnetic field configuration: (a) in 2015 ($\sum N/\sum N0 = 0.16$); in the reversal scenarios with (b) 10% dipole and quadrupole field ($\sum N/\sum N0 = 0.43$); (c) in the pure quadrupole field at the present value ($\sum N/\sum N0 = 0.49$); $N0$ is the number of protons reaching the unmagnetized Earth.

SAA is located in the latitude interval from $-50°$ to $0°$, and at longitudes from $-90°$ to $+40°$ (Fig. 5.6a). However, at the reversal moment, the magnetic field topology would be such that the SAA would have a higher magnetic field strength (Fig. 5.6b), and the particles will precipitate this region.

In passing through the atmosphere, the number of 'primary' protons decreases due to nuclear interactions and ionization losses, but interactions of the high-energy 'primary' protons with nuclei generate a certain number of 'secondary' protons, because a destroyed nucleus decays into protons and neutrons with lower energies (Galper, 2002; Kalmykov & Kulikov, 2007). The results reported in Sato *et al.* (2008); Sato (2015) suggest that positive and negative muons, as well as neutrons generated by nuclear interactions, mostly contribute to the radiation exposure dose. Below, we provide estimates of the radiation situation on Earth due to secondary particles, which are virtually independent of the magnetic field strength.

Figures 5.10 and 5.11 illustrate the mean energy spectra of GCR and SCR protons at the entrance to Earth's magnetosphere and upon entering the atmosphere: at a distance of 12.5 R_E from Earth's center (curve a), at a distance of 100 km from the ground in the year 2015 (curve d), and for two possible field configurations at the moment of magnetic reversal (curves b, c correspond to scenarios shown in Figs 5.9b, c, respectively). The mean energy spectra of these two reversals were found to be identical, although the particle spatial precipitation regions (Figs 5.9b, c) are different.

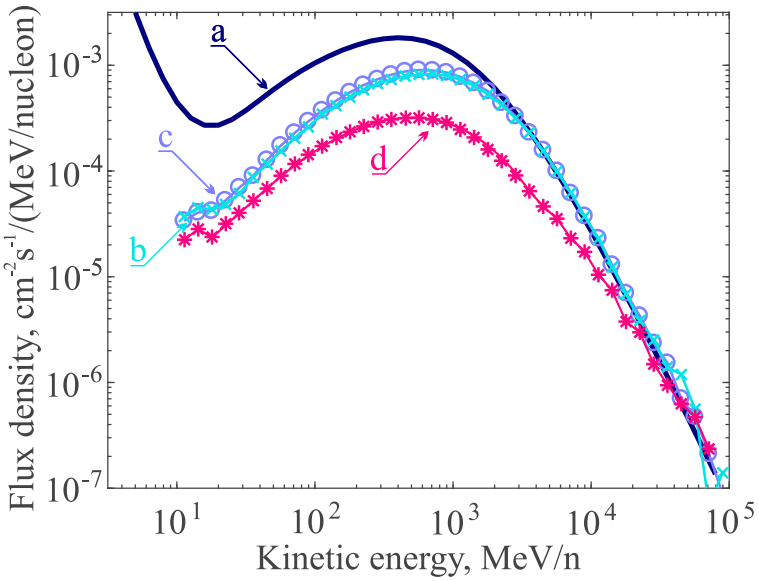

Figure 5.10: Mean differential spectra of GCR protons at the solar activity minimum at a distance of 12.5 R_E from Earth's center outside the magnetosphere (curve a), at a distance of 100 km above the ground level for the geomagnetic reversals (curves b, c correspond to scenarios presented in Figs 5.9b, c, respectively), and in 2015 (curve d).

A comparison with Fig. 5.9a shows that in the near-Earth space (100–400 km) with an account for the low-energy spectrum (below 100 MeV) the mean radiation background turns out to be higher in the present-day magnetic field than during the reversal due to the

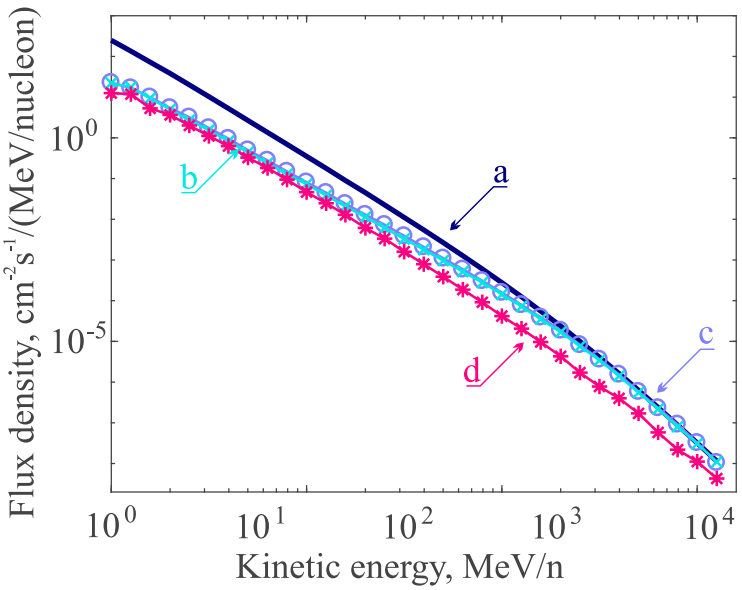

Figure 5.11: Mean differential spectra of SCR protons at the solar activity maximum at a distance of 12.5 R_E from Earth's center outside the magnetosphere (curve a), at a distance of 100 km above ground level for the geomagnetic reversals (curves b, c), and in 2015 (curve d).

presence of high-latitude zones with enhanced radiation exposure. At the same time, at the ISS latitude of 400 km, the proton flux density at the reversal moment should still be higher than in 2015 (see Fig 5.8).

Let us assess the biological impact of GCR protons. To do this, let us represent the formula for the effective radiation dose power (behind a layer with shielding thickness δ) in the form

$$H_R = B \int \Phi(E) \cdot Q(E) \frac{dE}{\rho dx} dE', \tag{5.20}$$

where B is the transition coefficient from the absorbed energy to the dose, Sv·MeV^{-1}cm^2; $Q(E)$ is the quality coefficient of the ionizing radiation (GOST 8.496-83 GSI), $dE/\rho dx$ is an ionization losses in the shield material described by the known formula (Antonov, 2007), MeV·g^{-1}cm^2; $\Phi(E)$ is the differential energy spectrum, E' is an energy at the depth of shield δ, related to energy E, MeV, falling on shield. Ionization losses and mean free paths of protons and electrons for various materials can be found in (Bespalov, 2006). We are protected by an air layer (atmosphere) with a thickness of about 1 kg/cm^2, which is equivalent to about 130 cm of iron.

The differential spectra used in the calculations are represented in Figs 5.8, 5.10 and 5.11. Here, in Figs 5.8 and 5.10 are shown GCR proton spectra during the solar activity (SA) minimum at altitudes of 400 km (in the ISS orbit) and at 100 km above the ground level, and in Fig 5.11 is presented SCR proton spectrum at the SA maximum. These spectra are chosen such because the maximum radiation doses on the ground level are found during

the SA minima due to GCR particles, and in the ISS orbit due to SCR particles during SA maxima.

In the ISS orbit, SCR protons mainly contribute to the radiation dose during the SA maximum (86% of the total radiation dose power from GCRs and SCRs for the modern field, and 97% for the pure quadrupole field). Table 5.1 suggests that during the reversal the total radiation dose power is 23.2 mSv day^{-1}(or 8500 mSv yr^{-1}). According to Table 5.5, these doses accumulated in one year would exceed the permissible radiation limit of 200 mSv, which can significantly restrict the duration of stay of astronauts in orbit, even with account for shielding. Figure 5.12 shows the radiation dose power decrease with aluminum (with density of 2.7 g/cm^3) shielding thickness (from the space suit to the ISS outer sheet). Aluminum shield corresponding to 1 cm thickness reduces the dose by two orders of magnitude. The power of the effective radiation dose from protons is calculated by Eq. 5.20.

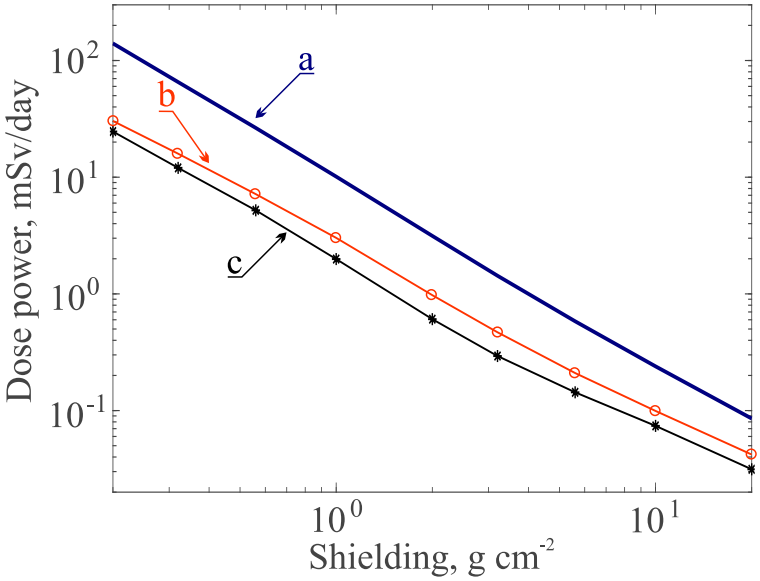

Figure 5.12: Average power of an equivalent radiation dose under different shieldings at the SA maximum in the ISS orbit caused by radiation belt, SCR, and GCR particles (curve c), and due to SCRs and GCRs without the magnetosphere (curve a), and in a quadrupole field (curve b).

The calculated effective radiation doses caused by GCR and SCR protons are listed in Tables tables 5.1 to 5.5, according to which, the GCR and SCR proton flux densities are higher for the pure quadrupole field than for a superposition of 10% of the dipole and quadrupole fields; therefore, below we will assume a pure quadrupole field during the magnetic field reversal.

The radiation background in the ISS during the SA minimum is quite different. The SCR proton spectra at the SA minimum are one and a half orders of magnitude below those at the SA maximum plotted in Fig. 5.8 The calculations showed (see Table 5.2) that at the reversal moment, the total radiation dose power would be 2 mSv day^{-1} (or 730 mSv yr^{-1}).

Table 5.3 presents calculations of radiation dose powers averaged over the planet surface

Table 5.1: Radiation dose power [mSv day^{-1}] in the ISS orbit for three magnetic field configurations (with the quadrupole at the present value) and without a magnetic field at the solar activity maximum.

	2015 field	10% dipole + quadrupole	0% dipole + quadrupole	Without magnetic field
GCR	0.23	0.77	0.87	1.08
SCR	1.45	15.56	22.28	113.7
GCR + SCR	1.68	16.33	23.15	114.8

Table 5.2: Radiation dose power [mSv day^{-1}] in the ISS orbit for three magnetic field configurations (with the quadrupole at the present value) and without a magnetic field at the solar activity minimum.

	2015 field	10% dipole + quadrupole	0% dipole + quadrupole	Without magnetic field
GCR	0.37	1.3	1.4	2
SCR	0.04	0.42	0.62	3.26
GCR + SCR	0.41	1.72	2	5.26

Table 5.3: Radiation dose power [mSv day^{-1}] from protons with energies of > 300 MeV at an altitude of 100 km from the ground for three magnetic field configurations (with the quadrupole at the present value) and without a magnetic field during the solar activity maximum.

	2015 field	10% dipole + quadrupole	0% dipole + quadrupole	Without magnetic field
GCR	0.27	0.68	0.73	0.97
SCR	0.31	0.6	0.67	1.9
GCR + SCR	0.58	1.28	1.4	3.9

Table 5.4: Radiation dose power [mSv day^{-1}] from protons with energies of $>$ 300 MeV at an altitude of 100 km from the ground for three magnetic field configurations (with the quadrupole at the present value) and without a magnetic field during the solar activity minimum.

	2015 field	10% dipole + quadrupole	0% dipole + quadrupole	Without magnetic field
GCR	0.46	1.25	1.31	1.87
SCR	0.006	0.011	0.012	0.035
GCR + SCR	0.47	1.26	1.32	1.91

from GCR and SCR protons with energies above 300 MeV at an altitude of 100 km in case of maximum solar activity. At this altitude, GCR and SCR particles almost equally contribute to the radiation background for both the modern magnetic field and the field during magnetic reversal. However, the radiation situation on Earth's surface is mainly determined by high-energy GCR protons, whose dose at the altitude of 100 km, as seen from Tables 5.3 and 5.4, during the SA maximum is two times as low as during the minimum. Correspondingly, the same ratio of radiation doses can be expected on the ground.

Table 5.4 presents the radiation power doses for GCR and SCR protons with energies above 300 MeV at the altitude of 100 km during the SA minimum. As expected, the SCR particles do not significantly contribute in this case to the total radiation background.

To estimate the radiation dose power on the ground level, we calculate the radiation dose ratio at the altitude of 100 km for the reversal (H_{R3}=1.32 mSv day^{-1}) and modern (2015) (H_{R2}= 0.47 mSv day^{-1}) fields: $H_{R3}/H_{R2} \approx 3$. By assuming that Earth's magnetic field is zero (H_{R1}=1.9 mSv day^{-1}), the corresponding radiation dose power ratio would be $H_{R1}/H_{R2} \approx 4$. By approximately setting constant atmospheric properties, we can assume that the obtained coefficient will be conserved on Earth's surface at the reversal time, too.

According to the PARMA model (PHITS-based Analytical Radiation Model in the Atmosphere; PHITS — Particle and Heavy Ion Transport code System), to estimate cosmic ray fluxes (Sato, 2015), in 2015 at the solar activity minimum the human radiation exposure at sea level due to cosmic rays was about 8×10^{-4} mSv day^{-1}, or 0.3 mSv yr^{-1}. From Table 5.6 showing the impact of the yearly radiation dose on humans, it is possible to conclude that a three- or even a four-fold increase in this dose will not be dangerous for humans over the natural duration of the human life (100 years). For completeness, the assumed radiation dose powers on Earth's surface at the SA minimum are taken into account in Table 5.5.

Table 5.5: Corrected radiation dose power [mSv yr^{-1}] on Earth's surface for three magnetic field configurations (with the quadrupole at the present value) and without a magnetic field (during the solar activity minimum).

2015 field	10% dipole + quadrupole	0% dipole + quadrupole	Without magnetic field
0.3	0.8	0.85	1.2

Table 5.6: Impact of γ-radiation dose on humans.

Dose, mSv	Impact on humans
0-200	No visible damage
200-500	Possible changes in blood composition
500-1000	Change in blood composition, damage
1000-2000	Damage, possible incapacitation
2000-4000	Total disability, possible fatality
4000	50% mortality
6000	Lethal

5.5 Conclusion

The geomagnetic field reversal process, which has likely started at present, can affect the structure of Earth's magnetosphere, the radiation situation (Siscoe & Chen, 1975; Saito *et al.*, 1978), and life on Earth in general (Glassmeier *et al.*, 2009*b*; Glassmeier & Vogt, 2010; Glassmeier *et al.*, 2004; Uffen, 1963; Sagan, 1965). During the reversal, in addition to the dipole component reversal, a shift of the quadrupole component is possible. In this case, the magnetic anomalies will change location, which also contributes to the cosmic radiation redistribution on Earth.

The impact of reversals on the biosphere and on humans, in particular, can be significant, although it is quite possible that such changes appear on paleomagnetic timescales and not during the lifetime of an individual or even the span of several generations.

Unlike low-energy SCRs and GCRs, during the geomagnetic dipole field disappearance, high-energy cosmic ray fluxes will be much higher inside Earth's magnetosphere and will provide larger radiation exposures to the ground. A long-term period of increased radiation lasting one thousand years or even more could be dangerous for humankind, its technological environment, and near-Earth space expeditions. The question is: can humankind survive in

the periods of increased radiation fluxes during magnetic reversals?

To elucidate this issue, we have carried out numerical simulations to estimate radiation threats for humans from GCR and SCR fluxes on the ground and at the ISS altitude of 400 km during an reversal period, when, according to the hypothesis, the dipole component of the geomagnetic field should totally or partially disappear. The model results and their analysis suggest that for the ISS orbiting at 400 km SCR particles, whose flux should increase by a factor of 14 over the present-day value, are the most dangerous.

Thus, radiation exposure to astronauts could be as high as 6000 mSv yr^{-1} or 8500 mSv yr^{-1} (without shielding) at the SA maximum. Most of the low-energy solar wind particles will be absorbed by the atmosphere and will not reach Earth's surface. At the same time, the radiation at the ground level should increase due to secondary GCRs (muons) and photon radiation, to which the atmosphere is transparent.

By assuming constant atmospheric properties by the beginning of reversal epoch, it is possible to predict a three-fold radiation increase at the solar activity minimum and a two-fold increase at the solar activity maximum. However, taking into account the present SA minimum radiation level at sea level of 8.02×10^{-4} mSv day^{-1}, a three-fold increase in the radiation background should not be dangerous for humans. Nevertheless, there is no certainty that on the full reversal timescale of 5–10 thousand years the elevated radiation background is totally safe for humans and organic life on Earth. It cannot be ruled out that the accumulation of genetic mutations (Harrison, 1966; Zarrouk & Bennaceur, 2009; Ponert & Príhoda, 2009) could have remote effects and appear on a longer timescale on the order of the reversal duration or longer.

To conclude, we can say that the results of our calculations, on the one hand, disprove studies arguing a significant heightened radiation impact on all living organisms on Earth at the period of magnetic field reversal: no critical radiation background rise has been found. At the same time, our results have a preventive character suggesting a radiation danger for humans in space (for example, in orbital stations at certain latitudes of $< 60°$) during magnetic reversal periods.

Chapter 6

Generalization of Störmer theory

What happens to radiation belts during geomagnetic reversal? To answer this question we have generalized Störmer theory for an axisymmetric superposition of dipole and quadrupole fields.

The possibility of trapping of charged particles in a magnetic dipole field was predicted several decades before "in-situ" measurements at the Earth orbiting satellites (1957) in studies of Störmer (1907, 1930, 1955) aimed at the mathematical justification of the Goldstein & Birkeland conjecture on the corpuscular nature of aurora, and in the works of Lemaître & Vallarta (1933); Vallarta (1938), devoted to the construction of an allowed cone of cosmic rays. These studies became the basis of the classical theory that researches the motion of charged particles coming from the large distances to the magnetic field. The theory has become widespread, and its consequence, the capture of particles by magnetic traps, was proved experimentally by the discovery of the radiation belts of the Earth, Jupiter and Saturn. The Voyager 2 program only formally confirmed the existence of Van Allen belts around Uranus and Neptune. In particular, a lot of information about the structure and dynamics of internal (Van Allen *et al.*, 1959) and external (Vernov *et al.*, 1958; Lemaire & Gringauz, 1998) radiation belts have been collected in near-Earth space, and their physics was thoroughly reviewed by Schindler (1975).

The Störmer's theory describes all the qualitative phenomena associated with the particles' motion in a dipole magnetic field (Störmer, 1955; Longair, 1981; Smart *et al.*, 2000). It also obtained a generalization for a configuration with a quadrupole field (Urban, 1966). Shebalin (2004) addressed charged particle motion in general axisymmetric multipole of degree n (up to $n = 5$). In the particular case of dipole and quadrupole fields, our and Shebalin's results can be compared. Particle motion in a superposition field with a magnetic dipole moment collinear and anti-collinear to an external uniform magnetic field was considered in

papers of Katsiaris & Psillakis (1986); Lemaire (2003).

In recent years, the superposition of dipole and quadrupole fields as a possible scenario of geomagnetic reversal has become of particular interest (Glassmeier & Vogt, 2010). As is widely known, the total magnetic field energy doesn't vary much during a reversal therefore the dipole magnetic field energy may be distributed randomly among the higher multipole moments (Schulz & Paulikas, 1990). We assume as in the previous chapter that the dipole component of the field vanishes with time, so that the quadrupole moment becomes dominant. Since the quadrupole field also evolves in time, its magnitude and configuration at the reversal time, generally speaking, may be random. All possible configurations of the quadrupole field can be found in paper (Vogt & Glassmeier, 2000). We are interested in an axisymmetric quadrupole. There are some precedents for treating the transition field as axisymmetric, e.g., Williams & Fuller (1981) suggest that some combination of the low order zonal harmonics may be typical of each reversal, Willis & Young (1987) dealt with an individual non-dipolar terms as predominant ones during polarity reversals, several possible combinations of dipole and quadrupole paleomagnetic fields (including axisymmetric ones) were considered by Vogt *et al.* (2004, 2007); Stadelmann *et al.* (2010). Particle impact regions and cutoff latitudes against kinetic energy were also illustrated. However, in the framework of analytical analysis, the problem with the superposition of axisymmetric dipole and quadrupole fields has not been considered so far.

Although the geomagnetic dipole moment is much smaller during a geomagnetic reversal than at present, there is no requirement for the dipole moment to pass through zero in the reversal process. For instance, the dipole moment during the reversal simulated by Glatzmaier & Roberts (1995); Glatzmaier (2002) had attained a minimum value of about 10% of its present one. From analogy with directly observed polarity transitions of the Sun's magnetic field during solar maxima, Saito & Akasofu (1987) had anticipated, that the magnetic axis could rotate through 180° relative to its present direction, passing through 90° near the time of the dipole moments minimum (but non-zero) value. This geomagnetic reversal was also modeled by Sheyko *et al.* (2016). The present study would be equally applicable to such a situation. By using the example of the dynamo model of Sheyko, we observe how the geomagnetic field at some reversal moments can assume a quasi-axisymmetric configuration.

6.1 Magnetic field model

The purpose of this paper is to study the motion of relativistic particles in the azimuthally symmetric magnetic field (of order $m = 0$) consisting of the superposition of the dipole and

quadrupole components in the geocentric coordinate system (r, θ, ϕ):

$$\mathbf{B} = \mathbf{B}_{dip} + \mathbf{B}_{qp} = \\ = g_1^0 \left(\frac{R_E}{r}\right)^3 [2\cos\theta\ \mathbf{e}_r + \sin\theta\ \mathbf{e}_\theta] + g_2^0 \frac{3}{2} \left(\frac{R_E}{r}\right)^4 \left[\left(3\cos^2\theta - 1\right)\ \mathbf{e}_r + \sin 2\theta\ \mathbf{e}_\theta\right], \quad (6.1)$$

where g_1^0 and g_2^0 are the leading dipole and quadrupole Gaussian coefficients of the IGRF (Thebault *et al.*, 2015), generally speaking, slowly varying with time t, for the modern magnetic field $g_1^0 = -0.3$ G and $g_2^0 = -0.025$ G.

Note that charged-particle motion would be the same even if r in Eq. (6.1) were measured from an effective magnetic center offset from Earth's geographic center and if θ were measured from a magnetic symmetry axis passing through $r = 0$ but inclined relative to Earths rotation axis.

The $m = 0$ and $m = 1$ components of the quadrupole moment can be reduced to zero by transforming the IGRF to appropriate offset tilted dipole coordinates. However, this could not have been done here because displacement of the magnetic center generates an infinite series of higher multipoles (Hilton & Schulz, 1973). The infinite series would not even converge if the dipole moment were too small compared to the original quadrupole moment in geocentric coordinates (placing the effective magnetic center outside the Earth during the reversal itself). Thus the present two-term model is simpler than the offset-dipole alternative.

We limit ourselves here to the dipole ($n = 1$) and quadrupole ($n = 2$) terms for simplicity. This model seems to capture essential elements of the **B** field now and during a geomagnetic reversal. Higher multipoles ($n > 2$), whose contributions to **B** decrease as $(1/r)^{n+2}$ and thus more strongly with altitude, could possibly be added as a future refinement but are not part of the present study. Calculation of the maximum values of the quadrupole field in the geomagnetic dynamo model (Popova, 2016*b*) showed that its intensity at the Earth's surface does not exceed 0.05 G. For the clear representation of our results we assume that $g_2^0 = -0.025$ G is constant in time, i.e. the present-day quadrupole field strength will not change. Thus, the contribution of the dipole component of the magnetic field decreasing during the magnetic reversal is characterized by the $\kappa_g = g_1^0/g_2^0$ parameter values from 12 to 0, where 12 corresponds to the modern dipole field of the Earth.

The magnitude of the modern dipole Earth's field prevails over the quadrupole and is almost symmetric (quasisymmetric) with respect to the Earth's rotation axis. The quadrupole field configuration is not axially symmetric today, and in the reversal process it can be of

a random nature. The above Störmer theory is based on axial symmetry and stationarity of the field. To construct our model, we make the analogous assumption that the dipole and quadrupole magnetic fields of the planet are axisymmetric, i. e. with magnetic moments collinear to the axis of rotation. In this chapter we consider the extremely simplified scenario of magnetic reversal, in reality it can be more complicated, therefore the realistic configuration of the radiation belts can differ from the solutions presented in this paper. However, our work can be useful to study some general trend or general pattern of the Earth's magnetosphere evolution in the period of possible magnetic reversal.

The square of magnetic field strength B^2 as a function of the geo-latitude $\lambda = \pi/2 - \theta$ (Fig. 6.1) has the form

$$B^2 = B_{dip}^2 + 2\left(\mathbf{B}_{dip} \cdot \mathbf{B}_{qp}\right) + B_{qp}^2 = \\ = (g_1^0)^2 \left(\frac{R_E}{r}\right)^6 \left[4\sin^2\lambda + \cos^2\lambda\right] + 12 g_1^0 g_2^0 \left(\frac{R_E}{r}\right)^7 \sin^3\lambda + \\ + (g_2^0)^2 \frac{9}{4} \left(\frac{R_E}{r}\right)^8 \left[4\sin^4\lambda + \cos^4\lambda\right]. \quad (6.2)$$

The magnetic field $\mathbf{B}$ is derivable from a vector potential $\mathbf{A} = \alpha\vec{\nabla}\beta$ such that $\mathbf{B} = \left[\vec{\nabla} \times \mathbf{A}\right] = \mathbf{B} = \left[\vec{\nabla}\alpha \times \vec{\nabla}\beta\right]$, where $\vec{\nabla}\beta = \mathbf{e}_\phi/(r\cos\lambda)$ and

$$\alpha(r,\lambda) = -R_E^2 \left[g_1^0 \left(\frac{R_E}{r}\right) + g_2^0 \frac{3}{2} \left(\frac{R_E}{r}\right)^2 \sin\lambda\right] \cos^2\lambda, \quad (6.3)$$

α and β are Euler potentials (Willis & Young, 1987; Jacobs, 1994). Field lines of the magnetic field $\mathbf{B}$ are defined by Eq. (6.3). Figure 6.1 shows the magnetic force lines at the time-epoch of interest: the predominance of the dipole component with the ratio $g_1^0/g_2^0 = 12$, the superposition of the dipole and quadrupole with g_1^0/g_2^0 =1.2, 0.6, 0.3, 0.12 and the pure quadrupole field ($g_1^0/g_2^0 = 0$). The magnetic field lines of the Earth's dipole field are directed from the south pole to the north pole. The force lines of the quadrupole field are directed from the equator to the poles. Thus, the directions of the force lines of the dipole and quadrupole in the northern region are the same, in the southern region they are opposite, so when the fields are superposed the length of the force lines increases in the northern region and decreases in the southern region.

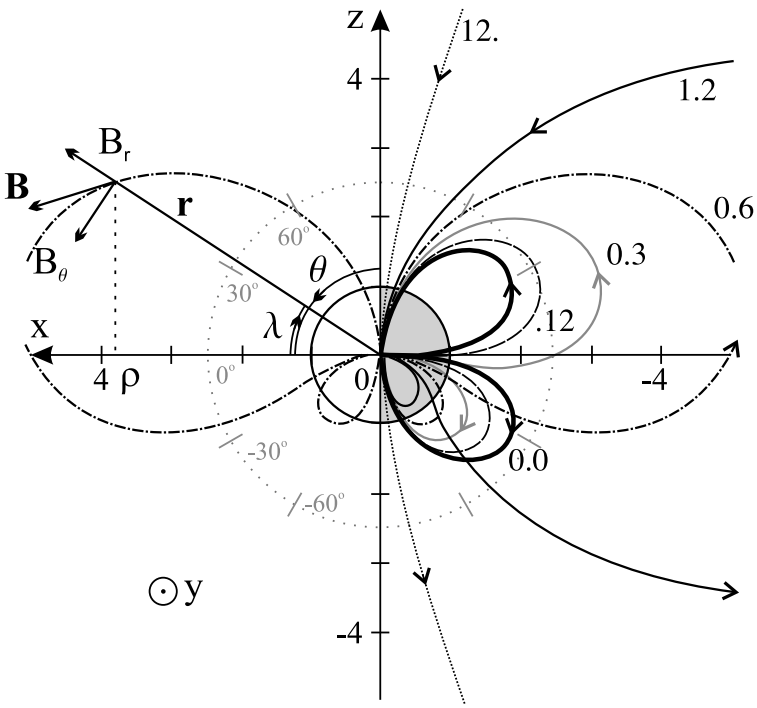

Figure 6.1: Lines of constant α (which also are field lines) of the axisymmetric dipoles and quadrupoles superpositions with given values of weighting coefficients $\kappa_g = g_1^0/g_2^0 =$ 12, 1.2, 0.6, 0.3, 0.12, 0.0 in the coordinate system of the medial plane. For all depicted field lines the value of α equals $g_1^0 R_E^3/L$, where $L = 100\ R_E$ is the magnetic shell in a dipole field.

The azimuthal potential is expressed as

$$A_\phi = -R_E \left[g_1^0 \left(\frac{R_E}{r} \right)^2 \cos\lambda + g_2^0 \frac{3}{2} \left(\frac{R_E}{r} \right)^3 \cos\lambda \sin\lambda \right], \tag{6.4}$$

Between the northern and southern lobes of the magnetic field, there is a separatrix that provides another path for the enhanced charged particle to access the Earth's surface. This separatrix should emanate from a magnetic null point ($\mathbf{B} = 0$) on the symmetry axis ($\cos\lambda = 0$), leaving its direction ambiguous. Eq. (6.1) yields such a magnetic null point on the $\cos\lambda = 0$ symmetry axis at

$$\kappa_g \left(r/R_E \right) = -3/2 \operatorname{sgn}(\sin\lambda), \tag{6.5}$$

where $\kappa_g = g_1^0/g_2^0$ is the weighting coefficient characterizing the contribution of the dipole and quadrupole components in the expression for magnetic field $\mathbf{B}$, and $\sin\lambda = \pm 1$. Since r/R_E is inherently positive, the value of $\sin\lambda$ at the magnetic null point must be opposite in sign to κ_g. (For example, the positive value of $\kappa_g > 0$ corresponds to the modern magnetic field. If the roles of the northern and southern hemispheres are reversed, the value of $\kappa_g < 0$ is negative.) The null point lies inside the Earth for $\kappa_g > 3/2$, and the magnetic poles on the symmetry axis at $r = R_E$ would thus have opposite signs (as for a dipole field). The null point lies outside the Earth for $\kappa_g < 3/2$, and the magnetic poles on the symmetry axis at

$r = R_E$ would thus have the same sign (as for a quadrupole field).

Since α must remain constant along any line of force, the value of α is zero (also for $\cos\lambda > 0$) on the entire separatrix

$$\sin\lambda^{(0)} = -2/3\kappa_g\,(r/R_E)\,. \tag{6.6}$$

Eq. (6.6) implies that the separatrix touches the south pole on the Earth (at $r = R_E$) for $\kappa_g = 3/2$ as shown in Fig. 6.2.

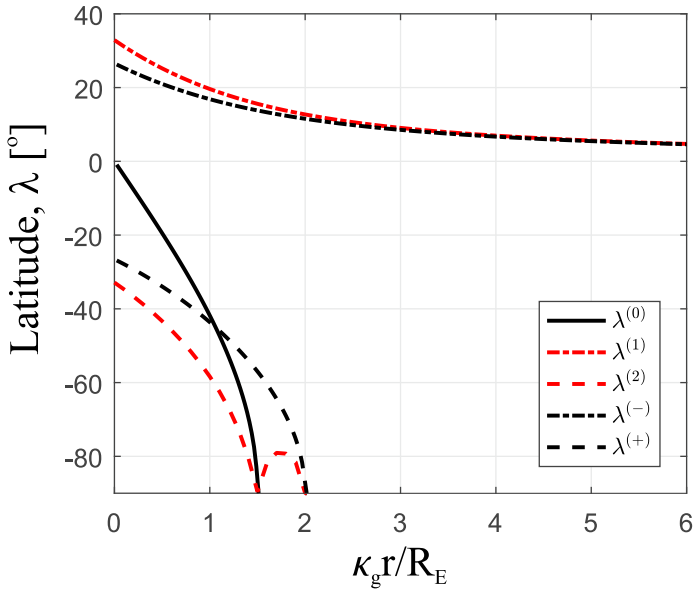

Figure 6.2: The magnetic latitudes $\lambda^{(1,2)}$ corresponding the points of minimum magnetic field strength along the force lines, magnetic latitude $\lambda^{(0)}$ of the separatrix between the northern and southern field lobes and magnetic latitudes $\lambda^{(\mp)}$ of metastable circular orbits as functions of the parameter $\kappa_g(r/R_E)$.

Axisymmetric quadrupole ($\kappa_g = 0$) is obtained by displacing the centers of two anti-collinear magnetic moments in the direction of the planet' rotation axis. As the parameter κ_g grow, i.e. as the dipole component in the superposition field increases, the magnetic moment directed to the north increases and the magnetic moment directed to the south decreases until it disappears. Thus, for values of $\kappa_g > 1.5$ (Eq. 6.6), the axisymmetric dipole prevails in the superposition of fields.

The locus of minima in magnetic field strength B along the force lines ($\mathbf{B}\cdot\nabla(B^2) = 0$) may be of particular interest for the adiabatic theory of charged particle motion (Shabansky (1971), pp. 372-380). It satisfies

$$2\kappa_g^3(r/R_E)^3x(5x^2+3) + \kappa_g^2(r/R_E)^2(65x^4+18x^2-3) + \\ + 3\kappa_g(r/R_E)x(45x^4-4^2+3) + 9(10x^6-5x^4+4x^2-1) = 0, \tag{6.7}$$

where $x = \sin\lambda$. At the limit of pure-quadrupole field $\kappa_g = 0$ ($g_1^0 = 0$) the last term of the

Eq. (6.7) yields a numerical solution $x^2 = 0.294563$ (hence $\lambda^{(1,2)} = \pm 32.87°$) for the cone consisting of minimum-B points along purely quadrupolar field lines, which corresponds to the conical surfaces in which the main capture of particles occurs in the quadrupole field (Vogt & Glassmeier, 2000). At the limit of pure-dipole field $\kappa_g \to \infty$ ($g_2^0 \to 0$) the minimum-B surface coincides with the equatorial plane ($x = 0$, hence $\lambda^{(1)} = 0°$). Fig. 6.2 shows the magnetic latitude $\lambda^{(1,2)}$ as a function of the parameter $\kappa_g(r/R_E)$. There is a bifurcation of the minimum-B surface at point $\kappa_g(r/R_E) = 1.48$ and $\lambda^{(2)} = -90°$.

Before proceeding to the investigation of the charged particle motion in the fields' superposition, we consider in detail the dynamics of a charged particle in a quadrupole magnetic field and recall the conclusions of the classical Störmer theory for a dipole field.

6.2 Störmer's theory and its development for a quadrupole field

In the present section we analyze in detail the trajectory of a charged particles moving from infinity to a quadrupole field, which is a special case of the more general work presented by Shebalin (2004), and compare it with the trajectories of motion in a dipole field, an analysis of which was described in the monograph of Störmer (1955).

Equating the centrifugal and Lorentz forces at the metastable circular orbits is

$$\frac{p^2}{mr\sin\theta}\vec{\nabla}(r\sin\theta) = q[\mathbf{v}\times\mathbf{B}], \tag{6.8}$$

where $\vec{\nabla}(r\sin\theta)$ is the unit vector perpendicular to the axis of symmetry. Therefore $\mathbf{B}\cdot\vec{\nabla}(r\sin\theta) = 0$ and the magnetic latitudes of metastable circular orbits are $\lambda^{(\mp)} = \pm 26.566°$ ($\sin^2\lambda^{(\mp)} = 0.2$) symmetric relative to the equatorial plane of the quadrupole.

Substitute the strength of the quadrupole magnetic field of Eqs. (6.2) and get

$$\frac{mv^2}{r\cos\lambda^{(\mp)}} = |q|vB = |q|v\frac{3}{2}\frac{|g_2^0|}{(r/R_E)^4}\sqrt{4\sin^4\lambda^{(\mp)} + \cos^4\lambda^{(\mp)}}, \tag{6.9}$$

At metastable circular orbits we express $r\cos\lambda$, called the Störmer radius of the particle in the quadrupole field as

$$c_{st,qp} = \sqrt[3]{\frac{|q|}{mv}\frac{3}{2}|g_2^0|R_E^4\cdot 0.8^{2.5}}. \tag{6.10}$$

Shebalin's Eq. (31a) defines Störmer radius as $r_S^{n+1} = ea_n/(np)$, where n is degree of

magnetic multipole component, and $a_n = g_n^0 R_E^{n+2}$. Thus in the quadrupole field Shebalin's and our Störmer radii are related through $c_{st,qp} = \sqrt[3]{3 \cdot 0.8^{2.5}}\, r_S$, in the dipole field $c_{st,dip} = r_S$.

The stationarity and axial symmetry of the quadrupole magnetic field presuppose the presence of two motion constants of charged particles: the total velocity $|v| = const$ and the canonical generalized momentum of the azimuthal motion

$$M_\phi = \rho\,(mv_\phi + eA_\phi) = const, \tag{6.11}$$

where $\rho = r\cos\lambda$ is the distance to the z axis. Since the particle energy is conserved in a stationary field, then the relativistic effects of particle motion is described by the same equations, where the mass is $m = m_0/\sqrt{1 - v^2/c^2}$ with the rest mass of particle m_0.

Our expression (6.11) of canonical (generalized) momentum M_ϕ (in SI units) coincides with Shebalin's Eq. (6) of canonical momentum P_ϕ (in CGS units) derived via rigorous Lagrangian theory.

We normalize the motion constant from Eq. (6.11) and then use it in the form of a dimensionless parameter $\gamma = -M_\phi/\,(2mvc_{st,qp})$. This normalization of canonical angular momentum γ differ from Shebalin's normalization $\tilde{\gamma} = P_\phi/\,([n+1]pr_S)$ in Eq. (31b). But in case of superposition, it is impossible to specify degree n. Therefore, Shebalin's definition of $\tilde{\gamma}$ is not suitable for our purposes. In the quadrupole field γ are related with Shebalin's $\tilde{\gamma}$ through $\gamma = 3/(2\sqrt[3]{3 \cdot 0.8^{2.5}})\tilde{\gamma}$, in the dipole field γ and $\tilde{\gamma}$ are same.

We introduce the angle δ between the meridional plane and the trajectory, so that $\sin\delta = v_\phi/v$. Then Eq. (6.11) can be rewritten in the form

$$M_\phi = mv\left(\rho\frac{v_\phi}{v} + \frac{c_{st,qp}^3}{0.8^{2.5}}\frac{\rho^2\sin\lambda}{r^4}\right) = -2mvc_{st,qp}\gamma, \tag{6.12}$$

or

$$r^3\cos\lambda\sin\delta + 2c_{st,qp}\gamma r^2 + c_{st,qp}^3\cos^2\lambda\sin\lambda/0.8^{2.5} = 0. \tag{6.13}$$

We have the cubic Eq. (6.13) with three roots $r_{1,2,3}$, which are easily found with the help of Cardano formula. Substitution of the quantity $\sin\delta = \pm 1$ in Eq. (6.13) gives formally six boundary values $r_1, r_2, \ldots, r_6(\lambda)$ to determine the allowed regions of motion for given values $c_{st,qp}$ and γ, corresponding to the two motion constants $|v|$ and M_ϕ.

Figures 6.3 and 6.4 show allowed and forbidden regions of protons' motion with an energy of 1 MeV for different values of the parameter γ in the meridian plane of the dipole and quadrupole fields, respectively. Pay attention to the existence of capture zones, internal allowed (colorless) areas surrounded by forbidden (red) areas. For the quadrupole, such

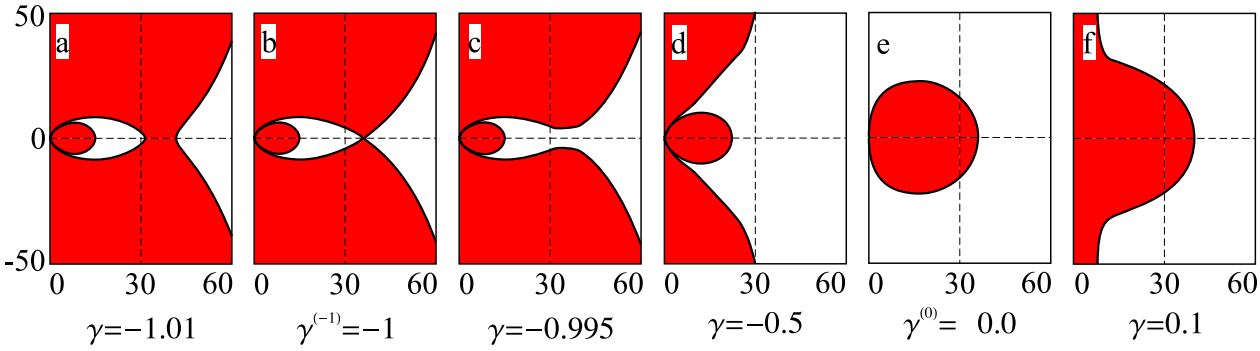

Figure 6.3: The forbidden regions (marked in red) of the axisymmetric dipole for different values of the parameter γ. The vertical and horizontal coordinates $z = r\sin\lambda$ and $\rho = r\cos\lambda$ of the meridian plane are measured in the Earth's radii R_E. Störmer radius is $c_{st,dip} = 36R_E$.

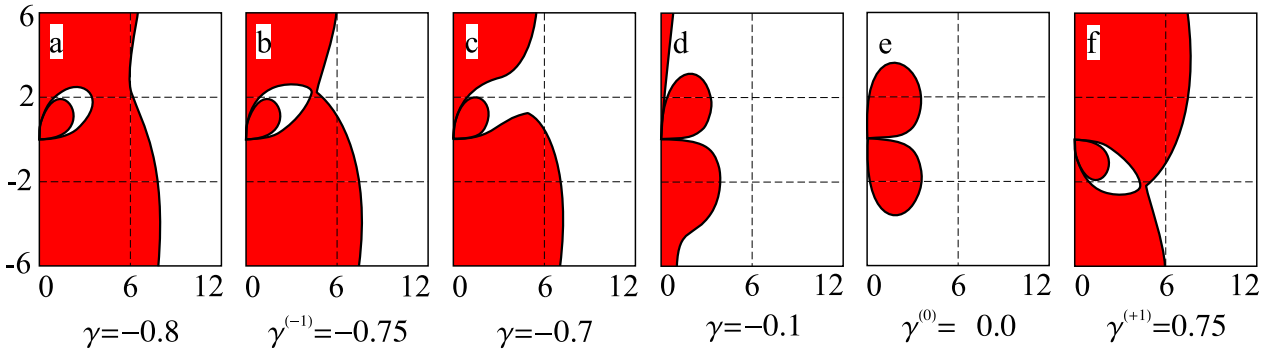

Figure 6.4: The forbidden regions (marked in red) of the axisymmetric quadrupole for different values of the parameter γ. The vertical and horizontal coordinates $z = r\sin\lambda$ and $\rho = r\cos\lambda$ of the meridian plane are measured in the Earth's radii R_E. Störmer radius is $c_{st,qp} = 4.5237R_E$.

regions of trapped particles can exist separately on two tori, which leads to two radiation belts and two ring currents. Figures 6.3 and 6.4 correspond to figures 1 and 2 presented by Shebalin (2004), respectively. The differences are that the coordinates of Shebalin's meridian plane are normalized not to the Earth's radius R_E, but to the Störmer radius r_S. In Fig. 6.4 the normalized canonical momenta $\tilde{\gamma}$ and γ also differ as described above.

Following the successively decreasing parameter $\gamma \in (-\infty; +\infty)$ (from a to f) in Figs. 6.3 and 6.4, it's easy to find that when $\gamma \leq \gamma^{(-1)}$ there is a (light) region of allowed trajectories (Figs. 6.3a, 6.4a), the inner region closest to the Earth is isolated from the outer space and forms a trap for the particles. In the dipole field (Fig. 6.3a), the inner capture region forms a toroid symmetrical with respect to the equatorial plane. In the quadrupole field (Fig. 6.4a), the toroidal capture region arises in the upper half-plane and ensures the stable existence of the northern radiation belt. This zone of finite motion always lies within the Störmer sphere

$r < c_{st}$, and its size decreases with increasing γ from $r = 1R_E$ to c_{st}; when $\gamma = \gamma^{(-1)}$ an unstable circular trajectory appears at the point of the forbidden zones separation $r = c_{st,dip}$ and $\lambda = 0°$ (Fig. 6.3b) or $r = c_{st,qp}$ and $\lambda^{(-)} = 26.6°$; when $\gamma^{(-1)} < \gamma < 0$ the inner allowed region opens for particles coming from infinity that penetrate the zones of the north and south poles, which narrow with increasing γ, in the dipole field (Figs. 6.3c,d) or into the zones of the north pole and equator in the quadrupole field (Figs. 6.4c,d); when $\gamma = 0$ there is one forbidden region in the dipole field (Fig. 6.3e) or two forbidden regions in the quadrupole field (Fig. 6.4e) symmetric with respect to the equatorial plane. The particles moving along $\lambda = \pm 90°$ or $\lambda = 0°$ reach the north and south poles (Fig. 6.3e) or the equator (Fig. 6.4e).

There are no particles reaching the dipole (Fig. 6.3f), when $\gamma > 0$. The forbidden regions of the quadrupole at $\gamma > 0$ (Fig. 6.4f) have the same form as the regions at $\gamma < 0$ (Fig. 6.4b), reflected from the equatorial plane.

The critical values of the parameters $\gamma_{qp}^{(-1,+1)}$ do not depend on the sort or energy of the particles and they are easily found by substituting $r = c_{st}$ and $\lambda^{(\mp)} = \pm 26.6°$ in Eq. (6.13):

$$\gamma_{qp}^{(-1,+1)} = -\frac{1}{2}\left(\frac{\cos^4\lambda^{(\mp)}\sin\lambda^{(\mp)}}{0.8^{2.5}} \pm 1\right) = \mp\frac{3}{4}. \tag{6.14}$$

In the quadrupole field with azimuthal symmetry, the threshold value Shebalin's $\tilde{\gamma}$ is $\tilde{\gamma}_c = \mp 5988$, in our notation $\gamma_{qp}^{(-1,+1)} = 3/(2\sqrt[3]{3 \cdot 0.8^{2.5}})\tilde{\gamma}_c = \mp 0.75$ which is similar to the found value in Eq. (6.14).

The Störmer radii of the dipole and quadrupole fields are inversely proportional to the roots of the second and third degree momenta $c_{st,dip} = 1/\sqrt{p}$ and $c_{st,qp} = 1/\sqrt[3]{p}$, respectively. Therefore the higher the particle energy, the shorter the Störmer radii and the closer the capture zone of the particle to the Earth (Fig. 6.5). With increasing energy the capture region approaches the Earth faster in the dipole than in the quadrupole. In other words, at the same energy, electrons are trapped farther from the Earth than protons. For example, for protons with the energy of 100 MeV are captured on 11 R_E from the Earth, and electrons with the same energy are captured on 75 R_E. Particles are able to reach the Earth's surface only at parameter values $\gamma^{(-1)} \leq \gamma \leq 0$ in the dipole and $\gamma^{(-1)} \leq \gamma \leq \gamma^{(+1)}$ in the quadrupole fields.

Substituting the parameter $\gamma_{qp}^{(-1,+1)}$ in Eq. (6.13), we can deduce the geomagnetic cutoff rigidity cp at which a charged particle moving at an angle δ to the meridian plane in the quadrupole field can reach a point with the coordinates r, λ. So for particles moving in the meridional plane of the quadrupole vertically at the angle $\delta = 0$, the rigidity of geomagnetic cutoff (in GeV) as a function of λ and r (in R_E) is expressed as

$$cp^{qp} = cg_2^0 R_E \frac{1.079}{10^9} \frac{|\sin\lambda|^{\frac{3}{2}} \cos^3\lambda}{(r/R_E)^3}, \quad cg_2^0 R_E \frac{1.079}{10^9} = 5.04\ GeV \tag{6.15}$$

The charged particles of low energies easily penetrate the poles $\lambda = \pm 90^\circ$ and equator $\lambda = 0^\circ$ of the Earth. The smallest number of particles reaches the Earth's surface at magnetic latitudes $\lambda^{(\mp)} = \pm 26.6^\circ$. The minimum momentum of particles falling vertically ($\delta = 0^\circ$) to these latitudes is 1.1 GeV. As the angle of the particles incidence δ increases, the necessary momentum grows. For particles penetrating horizontally, it's 5.5 GeV. Charged particles with smaller momenta will escape to the outer regions of the magnetosphere or form radiation belts. Vogt *et al.* (2007) derived formulas for the vertical cutoff rigidity in general axisymmetric multipole fields, see their Eq. (31), and in particular case of a quadrupole field, see their Eqs. (32) and (33), which differ from Eq. (6.15) by normalization to the polar surface strength of the present-day dipole field.

6.3 Superposition of the dipole and quadrupole fields

In accordance with the magnetic reversal scenario, we investigate the motion of a charged particle in the axisymmetric magnetic field **B** from Eq. (6.1) at the time-epoch of interest (via the ratio $\kappa_g = g_1^0/g_2^0$ corresponding to different stages of the system evolution).

According to balance between the Lorentz force and the centrifugal force, the latitudes at which metastable circular orbits can occur should be decided by requiring $\mathbf{B} \cdot \vec{\nabla}(r \sin\theta) = 0$, so that

$$\sin^2\lambda + 0.4\kappa_g(r/R_E)\sin\lambda - 0.2 = 0, \tag{6.16}$$

$$\sin\lambda^{(\mp)} = -0.2\kappa_g(r/R_E) \pm \sqrt{(0.2\kappa_g(r/R_E))^2 + 0.2} \tag{6.17}$$

As expected in the pure-quadrupole limit $\lambda^{(\mp)} = \pm 26.565^\circ$ and in the pure-dipole limit $\lambda = 0^\circ$. Fig. 6.2 shows how the northern $\lambda^{(-)}$ and the southern $\lambda^{(+)}$ latitudes depend on with $\kappa_g(r/R_E)$. At large distances (r/R_E) from the Earth and at high values of κ_g, the dipole component prevails, so the latitude $\lambda^{(-)}$ tends to 0°, while $\lambda^{(+)}$ go to 90°.

The difference between the exponents of r in the dipole and the quadrupole in the composition of the total field from Eq. (6.1) and the dependence of latitudes $\lambda^{(\mp)}$ on r in the equality of centrifugal and magnetic forces did not allow to express the Störmer radii $c_{st}^{(\mp)}$ for the fields superposition as a function of the momentum p in the explicit form. However the particle momentum p at the metastable circular Störmer orbit of radius $c_{st}^{(\mp)} = r\cos\lambda^{(\mp)}$ is expressed analytically as a function of $\kappa_g(r/R_E)$ via the Eqs. (6.8), (6.2) and (6.17) for

arbitrary κ_g.

$$p = \frac{|qg_2^0|R_E}{(r/R_E)^3}\sqrt{1-x^2}\sqrt{\kappa_g^2(r/R_E)^2\left[3x^2+1\right]+12\kappa_g(r/R_E)x^3+9/4\left[5x^4-2x^2+1\right]}, \quad (6.18)$$

where $x = \sin\lambda^{(\pm)}$.

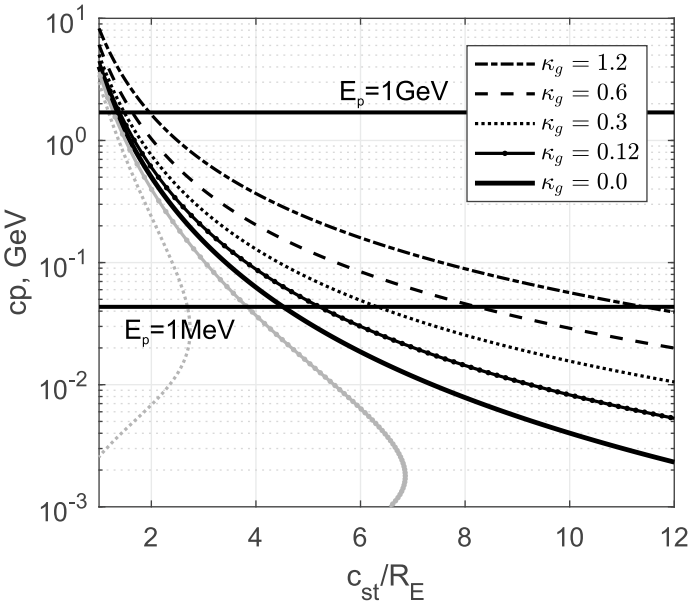

Figure 6.5: The particle momentum cp at the metastable circular orbit as a function of Störmer radius $c_{st}^{(\mp)}$ for selected values of $\kappa_g = g_1^0/g_2^0 =$ 1.2, 0.6, 0.3, 0.12, 0, ($g_2^0 = -0.025$ G is constant).

The Fig. 6.5 shows the decrease in the Störmer radius $c_{st}^{(\mp)}$ with an increase in the particle momentum cp (in GeV) for fields with different weighting factors κ_g. The Störmer radius $c_{st}^{(\mp)}$, $\lambda^{(\mp)}$ and $\gamma^{(\mp)}$ for protons with the kinetic energy $E = 1\ MeV$ are listed in Tab. 6.1. Since $cp = \sqrt{E(E+2m_0c^2)}$, in the Fig. 6.5 the protons' kinetic energies $E =$ 1MeV and 1GeV are marked with a black horizontal line.

Table 6.1: The northern $c_{st}^{(-)}$ and southern $c_{st}^{(+)}$ Störmer radii at the magnetic latitudes $\lambda^{(\mp)}$ of metastable circular orbits and corresponding $\gamma^{(\mp 1)}$ for protons with 1 MeV energy in the superposition fields with different values of κ_g.

κ_g	$c_{st}^{(-)}$, R_E	$\lambda^{(-)}(c_{st}^{(-)})$	$\gamma^{(-1)}$	$c_{st}^{(+)}$, R_E	$\lambda^{(+)}(c_{st}^{(+)})$	$\gamma^{(+1)}$
0.6	8.3	0°	-0.977	0.93	$-72.5°$	0.262
0.3	6.3	12°	-0.944	2.65	$-50°$	0.455
0.12	5.2	19°	-0.852	4.7	$-36°$	0.633
0	4.52	26.6°	-0.75	4.52	$-26.6°$	0.75

In contrast to the classical Störmer theory, for the given configuration of a superposition of the magnetic dipole and quadrupole, the parameters $\gamma^{(\mp 1)}$ in Tab. 6.1 are not constants

for particles of different sorts and energies, since they depend on the latitudes $\lambda^{(\mp)}\left(c_{st}^{(\mp)}\right)$ changing with the Störmer radii. With increasing parameter κ_g, in the northern hemisphere the Störmer radius $c_{st}^{(-)}$ increases, as does the particle stable capture region, simultaneously in the southern hemisphere the Störmer radius $c_{st}^{(+)}$ and the stable capture region decrease.

Eq. (6.12) for the superposition of the dipole and quadrupole fields is transformed as follows:

$$M_\phi = mv\left(\rho\frac{v_\phi}{v} + c_{st,dip}^2\frac{\rho^2}{r^3} + \frac{c_{st,qp}^3}{0.8^{2.5}}\frac{\rho^2\sin\lambda}{r^4}\right) = -2mvc_{st}^{(\mp)}\gamma, \tag{6.19}$$

or

$$r^3\cos\lambda\sin\delta + 2c_{st}^{(\mp)}\gamma r^2 + c_{st,dip}^2 r\cos^2\lambda + c_{st,qp}^3\cos^2\lambda\sin\lambda/0.8^{2.5} = 0, \tag{6.20}$$

where $c_{st,dip} = \sqrt{|qg_1^0|R_E^3/(mv)}$, $c_{st,qp}$ and $c_{st}^{(\mp)}$ are the Störmer radii of the dipole, quadrupole, and their superposition.

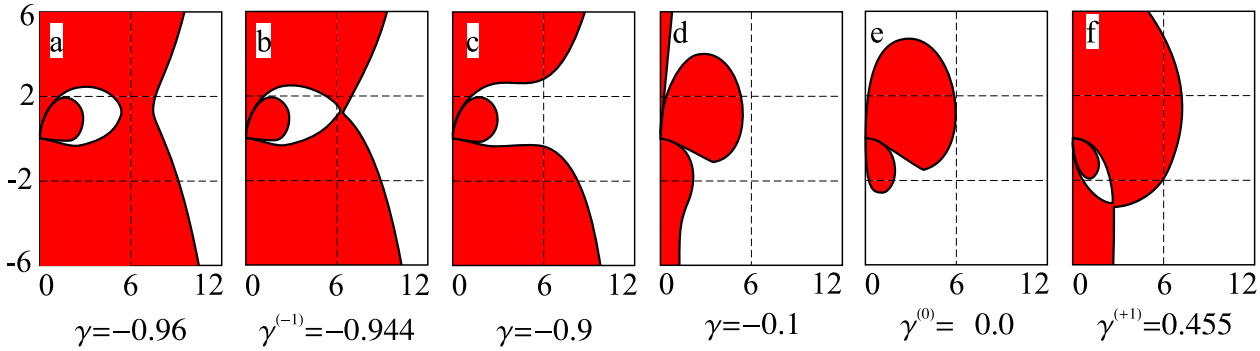

Figure 6.6: The forbidden regions (marked in red) for the superposition of axisymmetric dipole and quadrupole fields with the weighting factor $\kappa_g = g_1^0/g_2^0 = 0.3$ and different values of the parameter γ. The vertical and horizontal coordinates $z = r\sin\lambda$ and $\rho = r\cos\lambda$ of the meridian plane are measured in the Earth's radii R_E. Störmer radii are $c_{st}^{(-)} = 2.65R_E$ and $c_{st}^{(+)} = 6.3R_E$.

Figs. 6.6 show the allowed and forbidden regions of proton motion with 1 MeV energy in the dipole and quadrupole superposition with the weighting factor $\kappa_g = g_1^0/g_2^0 = 0.3$. When $\gamma = \gamma^{(-1)}$ (Fig. 6.6b) and $\gamma = \gamma^{(+1)}$ (Fig. 6.6f), the forbidden zones are connected at points $r = c_{st}^{(-)}$, $\lambda^{(-)} = 12°$ and $r = c_{st}^{(+)}$, $\lambda^{(+)} = -50°$. The northern capture region exceeds in size the southern one ($c_{st}^{(-)} > c_{st}^{(+)}$). When $\gamma = 0$ (Fig. 6.6) the forbidden areas are also not symmetric, particles can penetrate the poles located at magnetic latitudes $\lambda = \pm 90°$ and $\lambda^{(0)} = 0°$.

Thus, during the magnetic reversal, the southern radiation belt is filled by smaller number of particles than the northern one, and the particle spatial precipitation region, i.e. the separatrix between the northern and southern field lobes, is moving from the south to the

equator.

6.4 Conclusions

The magnetic field has two axisymmetric lobes in the quadrupole configuration and only one lobe in the dipole-dominated configuration. The superposition of axisymmetric fields having opposite parity (odd for dipolar, even for quadrupolar) introduces asymmetry between north and south. Studies of the dynamics of a charged particle in axially symmetric magnetic field have shown that, the particles capture region in the northern lobe exceeds in size the southern one (Figs. 6.6b,f), which, according to the reversal scenario of the Earth's magnetic field subsequently leads to an asymmetric distribution of radiation doses in the quadrupole belts. The separatrix (between the northern and southern field lobes) that provides another path for charged particles to penetrate the Earths ionosphere (instead of magnetic poles), migrates from the south to the equator with a decrease in the dipole component, that also corresponds to particle impact regions, illustrated by Stadelmann *et al.* (2010) and to the increase of the South polar cap, considered analytically by Vogt *et al.* (2007).

The complexity of the development of the Störmer theory for the dipole and quadrupole superposition is due to the fact that with increasing distance the field strengths weaken at different rates. For this reason, the particle momentum cp at the metastable circular orbit is expressed as a function of Störmer radius $c_{st}^{(\mp)}$ (Figs. 6.5) and not vice versa, as was done for the multipoles.

The axially symmetric configuration of the fields superposition allows to estimate the maximum of radiation dose in the near-earth space during the geomagnetic field reversal. However, other reversal scenarios are also possible. If the quadrupole assumes a quasi-axisymmetric configuration, then the radiation belts persist, but with smaller doses. And in the case of a nonaxisymmetric quadrupole configuration, the radiation belts can not stably exist. By the simulations of geomagnetic reversal a scenario of non-vanishing dipole moment with a rotating magnetic axis was shown. The axisymmetric superposition of fields may also be applicable for particular moments of such reversal scenario.

Chapter 7

Atmospheric escape during geomagnetic reversal

An open question for research is what happens to the atmosphere during the reversal process. According to the widely accepted concept, the magnetosphere protects the planetary atmosphere from erosion by the solar wind. In the absence of induced and convective electric fields, ionospheric ions cannot be accelerated to energies above the escape energy necessary to overcome the gravitational pull of the planet. Atmospheres of unmagnetized Mars and Venus, on the contrary, are subject to erosion, since the interplanetary magnetic field (IMF) easily reaches their ionosphere.

Can we expect the loss of a significant part of the Earth's atmosphere during the polarity transition, when the magnetic field strength decays to about 10% or less of its present value? For example, Wei *et al.* (2014) have suggested that geomagnetic reversal could significantly enhance the oxygen escape rate and be responsible for the mass extinction. On the other hand, a number of researchers (Gunell *et al.*, 2018; Strangeway *et al.*, 2010; Barabash, 2010), contrary to the above paradigm, supposed that no, we cannot, since the escape rate of ions is determined by the total energy transferred from the solar wind into the ionosphere and is thus limited by the transfer efficiency and the size of the interaction region of the solar wind and magnetosphere (Barabash, 2010). The present-day magnetosphere focuses the energy flux of the solar wind falling on the magnetopause into a small auroral zones. The energy flux in these zones is typically reaching values 10 – 100 times larger than in the case with no magnetosphere. It increases the ionospheric outflow of heavy ions (O^+), but has little effect on the light ones (H^+) (Brain *et al.*, 2013).

Gunell *et al.* (2018) have studied the dependence of the escape rate of ions on the magnetic moment of the planet. However, their rate estimates were obtained only for the magnetic

moment of dipole field. According to the simulation (Glatzmaier & Roberts, 1995), during the reversal, the dipole component of the magnetic field decays with time and the quadrupole one can become dominant. In this chapter we consider losses of the atmosphere of the Earth during the field reversals taking into account the quadrupole and the dipole components of the magnetic field. Since the quadrupole field also evolves in time, its magnitude and configuration at the reversal time may be random. And, for simplicity, we consider an axisymmetric quadrupole.

The main escape processes consist of Jeans escape, photochemical escape and sputtering for neutral particles (Brain *et al.*, 2016), and ion pickup and polar wind for charged particles. The mechanisms – sputtering, photochemical or charge exchange escape (Tian *et al.*, 2013) – described for neutral particle escape involve charged particles, therefore, a planetary magnetic field can influence their effectiveness.

Jeans escape is a classical thermal escape mechanism occurring when the energy of some particles in the high tail of distribution reach escape energy. Neutral atoms with energies exceeding the escape energy can also appear as a result of dissociative recombination of O_2^+, CO^+ and CO_2^+ ions. Sputtering is a result of Coulomb collisions between exospheric neutrals and energetic ions. Fast-moving ions (of the solar wind or magnetosphere origin) can escape from a magnetic trap if they exchange charge with neutrals in the atmosphere (charge-exchange escape). Planetary ions which occur in plasma flow are picked up and can escape (pickup escape). Ions escaping through open magnetic field lines in the polar region and cusps correspond to polar and auroral winds, see sec. 7.2.1 and 7.2.2.

Jeans and photochemical escape processes can be excluded from the further consideration since they do not depend on the magnetic field strength and configuration. Photochemical escape is not significant for Earth, since the energy of O-fast atoms arising in process of the dissociative recombination on Earth is not sufficient to overcome its gravity.

There are two possible scenarios of atmospheric erosion during reversal, depending on the magnitude of the magnetic field. If the intrinsic magnetic field is weaker or equal to the induced one, then the planet's ionosphere is directly affected by the solar wind, similarly to Mars and Venus (unmagnetized planets). Ionized atoms of the exosphere (mainly H for Earth), accelerated by the convection electric field in the solar wind, escape by the pickup process. Pickup ions can also produce sputtering of neutrals. The induced magnetosphere also contains some analogs of 'polar caps' with expansion of the ionospheric plasma driven by the ambipolar electric field (Dubinin *et al.*, 2017, 2011)

If the intrinsic magnetic field is stronger than the induced one, then it deflects the solar wind, thereby preventing ion pickup and sputtering, but contributes to the ions escape from

the polar caps and cusps, i. e. the polar and auroral wind outflows. According to (Slapak *et al.*, 2017), only an insignificant part of the weakly accelerated H^+ ions can be captured by the magnetic field and returned to the atmosphere.

7.1 Dayside magnetopause and plasmapause sizes

7.1.1 Magnetopause

Changes in the magnetosphere and plasmasphere sizes due to long-term geomagnetic variations of the dipole component were considered by Glassmeier *et al.* (2004); Siscoe & Chen (1975). But since during the reversal it is assumed that the Earth's magnetic field deviates from the current dipole configuration, and the quadrupole component dominates, we estimated the magnetosphere and plasmasphere sizes for an axisymmetric quadrupole configuration.

The pressure balance between the dynamic pressure of the solar wind and the magnetic pressure of the magnetosphere (excluding atmospheric pressure) reads:

$$p_{sw} = \left(B_p + B_{mc}\right)^2 / (2\mu_0), \tag{7.1}$$

where $p_{sw} = \rho_{sw} v_{sw}^2$ denotes the solar wind pressure (Pa), $\mu_0 = 4\pi \times 10^{-7}$ H/m is vacuum permeability B_p is the planet's magnetic field (T) and B_{mc} is the magnetic field of the magnetopause currents.

For a known magnetopause form, regardless of its scale, this sum can be represented as $B_p + B_{mc} = 2 f_0 B_p$, where f_0 is a form-factor. For the spherical magnetosphere a form-factor is $f_0 = 1.5$, and for a more realistic magnetopause shape (not a sphere) the coefficient $f_0 = 1.16$ (Voigt, 1995).

At the subsolar point of magnetopause, the dipole field strength is $B_{dip} = |g_1^0|(R_E/R_{s,dip})^3$, and the quadrupole field strength is $B_{quad} = 3/2|g_2^0|(R_E/R_{s,quad})^4$, where $g_{1,2}^0$ are the leading dipole and quadrupole Gaussian coefficients taken for 2015 year $g_1^0 = -29.4\ \mu$T and $g_2^0 = -2.5\ \mu$T from the IGRF-12 model of Thebault *et al.* (2015), and R_E and R_S are the Earth's radius and the magnetopause standoff distance.

Solar wind pressure changes over time (see sec. 7.2.4), so the dipole magnetopause standoff distance varies in the range $R_{s,dip} = 6 - 15\ R_E$. The quadrupole magnetopause standoff distance is:

$$R_{s,quad} = \sqrt[4]{\frac{3}{2}\frac{g_2^0}{g_1^0}\left(\frac{R_{s,dip}}{R_E}\right)^3} R_E = 2.3 - 4.6\ R_E. \tag{7.2}$$

The average magnetopause standoff distance of the dipole magnetosphere is 10 R_E at a solar wind speed of 500 km/s and a density of 2.5 particles/cm^3. The average magnetopause standoff distance of the quadrupole magnetosphere under the same conditions is 3.36 R_E. If the Earth magnetic field disappeared, the ionospheric plasma would stop the solar flux at a standoff distance of $R_{imb} = 1.2\ R_E$, (i. e. where solar wind dynamic pressure balances the thermal pressure of the ionosphere $p_{sw} = nkT$). Since $R_{s,quad} > R_{imb}$, the quadrupolar magnetic field alone could protect the ionosphere from direct solar influence.

Figure 7.1 shows a dipole (a) and quadrupole (b) field lines, and combines models of a open and closed dayside magnetospheres. The field lines disturbed by the solar wind correspond to Voigt (1981) model of the dayside magnetosphere, whose magnetic field is $\mathbf{B}_p + \mathbf{B}_{cf} + \mathbf{B}_{imf}$, where $\mathbf{B}_p$ is the intrinsic planet field (dipole and/or quadrupole), $\mathbf{B}_{cf}$ is the magnetic field of the Chapman-Ferraro current system and $\mathbf{B}_{imf}$ - IMF. The quadrupole magnetospheres, their field lines topology and the system of large-scale currents were investigated by Vogt *et al.* (2004) using the MHD modeling.

7.1.2 Magnetosphere and Plasmasphere

In the open magnetosphere model, first proposed by Dungey (1961) for the southward IMF, the reconnection (or fusion) of interplanetary and geomagnetic field lines partially opens the Earth's magnetic field to the solar wind (Fig. 7.1). The reconnection of the interplanetary and quadrupole field lines alternately opens the northern and southern lobes of the magnetic field when the IMF is directed southward and northward, respectively. Cross-tail current flows along y direction in northern lobe and against y in southern one.

The solar wind electric field $\mathbf{E}_{sw} = -[\mathbf{v}_{sw} \times \mathbf{B}_{sw}]$ is related to the electric field of the magnetospheric convection $\mathbf{E}_{convection} = k\mathbf{E}_{sw}$ and can be derived from the scalar potential Stern (1973)

$$\Phi_{convection} = k v_{sw} \left(B_{sw,z} y - B_{sw,y} z\right), \tag{7.3}$$

where $v_{sw} = 500$ km/s is the solar wind speed assumed to be uniform, $B_{sw,z} = -5$ nT, $B_{sw,y} = 0$ nT are the components of IMF, k is the efficiency of magnetic reconnection ($k \sim 0.2$ Levy *et al.* (1964)).

The magnetospheric convection potential is proportional to the size of the interaction region of the solar wind with the dayside magnetosphere, determined through its cross-

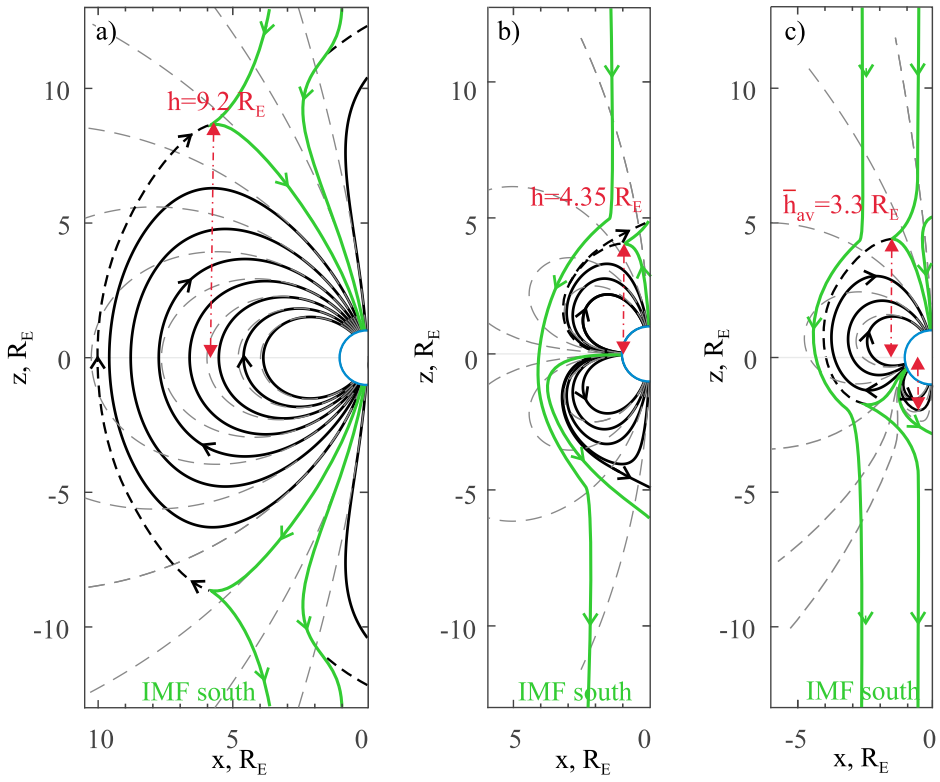

Figure 7.1: The field lines of the dipole (a), quadrupole (b) and mixed dipole-quadrupole (c) fields are perturbed (solid lines) and unperturbed (gray dashed) by the solar wind. Green lines are open field lines in the presence of the southward IMF. The height h is the maximum distance from the dayside magnetopause to the planet-sun line, indicated by the red arrows in panels (a) and (b); $\bar{h}_{av}$ is average of two heights indicated in panel (c).

sectional area πh^2, where h is the maximum distance from the dayside magnetopause to the planet-sun line, shown in Fig. 7.1. From the ratio of the cross-sectional areas of the dipole magnetosphere and half of quadrupole magnetosphere, taking into account that at any time only one lobe of the quadrupole magnetic field can be opened to the solar wind, it follows that convection potential of quadrupole magnetosphere is $\Phi^{quad}_{convection} = h^2_{quad}/2h^2_{dip}\Phi^{dip}_{convection} = 0.125\ \Phi^{dip}_{convection}$.

In a nonrotating Earth reference frame, the effective electrostatic potential includes the corotation potential Φ_Ω, which can be derived from the coefficients of the geomagnetic field spherical harmonics as follows:

$$\Phi_\Omega = [\mathbf{\Omega} \times \hat{\boldsymbol{r}}] \cdot \mathbf{A}, \quad [\mathbf{\Omega} \times \mathbf{r}] = \Omega r \sin\theta \hat{\boldsymbol{\varphi}}, \tag{7.4}$$

where $\mathbf{\Omega} = 2\pi/86400\ \mathbf{z}$ /s is the angular velocity of Earth's rotation, θ and ϕ are polar and azimuthal angles, respectively. The vector potential $\mathbf{A} = \alpha\vec{\nabla}\beta$ of the dipole and quadrupole

superposition is known from previous chapter (Eq. 6.3), hence $\Phi_\Omega(r,\theta) = \Omega\alpha(r,\theta)$.

The corotation electric field $\mathbf{E}_\Omega = -[\mathbf{\Omega}\times\mathbf{r}]\times\mathbf{B}$ causes the cold particles to rotate eastward along with the Earth (at any field configuration) with velocity $\mathbf{v}_E = [\mathbf{E}_\Omega \times \mathbf{B}]/B^2$.

The effective electrostatic potential for the cold ($\mu = mv_\perp^2/(2B) = 0$) particles motion is $\Phi_{eff} = \Phi_{convection} + \Phi_\Omega$. Remind that for hot particles of the plasmasheet, the potential of the gradient drift exceeds the corotational potential and leads to charge separation, i. e. the appearance of the electric field of polarization (Kivelson & Russell, 1995).

Figure 7.2 shows the equipotential lines Φ_{eff}, along which charged particles drift. The last closed equipotential line of the convection electric field in the magnetosphere is a plasmapause. The plasmapause divides the azimuthal flow of dense cold plasma, which rotates around the Earth continuously and forms the plasmasphere, and the convective plasma flow directed from the magnetotail to the dayside magnetopause.

As can be seen from Fig. 7.2, for the dipole configuration, the plasmapause field is located on the field lines at equatorial latitudes ($\Phi_\Omega^{dip}|_{\theta=0} = -87\ R_E/r$ kV). The nearest standoff distance to the plasmapause is 2.2 R_E. There is one point in the dusk meridian, where the flow velocity is zero (Kivelson & Russell, 1995), which represents an exact balance between competing processes of convection and corotation. At this point, $\partial\Phi_{eff}/\partial r = 0$, $\partial\Phi_{eff}/\partial\theta = 0$ $\partial\Phi_{eff}/\partial\varphi = 0$, from where $r_{zero-flow}^{dip} = \sqrt{\Omega R_E|g_1^0|/\left(k_{dip}v_{sw}|B_{sw,z}|\right)} = 5.2\ R_E$.

For a quadrupole, there are two points on the dusk meridian. One point is located at the northern latitude of metastable circular orbit $\theta = 63.4°$, when $B_{sw,z} < 0$, and another one is located at the southern latitude 116.6°, when $B_{sw,z} > 0$. A standoff distance from the point to the quadrupole axis is $r_{zero-flow}^{quad}\sin\theta = \sqrt[3]{3/2\Omega R_E|g_2^0|0.8/(k_{quad}v_{sw}|B_{sw,z}|)}\sqrt{0.8} = 2.5\ R_E$. The nearest standoff distance of plasmapause from the axis is 1.3 R_E.

7.1.3 Plasmaspheric plumes and wind

The plasmasphere expands during quiet times and then, during a main phase of a magnetospheric storm, is eroded by convection, producing sunward extending plumes. During the storm's recovery phase, the plasmasphere's outer region of a low density is refilled by an upward ionospheric plasma. At high geomagnetic activity the enhanced magnetospheric convection removes $\sim 50\%$ of mass of the plasmasphere. The mass fluxes in the plumes are $10^{25} - 10^{27}$ ions/s (Andrè & Cully, 2012; Welling *et al.*, 2015), much of which is lost via dayside reconnection. There is also a plasmaspheric wind that provides steady transport of cold plasma across the field lines from the plasmasphere with escape rate of 10^{25} ions/s.

Since the entire quadrupole plasmasphere lies inside the magnetosphere, i. e. $r_{zero-flow}^{quad} < R_{s,quad}$, the plumes are formed within the magnetosphere with the same intensity and regu-

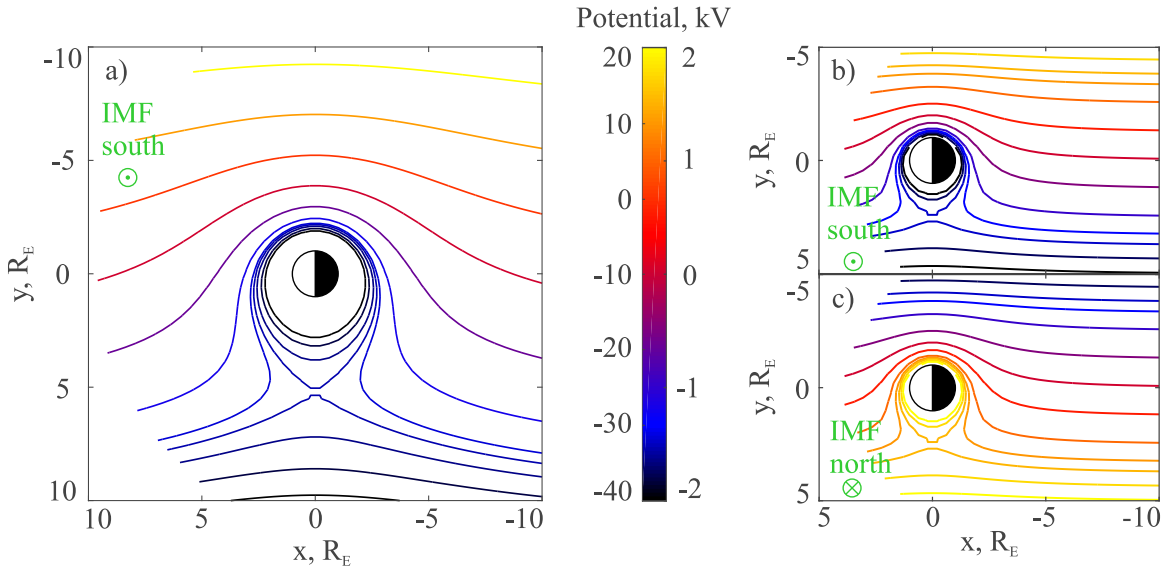

Figure 7.2: Equipotential contours of convection and corotation electric fields in dipole (a) and quadrupole (b) configurations at solar wind speed $v_{sw} = 500$ km/s. (a) in a plane $z = 0$: IMF is directed southward, $B_{sw,z} = -5$ nT; on a cone $z = \pm\sqrt{x^2 + y^2}/\tan 63.4°$: IMF is directed either southward (b) or northward (c). The reconnection of the interplanetary and quadrupole field lines alternately opens the northern and southern lobes of the magnetic field, respectively.

larity as in present field configuration. Thus, these loss mechanisms are weakly dependent on the magnetic field (Gunell *et al.*, 2018), but contribute to the total ion escape rate.

7.2 Ion acceleration mechanisms

The main sort of ions flowing from the ionosphere are singly charged oxygen (O^+), hydrogen (H^+) and helium (He^+). Ions escaping from the polar caps can be accelerated to keV energies in the cusp, or can remain cold drifting in the magnetotail (Nilsson *et al.*, 2012). We divided ion outflows into two categories: 'classical polar wind' and 'auroral wind' driven by solar radiation and by localized solar wind energy dissipation, respectively.

Ion outflows vary with solar EUV flux (F10.7 index), solar wind pressure (p_{sw}) and geomagnetic activity (Kp index). Higher X-ray and EUV radiation leads to an expansion of exosphere and higher escape rates at solar maximum or when the Sun was young (Lammer *et al.*, 2018). Solar wind dynamic pressure also plays a significant role in delivering energy to the ionosphere. Fok *et al.* (2005) found the gross dependence of auroral wind outflows (O^+/s) on solar wind dynamic pressure (nPa) fluctuations as $\log(Q_{aw,O^+}) = 25.97 \pm .64 + .61 \log(p_{sw})$.

7.2.1 Polar wind

The source of acceleration for the polar wind ions is an ambipolar (polarization) electric field that forms when the faster and mobile electrons begin to separate from the ions. It is affected by solar thermal irradiation (illumination). The polar wind is considered in the context of global ionospheric convection, with Joule dissipation and the precipitation of soft electrons (<500 eV) effects on the ambipolar electric field (Ogawa *et al.*, 2000; Strangeway *et al.*, 2005). Ions in the polar wind are convected into the plasma sheet and then sunward, replacing the denser plasma being removed toward the subsolar magnetosphere.

In the polar caps, we observe polar wind ions with escape rate $Q^{dip}_{0,pw,H} = 7.8 \times 10^{25}$ H^+/s Engwall *et al.* (2009) and $Q^{dip}_{0,pw,O} = 8 \times 10^{24}$ O^+/s (Yau & Andrè, 1997).

The escape rate of ions from the polar caps is proportional to their area (Gunell *et al.*, 2018) and could be expressed, for a quadrupolar configuration, through the ratio (see app. B)

$$Q_{pw,\alpha} = Q_{0,pw,\alpha}\frac{S_{quad}}{S_{dip}} = Q_{0,pw,\alpha}\frac{2\pi r^2_{exo,q}\Theta_{quad}}{2\pi r^2_{exo,d}\Theta_{dip}}, \tag{7.5}$$

where α is the sort of ions, $r_{exo} = 6871$ km is the exobase radius, defined as the altitude where the atmospheric scale height is equivalent to the mean free path. The exobase distance can increase to 7371 km at high solar activity. Position of the exobase does not change with a change of the field topology ($r_{exo,q} = r_{exo,d}$).

Assuming the average standoff distance to the dipole and quadrupole magnetopause, the ratio of the areas of open field line regions is $\Theta_{quad}/\Theta_{dip} = 0.112/0.11 = 1.01$ (see App. B). Thus, the total area of the polar caps and equatorial belt of the reversing quadrupole field almost coincides with the area of the polar caps of the present dipole field, therefore the escape rate of polar wind ions will change slightly. We note that in the quadrupole configuration, the area of the equatorial belt is 2 times higher the area of both polar caps.

If we consider the pure dipole magnetic field with the strength less in 10 times than the present value, then the average subsolar magnetopause standoff distance will be $R_{s,rev.\ dip} = \sqrt[3]{0.1}R_{s,dip} = 4.6\ R_E$, and the area of the polar caps will increase in $\Theta_{rev.\ dip}/\Theta_{dip} = 2.23$ times.

7.2.2 Auroral wind

The energization of ions in the cusp is caused by their resonant heating by broadband low-frequency electric field fluctuations (BBELF), which promote the formation of super-thermal and energetic upwelling ion population in the form of ion beams and conics (Yau & Andrè,

1997). Upwelling is the most stable ion outflow from the cusp, and is dominated by O^+ ions. It displays the effects of both parallel and perpendicular energization to energies from one to tens of eV. Pollock *et al.* (1990) estimated the outflow rate of upwelling ions from two hemispheres $Q_{0,upw,O^+} = 2 \times 10^{25}$ ions/s, $Q_{0,upw,H^+} = 0.5 \times 10^{25}$ ions/s and $Q_{0,upw,He^+} = 0.1 \times 10^{25}$ ions/s. We took these escape rates as average auroral wind rates.

It is not known whether BBELF waves are generated locally or propagate from the boundary of the magnetospheric region (Bouhram *et al.*, 2004). However, since transverse ion heating occurs in a wide range of heights and is partially controlled by the components of the IMF (Miyake *et al.*, 2000), it is assumed that the waves responsible for heating the ions can be generated in the dayside reconnection region. The energy of these waves with a frequency equal to the ion gyrofrequency (<10 Hz for O^+ at altitude of 2.5 – 6.5 R_E, 0.2 – 4.0 Hz for H^+ at altitude of 6 – 9 R_E (Le *et al.*, 2001)), is transmitted by plasma instabilities, as well as by the Poynting descending flux to a lower altitude in the ionosphere cusp.

The escape rate of auroral wind outflows is proportional to the area of cusp, which is part of the polar cap, and proportional magnetopause's cross section πh^2 (Gunell *et al.*, 2018), i. e. the energy flux of the solar wind falling on it. The escape rate increases with the magnetic moment of a dipole field until it reaches the maximum ion flux provided by the ionosphere. The maximum ion flux O^+, measured by the DE-1 spacecraft during the high solar and magnetic activity and integrated over both polar caps, is about 3×10^{26} ions/s (Yau & Andrè, 1997). This upper limit, reached by the outflow rate O^+, makes it possible to judge the effectiveness of the magnetospheric shield.

The escape rate of auroral wind outflows for the quadrupole configuration can be estimated as

$$Q_{aw,\alpha} = Q_{0,upw,\alpha} \frac{\pi h_{quad}^2}{\pi h_{dip}^2} \frac{S_{quad}}{S_{dip}}. \tag{7.6}$$

The areas of open field line regions in the two field configurations are almost the same $S_{quad}/S_{dip} \simeq 1.01$. And the ratio of the cross sections of the magnetospheres is $h_{quad}^2/h_{dip}^2 = 0.22$ (Fig. 7.1). Thus, the escape rate of auroral wind ions is reduced by 4.5 times.

For a dipole field with reduced strength of 10 times, this ratio is $h_{rev.\ dip}^2/h_{dip}^2 = 0.21$, but with $S_{rev.\ dip}/S_{dip} = 2.23$, the escape rate of auroral wind outflows will decrease by about 2 times.

7.2.3 Dipole-quadrupole magnetosphere

The field lines of the dipole-quadrupole magnetic field are defined by $\alpha(r, \theta)$ from Eq. 6.3. The latitudes of the polar caps boundaries (θ) satisfy the equality $\alpha(r_{exo}, \theta) = \alpha(R_s, \theta^{(\mp)})$,

where $\theta^{(\mp)}$ are the latitudes of metastable circular orbits. The solution of this equation is shown in the Fig. 7.3.

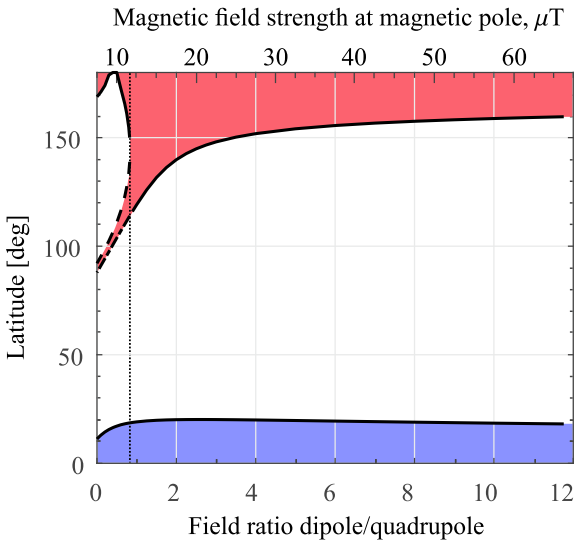

Figure 7.3: Polar cap boundary latitudes as a function of g_1^0/g_2^0 (dipole and quadrupole magnetic field strength ratio)

At $g_1^0/g_2^0 = 0$ the magnetic configuration is pure quadrupole one, there are three regions – a two polar caps and an equatorial belt, in which the field lines are open and connect to the solar wind. As the ratio g_1^0/g_2^0 increases, the equatorial belt moves to the southern polar cap where they connect at a point, marked by vertical line in the Fig. 7.3. After this line, the dipole component dominates in the magnetic field, the two polar caps, asymmetrical in size due to the quadrupole contribution, become smaller until they become equal.

Vogt *et al.* (2007) illustrated the change in the boundaries of the polar caps with an increase in the quadrupolar contribution to the dipole-quadrupole magnetosphere. They looked at several values of the dipole moment, the minimum of which one is about one-tenth of its present value. We have considered a change in the polar caps boundaries with a decrease in the dipole moment down to zero (Fig. 7.3).

The ion escape rates from the polar caps are proportional to their sizes depending on the magnetic field. Figure 7.4 shows the H^+ and O^+ ion escape rates as a function of magnetic field strength at the magnetic pole. Solid and dashed curves correspond to the mixed dipole-quadrupole configuration and purely dipole configuration considered by Gunell *et al.* (2018). Purple vertical line shows the reversing magnetic field without a dipole component. The total escape rate grows with decreasing magnetic field strength, but drops sharply when the field configuration is reversed and then increases again.

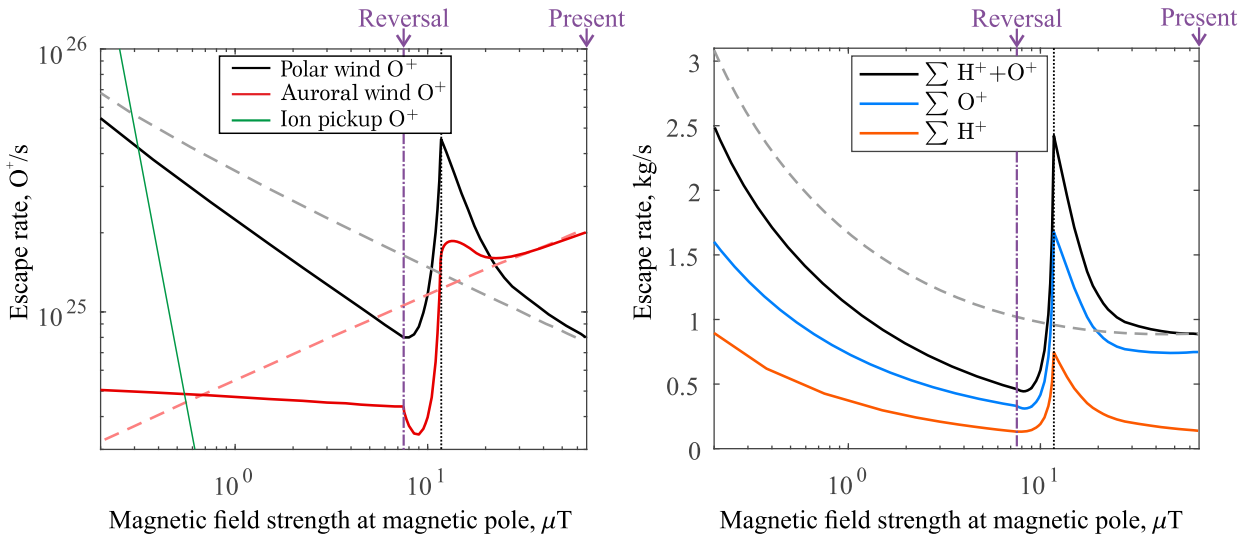

Figure 7.4: Hydrogen and oxygen ion escape rates as a function of magnetic field strength at the magnetic pole. Magnetic field is an axisymmetric superposition of dipole and quadrupole fields (solid lines) or a pure dipole field (dashed lines) as in Gunell *et al.* (2018) paper. Left: Oxygen ion escape rates for polar and auroral winds and ion pickup; Right: Total (polar and auroral) ion escape rates (without ion pickup).

7.2.4 Ion pickup

Scenario when the solar wind is in a direct contact with the Earth atmosphere/ionosphere was considered by Wei *et al.* (2014) similar as was done for the unmagnetized Mars (Lundin & Dubinin, 1992). The estimatel was based on the momentum transfer between the solar wind and planetary plasmas. The (accelerated) escaping magnetospheric flux (E) is related to the incident solar wind flux (sw) and the local (decelerated) solar wind flux (swE) as :

$$Q_{pickup} = \delta \frac{v_{sw} m_{sw}}{v_E m_E} \left(n_{sw} v_{sw} - \frac{v_{swE}}{v_{sw}} n_{swE} v_{swE} \right) A = n_E v_E A, \tag{7.7}$$

where v, m, n is speed, mass, density, $\delta = \delta_{sw}/\delta_E$ defines the relative momentum exchange thickness term (Pérez-de-Tejada, 1998)

$$\delta = \left(\frac{v_E}{v_{sw}} \right)^2 \frac{n_E m_E}{n_{sw} m_{sw}} \left(1 - \frac{n_{swE} v_{swE}^2}{n_{sw} v_{sw}^2} \right)^{-1}. \tag{7.8}$$

The typical solar wind density n_{sw} and velocity v_{sw} are 5 cm^{-3} and 400 km/s. Since solar wind particles are H^+, for a dominant O^+ population $m_{sw}/m_E = 1/16$. v_E is pick-up velocity for the terrestrial ions, using $v_E = 10$ km/s (the Earth escape speed near the MP). From the Mars observations, the speed and density of the decelerated solar wind are $v_{swE} = 40$ km/s

and $n_{swE} = 1$ cm^{-3}.

The cross section of the momentum transfer (MT) region, where the transfer of solar wind energy and momentum takes place, is defined as $A = \pi\,(R_{MLB}^2 - R_{MP}^2)$, it lies between the mass loading boundary (MLB) and the magnetopause (MP) at the terminator. The MLB represents the diffuse outer boundary encompassing the region of heavy mass-loading of the solar wind by terrestrial plasma and neutral gas. The distance of MLB is $R_{MLB} = R_{MP} + \delta(R_{MP} - R_E - 100\ km)$.

Wei *et al.* (2014) suggested that for high values of the density of the terrestrial O^+ ions in the interaction region the escape rate might be significant. For example, taking $n_E = 3 \times 10^3$ cm^{-3}, when $R_{MP} = R_{imb} = 1.2\ R_E$, one obtain $Q_{pickup} = 1.5 \times 10^{28}$ O^+/s.

7.3 Conclusion

It is shown that during the reversal of the geomagnetic field the standoff distance of the quadrupole magnetosphere is about of 3 R_E and therefore a magnetic shielding of the Earth atmosphere is still effective. The Earth's intrinsic magnetic field protects the atmosphere from sputtering and ion pickup (Lammer *et al.*, 2007), but contributes to the polar and auroral winds through open field lines from polar caps and cusps. We assume that the main sources of polar and auroral winds are solar illumination and solar wind energy, respectively. Both escape processes are proportional to the area of open field line regions. The auroral wind also depends on the cross-sectional area of interaction of the solar wind and the magnetosphere.

Since the magnetic moment of the dipole field decreases during the geomagnetic reversal, the area of the polar caps and the ion escape rate from them increases until the magnetic field configuration changes. A change in the field configuration leads to the emergence of new quadrupole equatorial belt and two polar caps, their total area reaches a minimum when the dipole component disappears (the pure quadrupole configuration), therefore, the total ion escape rate drops sharply and then increases with decreasing quadrupole field strength (Fig. 7.4). Table 7.1 gives average estimates of the escape rates of ionospheric ions at the time of reversal for the dipole and quadrupole field configurations.

The atmosphere plays a key role in protecting earthly life from radiation. In chapter 5 we estimated the radiation doses on Earth from cosmic rays during magnetic field reversal, assuming the thickness of the Earth's atmosphere to be unchanged. According to our estimates, the escape rates of atmospheric particles during the reversal process will increase by 2.5 times (Fig. 7.4), i. e. the atmosphere will become slightly thinner, but by the time of the reversal the escape rates will decrease by 2 times, and the atmosphere will become a little

Table 7.1: Escape rates of ionospheric hydrogen and oxygen ions for the present dipole field, quadrupole reversing field and weak dipole (i. e. with magnetic field strength ratio $g_1^0/g_2^0 = 0.8$)

Ions Escape	Present-day Dipole	Reversing Quadrupole	Weak Dipole
Auroral wind H^+/s	5×10^{24}	1.1×10^{24}	2.3×10^{24}
Polar wind H^+/s	7.8×10^{25}	7.9×10^{25}	1.7×10^{26}
Auroral wind O^+/s	2×10^{25}	4.4×10^{24}	9.4×10^{24}
Polar wind O^+/s	8×10^{24}	8.1×10^{24}	1.8×10^{25}
Total escape kg/s	**0.9**	**0.5**	**1.1**

more dense. Thus, in order to estimate doses, we can assume that the Earth's atmosphere does not change on average during the reversal period.

Chapter 8

Conclusion

Since the discovery of substorms in 1964, the processes causing explosively auroral brightenings have been causally associated with a very fast the release from nightside magnetosphere. Most probably through a magnetic reconnection process energy stored in the stretched magnetotail is suddenly and unpredictably released in the form of energised particle populations, enhanced current systems and enrichments of the Van Allen Radiation belts. Later, an another scenario was proposed for the initiation an auroral substorm deep in a closed field line region, where reconnection is likely not to occur. In this near-Earth region the trapped electrons bounce with periods of a few tens of seconds coinciding with the periods of wave activity observed at substorm breakups.

The theoretical study aims to investigate the resonant interaction between electromagnetic fluctuations with trapped bouncing electrons in the near-Earth tail of the magnetosphere ($8\ R_E < L < 12\ R_E$), characterized by a high density gradient $\vec{\nabla} n \parallel \vec{e}_x$ and a small field line curvature. Assuming a low plasma $\beta \ll 1$, only parallel currents and torsional perturbations are considered in this first study. Starting with a particle distribution function respecting the invariance along the y-axis, the Vlasov equation is integrated along the unperturbed particle trajectories, including cyclotron and bounce motions. A Fourier expansion has been assumed first to model the spatial structure of the electromagnetic potential and second to decompose the bounce motion. Only the first term of these expansions has been conserved in this first analysis but generalizations with other harmonics are possible. Ion cyclotron effects have also been neglected in this first approach of the problem and could be possibly included in future investigations. Taking these restrictions into account, integration over cyclotron motion and electron bounce oscillations allows to write perturbed distribution functions as a linear combination of potentials. The dispersion relation is then obtained analytically via the plasma quasi-neutrality condition and Ampere's law for the parallel current. This system

supports the propagation of waves with similar polarization and characteristics as Alfvén waves but they are strongly damped. The unstable mode has little to do with Alfvén waves. It is more similar to an electrostatic drift wave with a wave impedance increasing strongly with the frequency. This instability develops principally on the plasma inhomogeneity regardless magnetic perturbations.

Unstable electromagnetic drift modes have been found to propagate in the positive y-direction, i.e., in the same direction as the ion drift (westwards) with a phase velocity of the order of the ion drift velocity. These modes oscillate at about the thermal electron bounce period ($\sim$13.6 s) with the wavelength of the order of the ion Larmor radius (112 km). The growth rate strongly depends on the slope of the density gradient. For typical gradient scales larger than 2 R_E, drift effects are too weak to produce a fast growing instability, as the e-folding time of the perurbations is longer than a few minutes. The mode becomes potentially unstable with e-folding time less than 1 minute if the density gradient steepens with scale less than 0.5-1 R_E. This instability threshold depends on the Alfvén velocity at equatorial plane and on the magnetic L-shell. It has been showed that a larger Alfvèn velocity tends to stabilize the plasma sheet and a much sharp density gradient is required to get large growth rate. On the other hand, the instability threshold presents a maximum along the L-shell meaning that the electromagnetic drift instability may develop more easily on a particular magnetic shell depending on its perpendicular wavelength. The present treatment is still somewhat limited by several assumptions that we plan to reconsider in the near future. First cyclotron effects may be important to include in order to regularize the behaviour of the instability at larger wavenumber and higher frequencies. Second, a full electromagnetic theory that includes the curvature effects is still needed to model a similar type of electromagnetic bounce instability in a stretched magnetotail configuration.

Some authors have nevertheless reported observations of aurora arcs with a beading structure (Lui, 2016; Kalmoni *et al.*, 2015; Miyashita *et al.*, 2018) that could be a visual manifestation of this drift-Alfvén instability. From the all-sky images (ASI) of auroral arcs they found that the growth rate of the instability covers the range $0.02 - 0.3\ s^{-1}$. With a typical bounce period of 15 s, this corresponds to normalized growth rate comprised between 0.3 and 4.5 which matches the founded growth rate with density gradient scale of the order of 0.5 R_E.

A precise comparison between observations of auroral arcs and the theoretical results of our model was carried out on the example of the isolated weak substorm onset event at 04:54:30 UT on 3 February 2008. At the time of this event, three satellites TH-A, TH-D and TH-E were located sufficiently close to the current sheet, so their data were useful to

determine the diamagnetic drift. We investigated the wave-like arc in the ionosphere and the magnetic field disturbances in the near-Earth plasma sheet to find their temporal (real and imaginary frequency components) and spatial (wavenumber) evolution in order to compare them with our instability theory.

From auroral data, we identified the wave-like structure propagating westward with the magnetospheric phase speed $v_\perp \approx 127$ km/s. Azimuthal magnetospheric wavelength is $\lambda_\perp = 1650$ km and the growth rates peak is 0.05/s. At the same time, in the near-Earth plasma sheet at TH-A, TH-D and TH-E, we observe an increase in the density gradient and in the perturbations of magnetic field with the frequency components well approximating the theoretical ones.

According our theory, the electromagnetic drift waves propagate in the positive y-direction, i. e., in the same direction as the ion drift (westwards) with a phase velocity of the order of the ion drift velocity. These modes oscillate at about the thermal electron bounce period $2 \cdot 6.38$ s with a wavelength (830 km) smaller than the ion Larmor radius. A stronger diamagnetic drift is required so that the dispersion curve approximates the observed one. However, the growth rate curves are in good agreement with the curves observed at TH-A and TH-D at the diamagnetic drifts measured by satellites. If we change some plasma parameters to make the azimuthal magnetospheric wavelength comparable to the ion gyroradius (according (Kalmoni *et al.*, 2015)), our dispersion relation can reproduce the characteristic linear relationship between angular frequency and spatial scales of auroral wave-like signatures. But the observed growth rate still will be two times smaller than theoretical one. Therefore, we suppose that the link between the growth rates of auroral and magnetic waves is not linear as in the works of Kalmoni *et al.* (2015, 2018).

Thus the output of this new kinetic model can help substantially to understand the triggering processes of instability in the near-Earth region at the origin of some aurora arcs.

Earth's global magnetic field generated by an internal dynamo mechanism has been continuously changing on different time scales since its formation. Paleodata indicate that relatively long periods of evolutionary changes can be replaced by quick geomagnetic reversals. Based on observations, Earth's magnetic field is currently weakening and the magnetic poles are shifting, possibly indicating the beginning of the reversal process. We considered a possible scenario of the disappearance of the dipole component of the geomagnetic field during Earth's magnetic dipole reversal. An $\alpha\Omega$-dynamo model for the dipole and quadrupole field components was constructed. We considered two possible reversal scenarios: 1) with quadrupole and 10%-dipole magnetic fields, and 2) only with a quadrupole field. For both

scenarios, we calculated GCR and SCR proton spectra and their flux distributions across Earth and estimated the change in the effective proton radiation doses.

We have shown that, assuming constant atmospheric properties, the mean effective doses of GCR protons (SCR protons make a minor contribution) should increase about three-fold over the 2015 level. It has been shown that the magnetic field configuration change will result in the redistribution of higher radiation regions over Earth's surface (these regions are now located around the North and South Magnetic Poles), which can have negative effects on the health of the human population in these regions.

On Earth, the radiation mainly caused by GCR particles inversely correlates with solar activity periods, i. e., it reaches a maximum during the solar activity minimum. As for the ISS, the maximum radiation caused by SCR and GCR particles correlates with the maximum solar activity, because SCR particles mainly contribute to the radiation environment in the ISS orbit. Estimates show that during a reversal at the maximum solar activity the power of SCR and GCR effective doses in the ISS orbit (at the latitude of 51.6° and altitude of 400 km) should increase by a factor of 14 compared to the 2015 level, which is due to the latitudinal redistribution of the radiation. Undoubtedly, in this case, a correction of the orbits of space vehicles would be required. It should be stressed that the issues of the impact of elevated radiation dose on Earth's biosphere and the long-term evolution of the magnetosphere during magnetic reversals remain poorly understood and require more in-depth studies.

To study the changes in radiation belts during the reversal, we assumed the third reversal scenario in which the quadrupole magnetic field configuration is an axisymmetric one. Since if the quadrupole assumes a quasi-axisymmetric configuration, then the radiation belts persist, but with smaller doses. And in the case of a nonaxisymmetric quadrupole configuration, the radiation belts can not stably exist.

Studies of the dynamics of a charged particle in axially symmetric magnetic field have shown that, the particles capture region in the northern lobe exceeds in size the southern one, which, according to the reversal scenario of the Earth's magnetic field subsequently leads to an asymmetric distribution of radiation doses in the quadrupole belts. The separatrix between the northern and southern field lobes that provides another path for charged particles to penetrate the Earths ionosphere (instead of magnetic poles), migrates from the south to the equator with a decrease in the dipole component.

The atmosphere plays a key role in protecting earthly life from radiation. We estimated the radiation doses on Earth from cosmic rays, assuming the thickness of the Earth's atmosphere to be unchanged during magnetic field reversal. But this is not entirely true. During the reversal of the geomagnetic field the standoff distance of the quadrupole magnetosphere

is about of 3 R_E and therefore a magnetic shielding of the Earth atmosphere is still effective. We considered basic mechanisms of atmospheric particle acceleration such as Jeans escape, photochemical escape and sputtering for neutral particles (Brain *et al.*, 2016), and ion pickup and polar wind for charged particles and find that the Earth's intrinsic magnetic field protects the atmosphere from sputtering and ion pickup, but contributes to the polar and auroral winds through open field lines from polar caps and cusps.

We assume that the main sources of polar and auroral winds are solar illumination and solar wind energy, respectively. Both this escape processes are proportional to the area of open field line regions. The auroral wind also depends on the cross-sectional area of interaction of the solar wind and the magnetosphere. Since the magnetic moment of the dipole field decreases during the geomagnetic reversal, the area of the polar caps and the ion escape rate from them increases until the magnetic field configuration changes. A change in the field configuration leads to the emergence of new quadrupole equatorial belt and two polar caps, their total area reaches a minimum when the dipole component disappears (the pure quadrupole configuration), therefore, the total ion escape rate drops sharply and then increases with decreasing quadrupole field strength.

We estimated the escape rates of ionospheric ions (H^+ and O^+) at the time of reversal for the dipole and quadrupole field configurations. According to our estimates, the escape rates of atmospheric particles during the reversal process will increase by 2.5 times, i. e. the atmosphere will become slightly thinner, but by the time of the reversal the escape rates will decrease by 2 times, and the atmosphere will become a little more dense. Thus, in order to estimate doses, we can assume that the Earth's atmosphere does not change on average during the reversal period.

Bibliography

Akasofu, S.-I. 1964 The development of the auroral substorm. *Planetary and Space Science* **12** (4), 273–282.

Andrè, M. & Cully, C. M. 2012 Low-energy ions: A previously hidden solar system particle population. *Geophysical Research Letters* **39** (3), L03101.

Antonov, R. A. 2007 *Radiation conditions in the lower part of the Earths atmosphere (up to heights of 50-60 km)*, , vol. 1. Moscow: KDU.

Antonsen, Jr., T. M. & Lane, B. 1980 Kinetic equations for low frequency instabilities in inhomogeneous plasmas. *Physics of Fluids* **23**, 1205–1214.

Baker, D. N., Pulkkinen, T. I., Angelopoulos, V., Baumjohann, W. & McPherron, R. L. 1996 Neutral line model of substorms: Past results and present view. *Journal of Geophysical Research (Space Physics)* **101** (A6), 12,975–13,010.

Barabash, S. 2010 Venus, Earth, Mars: Comparative Ion Escape Rates. In *EGU General Assembly Conference Abstracts*, *EGU General Assembly Conference Abstracts*, vol. 5308.

Bellan, P. M. 2008 *Fundamentals of Plasma Physics*. Cambridge, UK: Cambridge University Press.

Bespalov, V. I. 2006 *The Interaction of Ionizing Radiation with Matter. [in Russian]*. Tomsk: TPU Publ.

Black, D. I. 1967 Cosmic ray effects and faunal extinctions at geomagnetic field reversals. *Earth and Planetary Science Letters* **3**, 225–236.

Bouhram, M., Klecker, B., Miyake, W., Rème, H., Sauvaud, J.-A., Malingre, M., Kistler, L. & Blăgău, A. 2004 On the altitude dependence of transversely heated o+ distributions in the cusp/cleft. *Annales Geophysicae* **22**, 1787–1798.

Brain, D. A., Bagenal, F., Ma, Y.-J., Nilsson, H. & Wieser, G. S. 2016 Atmospheric escape from unmagnetized bodies. *J. Geophys. Res. Planets* **121**.

Brain, D. A., Leblanc, F., Luhmann, J. G., Moore, T. E. & Tian, F. 2013 *Planetary magnetic fields and climate evolution. In Comparative Climatology of Terrestrial Planets*. Univ. of Arizona, Tucson.

Clement, B. M. 1991 Geographical distribution of transitional vgps: Evidence for non-zonal equatorial symmetry during the matuyama-brunhes geomagnetic reversal. *Earth and Planetary Science Letters* **104** (1), 48–58.

Clement, B. M. & Kent, D. V. 1984 Latitudinal dependency of geomagnetic polarity transition durations. *Nature* **310** (5977), 488–491.

Clement, B. M. & V., K. D. 1985 A comparison of two sequential geomagnetic polarity transitions (upper olduvai and lower jaramillo) from the southern hemisphere. *Physics of the Earth and Planetary Interiors* **39** (4), 301–313.

Cox, A. & Doell, R. R. 1960 Review of Paleomagnetism. *Geological Society of America Bulletin* **71** (6), 645.

Doake, C. S. M. 1978 Climatic change and geomagnetic field reversals: A statistical correlation. *Earth and Planetary Science Letters* **38** (2), 313–318.

Dubinin, E., Fraenz, M., Fedorov, A., Lundin, R., Edberg, N., Duru, F. & Vaisberg, O. 2011 Ion energization and escape on mars and venus. *Space Science Reviews* **162** (1), 173–211.

Dubinin, E., Fraenz, M., Pätzold, M., McFadden, J., Halekas, J. S., DiBraccio, G. A., Connerney, J. E. P., Eparvier, F., Brain, D., Jakosky, B. M., Vaisberg, O. & Zelenyi, L. 2017 The effect of solar wind variations on the escape of oxygen ions from mars through different channels: Maven observations. *Journal of Geophysical Research: Space Physics* **122** (11), 11,285–11,301.

Dungey, J. W. 1961 Interplanetary magnetic field and the auroral zones. *Phys. Rev. Lett.* **6**, 47–48.

Engwall, E., Eriksson, A. I., Cully, C. M., Andrè, M., Torbert, R. & Vaith, H. 2009 Earth's ionospheric outflow dominated by hidden cold plasma. *Nature Geoscience* **2** (1), 24–27.

Erickson, G. M. 1995 Substorm theories: United they stand, divided they fall. *Rev. Geophys.* **33**, 685–692.

Fok, M.-C., Ebihara, Y. & Moore, T. 2005 Inner magnetospheric plasma interaction and coupling with the ionosphere. *Adv. Polar Upper Atmos. Res.* **19**.

Fried, B. & Conte, S. 1961 *The Plasma dispersion function*. Academic Press Inc. New York.

Fruit, G., Louarn, P. & Tur, A. 2013 Electrostatic "bounce" instability in a magnetotail configuration. *Physics of Plasmas* **20** (2), 022113.

Fruit, G., Louarn, P. & Tur, A. 2017 Electrostatic drift instability in a magnetotail configuration: The role of bouncing electrons. *Physics of Plasmas* **24** (3), 032903.

Galper, A. M. 2002 *Kosmicheskie Luchi (Cosmic Rays)*. Moscow: MIFI.

Glassmeier, K.-H., Richter, O., Vogt, J., Möbus, P. & Schwalb, A. 2009*a* The Sun, geomagnetic polarity transitions, and possible biospheric effects: review and illustrating model. *International Journal of Astrobiology* **8** (3), 147–159.

Glassmeier, K.-H., Soffel, H. & Negendank, J. F. W. 2009*b* *Geomagnetic Field Variations*. Berlin: Springer-Verlag.

Glassmeier, K. H. & Vogt, J. 2010 Magnetic polarity transitions and biospheric effects. *Space Sci. Rev.* **155**, 387–410.

Glassmeier, K.-H., Vogt, J., Stadelmann, A. & Buchert, S. 2004 Concerning long-term geomagnetic variations and space climatology. *Annales Geophysicae* **22** (10), 3669–3677.

Glatzmaier, G. A. 2002 Geodynamo simulations – how realistic are they? *Ann. Rev. Earth Planet. Sci.* **30**, 237–257.

Glatzmaier, G. A. & Roberts, P. H. 1995 A three-dimensional self-consistent computer simulation of a geomagnetic field reversal. *Nature* **377** (6546), 203–209.

Glatzmaier, G. A. & Roberts, P. H. 1997 Simulating the geodynamo. *Contemporary Physics* **38** (4), 269–288.

Gubbins, D. 1994 Geomagnetic polarity reversals: A connection with secular variation and core-mantle interaction? *Reviews of Geophysics* **32** (1), 61–83, arXiv: https://agupubs.onlinelibrary.wiley.com/doi/pdf/10.1029/93RG02602.

Gubbins, D. 1999 The distinction between geomagnetic excursions and reversals. *Geophysical Journal International* **137** (1), F1–F3.

Gubbins, D. & Kelly, P. 1995 On the analysis of paleomagnetic secular variation. *Journal of Geophysical Research: Solid Earth* **100** (B8), 14955–14964, arXiv: https://agupubs.onlinelibrary.wiley.com/doi/pdf/10.1029/95JB00609.

Gunell, H., Maggiolo, R., Nilsson, H., Wieser, G. S., Slapak, R., Lindkvist, J., Hamrin, M. & De Keyser, J. 2018 Why an intrinsic magnetic field does not protect a planet against atmospheric escape. *Astronomy and Astrophysics* **614** (L3).

Haerendel, G. 2000 Outstanding issues in understanding the dynamics of the inner plasma sheet and ring current during storms and substorms. *Adv. Space Res.* **25**, 2379–2388.

Harrison, C. G. A. 1966 Behaviour of the Earth's Magnetic Field During a Reversal. *Nature* **212** (5067), 1193–1195.

Hasegawa, A. 1975 *Plasma instabilities and nonlinear effects*, , vol. 8. Springer Verlag Springer Series on Physics Chemistry Space.

Hess, H. H. 1962 *History of Ocean Basins*. CO: Geological Society of America.

Hilton, H. H. & Schulz, M. 1973 Geomagnetic potential in offset-dipole coordinates. *J. Geophys Res.* **78**, 2324–2330.

Hoffman, K. 1992 Dipolar reversal states of the geomagnetic field and coremantle dynamics. *Nature* **359**, 789–794.

Hoyng, P. 1993 Helicity fluctuations in mean field theory: An explanation for the variability of the solar cycle? *Astronomy and Astrophysics* **272**, 321.

Hull, A. J., Chaston, C. C., Frey, H. U., Fillingim, M. O., Goldstein, M. L., Bonnell, J. W. & Mozer, F. S. 2016 The "alfvénic surge" at substorm onset/expansion and the formation of "inverted vs": Cluster and image observations. *Journal of Geophysical Research: Space Physics* **121** (5), 3978–4004.

Hurricane, O. A., Pellat, R. & Coroniti, F. V. 1994 The kinetic response of a stochastic plasma to low frequency perturbations. *Geophysical Research Letters* **21**, 253–256.

Jacobs, J. A. 1994 *Reversals of the Earth's magnetic field*. UK: 2nd edition, Cambridge Univ. Press.

Kalmoni, N. M. E., Rae, I. J., Murphy, K. R., Forsyth, C., Watt, C. E. J. & Owen, C. J. 2017 Statistical azimuthal structuring of the substorm onset arc: Implications for the onset mechanism. *Journal of Geophysical Research (Space Physics)* **44**, 2078–2087.

Kalmoni, N. M. E., Rae, I. J., Watt, C. E. J., Murphy, K. R., Forsyth, C. & Owen, C. J. 2015 Statistical characterization of the growth and spatial scales of the substorm onset arc. *Journal of Geophysical Research (Space Physics)* **120**, 8503–8516.

Kalmoni, N. M. E., Rae, I. J., Watt, C. E. J., Murphy, K. R., Samara, M., Michell, R. G., Grubbs, G. & Forsyth, C. 2018 A diagnosis of the plasma waves responsible for the explosive energy release of substorm onset. *Nature Communications* **9**, 4806.

Kalmykov, N. N. & Kulikov, G. V., R. T. M. 2007 *Galactic cosmic rays*, , vol. 1. Moscow: KDU.

Katsiaris, G. A. & Psillakis, Z. M. 1986 Allowed regions for the motion of charged particles in superposed dipole and uniform magnetic fields. *J. Astrophys. and Space Sci.* **126**, 69–87.

Kida, S. & Kitauchi, H. 1998 Chaotic reversals of dipole moment of thermally driven magnetic field in a rotating spherical shell. *Journal of the Physical Society of Japan* **67** (8), 2950–2951.

Kirkby, J. 2007 Cosmic Rays and Climate. *Surveys in Geophysics* **28** (5-6), 333–375.

Kirkby, M. J., Gallart, F., Kjeldsen, T. R., Irvine, B. J., Froebrich, J., Lo Porto, A., de Girolamo, A. & Mirage Team 2011 Classifying low flow hydrological regimes at a regional scale. *Hydrology and Earth System Sciences* **15** (12), 3741–3750.

Kitiashvili, I. & Kosovichev, A. G. 2008 Application of Data Assimilation Method for Predicting Solar Cycles. *Astrophysical Journal Letters* **688** (1), L49.

Kitiashvili, I. N. & Kosovichev, A. G. 2009 Nonlinear dynamical modeling of solar cycles using dynamo formulation with turbulent magnetic helicity. *Geophysical and Astrophysical Fluid Dynamics* **103** (1), 53–68.

Kivelson, M. G. & Russell, C. T. 1995 *Introduction to space physics*. Cambridge University Press.

Korte, M. & Mandea, M. 2008 Magnetic poles and dipole tilt variation over the past decades to millennia. *Earth Planets and Space* **60**, 937–948.

Lammer, H., Lichtenegger, H. I. M., Kulikov, Y. N., Griessmeier, J.-M., Terada, N., Erkaev, N. V., Biernat, H. K., Khodachenko, M. L., Ribas, I. & Penz, T. 2007 Coronal Mass Ejection (CME) Activity of Low Mass M Stars as An Important Factor for The Habitability of Terrestrial Exoplanets. II. CME-Induced Ion Pick Up of Earth-like Exoplanets in Close-In Habitable Zones. *Astrobiology* **7** (1), 185–207.

Lammer, H., Zerkle, A. L., Gebauer, S., Tosi, N., Noack, L., Scherf, M., Pilat-Lohinger, E., Güdel, M., Grenfell, J. L., Godolt, M. & Nikolaou, A. 2018 Origin and evolution of the atmospheres of early venus, earth and mars. *The Astronomy and Astrophysics Review* **26**.

Le, G., Blanco-Cano, X., Russell, C. T., Zhou, X.-W., Mozer, F., Trattner, K. J., Fuselier, S. A. & Anderson, B. J. 2001 Electromagnetic ion cyclotron waves in the high-altitude cusp: Polar observations. *J. Geophys. Res.* **106** (A11), 19067–19079.

Le Contel, O., Pellat, R. & Roux, A. 2000 Self-consistent quasi-static parallel electric field associated with substorm growth phase. *Journal of Geophysical Research: Space Physics* **105** (A6), 12945–12954, arXiv: https://agupubs.onlinelibrary.wiley.com/doi/pdf/10.1029/1999JA900499.

Lemaire, J. F. 2003 The effect of a southward interplanetary magnetic field on stormers allowed regions. *Space Res.* **31** (5), 1131–1153.

Lemaire, J. F. & Gringauz, K. I. 1998 *The Earth's Plasmasphere*. New York: Cambridge Univ. Press.

Lemaire, J. F. & Singer, S. F. 2012 *What Happens When the Geomagnetic Field Reverses?*. (Washington, DC: American Geophysical Union.

Lemaître, G. & Vallarta, M. S. 1933 On compton's latitude effect of cosmic radiation. *Phys. Rev.* **43** (2), 87–91.

Lembege, B. & Pellat, R. 1982 Stability of a thick two-dimensional quasineutral sheet. *Physics of Fluids* **25**, 1995–2004.

Levy, R. H., Petschek, H. E. & L., S. G. 1964 Aerodynamic aspects of magnetospheric flow. *AIAA J.* **2**, 2065.

Liou, K., Meng, C.-I., Lui, A. T. Y., Newell, P. T. & Wing, S. 2002 Magnetic dipolarization with substorm expansion onset. *Journal of Geophysical Research (Space Physics)* **107** (A7), 1131.

Longair, M. S. 1981 *High energy astrophysics*. New York: Cambridge University Press.

Lui, A. T. Y. 1991 A synthesis of magnetospheric substorm models. *Journal of Geophysical Research (Space Physics)* **96** (A2), 1849–1856.

Lui, A. T. Y. 1996 Current disruption in the Earths magnetosphere: Observations and models. *Journal of Geophysical Research (Space Physics)* **101** (A6), 13,067–13,088.

Lui, A. T. Y. 2004 Potential plasma instabilities for substorm expansion onsets. *Space Science Reviews* **113**, 127–206.

Lui, A. T. Y. 2016 Cross-field current instability for auroral bead formation in breakup arcs. *Journal of Geophysical Research (Space Physics)* **43**, 6087–6095.

Lui, A. T. Y. & Murphree, J. S. 1998 A substorm model with onset location tied to an auroral arc. *Geophys. Res. Lett.* **25**, 1269–1272.

Lundin, R. & Dubinin, E. M. 1992 Phobos-2 results on the ionospheric plasma escape from Mars. *Advances in Space Research* **12**, 255–263.

McCormac, B. M. & Evans, J. E. 1969 Consequences of Very Small Planetary Magnetic Moments. *Nature* **223** (5212), 1255.

McPherron, R. L. 1970 Growth phase of magnetospheric substorms. *Journal of Geophysical Research (1896-1977)* **75** (28), 5592–5599.

Melott, A. L., Thomas, B. C., Hogan, D. P., Ejzak, L. M. & Jackman, C. H. 2005 Climatic and biogeochemical effects of a galactic gamma ray burst. *Geophys. Res. Lett.* **32** (14), L14808.

Merrill, R. T. & McFadden, P. L. 1999 Geomagnetic polarity transitions. *Reviews of Geophysics* **37** (2), 201–226.

Mikhailovskii, A. B. 1998 *Instabilities in a Confined Plasma*. IOP.

Miyake, W., Mukai, T. & Kaya, N. 2000 Interplanetary magnetic field control of dayside ion conics. *J. Geophys. Res.* **105** (A10), 23339–23344.

Miyashita, Y., Angelopoulos, V., Fukui, K. & Machida, S. 2018 A case study of near-Earth magnetotail conditions at substorm and pseudosubstorm onsets. *Journal of Geophysical Research (Space Physics)* **45**, 6353–6361.

Miyashita, Y., Machida, S., Ieda, A., Ieda, D., Kamide, Y., Nosé, M., Liou, K., Mukai, T., Christon, S. P., Russell, C. T., Shinohara, I. & Saito, Y. 2010 Pressure changes associated with substorm depolarization in the near-Earth plasma sheet. *Journal of Geophysical Research (Space Physics)* **115**, A12239.

Morley, L. W. & Larochelle, A. 1964 Paleomagnetism as a means of dating geological events. *Geochronology in Canada* **8**, 39–51.

Nefedov, S. N. & Sokolov, D. D. 2010 Nonlinear low-mode parker dynamo model. *Astron. Zh.* **87**, 278–285.

Nilsson, H., Barghouthi, I. A., Slapak, R., Eriksson, I. A. & Andrè, M. 2012 Hot and cold ion outflow: Spatial distribution of ion heating. *Journal of Geophysical Research (Space Physics)* **117**, 11201–.

Nymmik, P. A. 1993 Model of particle fluxes and averaged energy spectra of solar cosmic rays. *Kosmicheskie Issledovaniia* **31**, 51.

Ogawa, Y., Fujii, R., Buchert, S., Nozawa, S., Watanabe, S. & Van Eyken, A. P. 2000 Simultaneous eiscat svalbard and vhf radar observations of ion upflows at different aspect angles. *Geophys. Res. Lett.* **27**, 81 – 84.

Olson, P. & Amit, H. 2006 Changes in Earth's dipole. *Naturwissenschaften* **93** (11), 519–542.

Olson, P., Driscoll, P. & Amit, H. 2009 Dipole collapse and reversal precursors in a numerical dynamo. *Phys. Earth Planet. Inter.* **173**, 121–140.

Onishchenko, O. G., Pokhotelov, O. A., Krasnoselskikh, V. V. & Shatalov, S. I. 2009 Drift-alfvn waves in space plasmas ; theory and mode identification. *Annales Geophysicae* **27** (2), 639–644.

Opdyke, N. D. 1972 Paleomagnetism of Deep-Sea Cores. *Reviews of Geophysics and Space Physics* **10**, 213.

Parker, E. N. 1955 Hydromagnetic Dynamo Models. *Astrophysical Journal* **122**, 293.

Pellat, R. 1990 A new approach to magnetic reconnection - Magnetic substorms and stellar winds. *Academie des Sciences Paris Comptes Rendus Serie B Sciences Physiques* **311**, 45–49.

Pellat, R., Hurricane, O. A. & Coroniti, F. V. 1994 Multipole stability revisited. *Physics of Plasmas* **1**, 3502–3504.

Pérez-de-Tejada, H. 1998 Momentum transport in the solar wind erosion of the Mars ionosphere. *Journal of Geophysical Research: Planets* **103**, 31499–31508.

Perraut, S., Le Contel, O., Roux, A., Parks, G., Chua, D. & Hoshino, M. 2003 Substorm expansion phase: Observations from Geotail, Polar and IMAGE network. *Journal of Geophysical Research (Space Physics)* **108** (A4), 1159.

Pollock, C. J., Chandler, M. O., Moore, T. E., Waite Jr., J. H., Chappell, C. R. & Gurnett, D. A. 1990 A survey of upwelling ion event characteristics. *J. Geophys. Res.* **95** (A11), 18969–18980.

Ponert, J. & Príhoda, P. 2009 Biological Evolution on the Earth Influenced by Astronomical Objects: Especially Gamma-ray Sources. In *Bioastronomy 2007: Molecules, Microbes and Extraterrestrial Life ASP Conference Series, Vol. 420, proceedings of a workshop held 16-20 July 2007 in San Juan, Puerto Rico. Edited by Karen J. Meech, Jaqueline V. Keane, Michael J. Mumma, Janet L. Siefert, and Dan J. Werthimer. San Francisco: Astronomical Society of the Pacific, 2009., p.259* (ed. K. J. Meech, J. V. Keane, M. J. Mumma, J. L. Siefert & D. J. Werthimer), *Astronomical Society of the Pacific Conference Series*, vol. 420, p. 259.

Popova, H. 2013 A double magnetic solar cycle and dynamical systems. *Magnetohydrodynamics* **49**, 59–68.

Popova, H. P. 2016*a* Current results on the asymptotics of dynamo models. *Physics Uspekhi* **59** (6), 513–530.

Popova, H. P. 2016*b* Dynamical systems for modeling the evolution of the magnetic field of stars and earth. *J. of Physics: Conference Series* **681**, 012021.

Rae, I. J., Mann, I. R., Angelopoulos, V., Murphy, K. R., Milling, D. K., Kale, A., Frey, H. U., Rostoker, G., Russell, C. T., Watt, C. E. J., Engebretson, M. J., Moldwin, M. B., Mende, S. B., Singer, H. J. & Donovan, E. F. 2009 Near-Earth initiation of a terrestrial substorm. *Journal of Geophysical Research (Space Physics)* **114**, A07220.

Roux, A., Perraut, S., Robert, P., Morane, A., Pedersen, A., Korth, A., Kremser, G., Aparicio, B., Rodgers, D. & Pellinen, R. 1991 Plasma sheet instability related to the westward traveling surge. *Journal of Geophysical Research (Space Physics)* **96**, 17697.

Ruzmaikin, A. A. 1981 The solar cycle as a strange attractor. *Comments on Astrophysics* **9** (2), 85–93.

Sagan, C. 1965 Is the early evolution of life related to the development of the earth's core? *Nature* **206**, 448.

Sagnotti, L., Scardia, G., Giaccio, B., Liddicoat, J., Renne, P. & Sprain, C. 2014 Extremely rapid directional change during matuyama-brunhes geomagnetic polarity reversal, geophys. *Geophysical Journal International* **199**, 1110–1124.

Saito, T. & Akasofu, S.-I. 1987 On the resersal of the dipolar field of the sun and its possible implication for the reversal of the earths field. *J. Geophys. Res.* **92**, 1255–1259.

Saito, T., Sakurai, T. & Yumoto, K. 1978 The earth's palaeomagnetosphere as the third type of planetary magnetosphere. *Planetary and Space Science* **26**, 413–422.

Sato, T. 2015 Analytical Model for Estimating Terrestrial Cosmic Ray Fluxes Nearly Anytime and Anywhere in the World: Extension of PARMA/EXPACS. *PLoS ONE* **10** (12), e0144679.

Sato, T., Yasuda, H., Niita, K., Endo, A. & Sihver, L. 2008 Development of PARMA: PHITS-based Analytical Radiation Model in the Atmosphere. *Radiation Research* **170** (2), 244–259.

Schindler, K. 1975 Plasma and fields in the magnetospheric tail. *Space Science Reviews* **17**, 589–614.

Schulz, M. & Paulikas, G. A. 1990 Planetary magnetic fields: A comparative view. *Adv. Space Res.* **10** (1), 55–64.

Seyfert, C. K. 1987 *Continental drift, paleomagnetic evidence*, pp. 62–81. Springer Berlin Heidelberg.

Shabansky, V. P. 1971 Some processes in the magnetosphere. *Space Sci. Rev.* **12** (3), 299–418.

Shebalin, J. V. 2004 Stormer regions for axisymmetric magnetic multipole fields. *Physics of Plasmas* **11**, 3472.

Sheyko, A., Finlay, C. & Jackson, A. 2016 Magnetic reversals from planetary dynamo waves. *Nature* **539** (7630), 551–554.

Shiokawa, K., Baumjohann, W. & Haerendel, G. 1997 Braking of high-speed flows in the near-Earth tail. *Geophys. Res. Lett.* **24**, 1179–1182.

Shiokawa, K., Haerendel, G. & Baumjohann, W. 1998 Azimuthal pressure gradient as driving force of substorm currents. *Geophys. Res. Lett.* **25**, 959–962.

Simpson, J. F. 1966 Evolutionary Pulsations and Geomagnetic POLARITY1. *Geological Society of America Bulletin* **77** (2), 197.

Sinnhuber, B.-M., Weber, M., Amankwah, A. & Burrows, J. P. 2003 Total ozone during the unusual Antarctic winter of 2002. *Geophys. Res. Lett.* **30** (11), 1580.

Siscoe, G. L. & Chen, C.-K. 1975 The paleomagnetosphere. *Journal of Geophysical Research* **80** (34), 4675–4680.

Slapak, R., Hamrin, M., Pitkänen, T., Yamauchi, M., Nilsson, H., Karlsson, T. & Schillings, A. 2017 Quantification of the total ion transport in the near-earth plasma sheet. *Annales Geophysicae* **35** (4), 869–877.

Smart, D. F., Shea, M. A. & Flückiger, E. O. 2000 Magnetospheric models and trajectory computations. *Space Sci. Rev.* **93**, 305–333.

Sobko, G. S., Zadkov, V. N., Sokoloff, D. D. & Trukhin, V. I. 2012 Geomagnetic reversals in a simple geodynamo model. *Geomagnetism and Aeronomy* **52** (2), 254–260.

Sokoloff, D., Nefedov, S., Ermash, A. & Lamzin, S. 2008 Dynamo model with a small number of modes and magnetic activity of t tauri stars. *Astronomy Letters* **34**, 761–771.

Soler-Arechalde, A., Goguitchaichvili, A., Carrancho, Á., Sedov, S., Caballero-Mirand a, C., Ortega, B., Solís, B., Morales Contreras, J., Urrutia-Fucugauchi, J. & Bautista, F. 2015 A detailed paleomagnetic and rock-magnetic investigation of the Matuyama-Bruhnes geomagnetic reversal recorded in tephra-paleosol sequence of Tlaxcala(Central Mexico). *Frontiers in Earth Science* **3**, 11.

Stadelmann, A., Vogt, J., Glassmeier, K.-H., Kallenrode, M.-B. & Voigt, G.-H. 2010 Cosmic ray and solar energetic particle flux in paleomagnetospheres. *Earth Planets Space* **62** (5), 333–345.

Stern, D. P. 1973 A Study of the Electric Field in an Open Magnetospheric Model. *Journal of Geophysical Research* **78** (31), 7292–7305.

Störmer, C. 1907 Sur les trajectoires des corpuscules électrisés dans l'espace sous l'action du magnétisme terrestre avec application aux aurores boréales. *Arch. Sci. Phys. Nat.* **24**, 5–18, 113–158, 221–247, 317–364.

Störmer, C. 1930 Twenty-five years' work on the polar aurora. *Terr. Magn. Atmos. Electr.* **35**, 193–208.

Störmer, C. 1955 *The polar Aurora*. Oxford: Clarendon Press.

Strangeway, R. J., Ergun, R. E., Su, Y.-J., Carlson, C. W. & Elphic, R. C. 2005 Factors controlling ionospheric outflows as observed at intermediate altitudes. *Journal of Geophysical Research (Space Physics)* **110**, A03221–.

Strangeway, R. J., Russell, C. T., Luhmann, J. G., Moore, T. E., Foster, J. C., Barabash, S. V. & Nilsson, H. 2010 Does a Planetary-Scale Magnetic Field Enhance or Inhibit Ionospheric Plasma Outflows? *AGU Fall Meeting Abstracts* pp. SM33B–1893.

Svensmark, H. & Friis-Christensen, E. 1997 Variation of cosmic ray flux and global cloud coverage-a missing link in solar-climate relationships. *Journal of Atmospheric and Solar-Terrestrial Physics* **59**, 1225–1232.

Thébault, E., Finlay, C. & Toh, H. 2015*a* Special issue "International Geomagnetic Reference Field—the twelfth generation". *Earth, Planets, and Space* **67**, 158.

Thébault, E., Finlay, C. C., Alken, P., Beggan, C. D., Canet, E., Chulliat, A., Langlais, B., Lesur, V., Lowes, F. J., Manoj, C., Rother, M. & Schachtschneider, R. 2015*b* Evaluation of candidate geomagnetic field models for IGRF-12. *Earth, Planets, and Space* **67**, 112.

Thebault, E., Finlay, C. C. & Toh, H. 2015 International geomagnetic reference field: the 12th generation. *Earth, Planets and Space* **67**, 158.

Tian, F., Chassefière, E., Leblanc, F. & Brain, D. A. 2013 *Atmosphere escape and climate evolution of terrestrial planets. In Comparative Climatology of Terrestrial Planets*. Univ. of Arizona, Tucson.

Tsyganenko, N. A. 1995 Modeling the Earths magnetospheric magnetic field confined within a realistic magnetopause. *Journal of Geophysical Research (Space Physics)* **100** (A4), 5599–5612.

Tur, A., Fruit, G., Louarn, P. & Yanovsky, V. 2014 Kinetic theory of the electron bounce instability in two dimensional current sheets-Full electromagnetic treatment. *Physics of Plasmas* **21** (3), 032113.

Tur, A., Louarn, P. & Yanovsky, V. 2010 Kinetic theory of electrostatic "bounce" modes in two-dimensional current sheets. *Physics of Plasmas* **17** (10), 102905.

Uffen, R. J. 1963 Influence of the Earth's Core on the Origin and Evolution of Life. *Nature* **198** (4876), 143–144.

Urban, E. W. 1966 Critical stormer conditions in quadrupole and double ring-current fields. *J. of Math. Physics* **6**, 1966–1975.

Valet, J. & Meynadier, L. 1993 Geomagnetic field intensity and reversals during the past four million years. *Nature* **366**, 234–238.

Vallarta, M. S. 1938 An outline of the theory of the allowed cone of cosmic radiation. *Appl. Math. Series* **3**.

Van Allen, J. A., McIlwain, C. E. & Ludwig, G. I.-I. 1959 Radiation observations with satellite 1958. *J. Geophys. Res.* **64** (3), 271–285.

Vernov, S. N., Grigorov, N. L., Logachev, Y. I. & Chudakov, A. E. 1958 Measurement of cosmic radiation on the sputnik. *Dokl. Akad. Nauk SSSR* **120** (6), 1231–1233.

Vine, F. & Matthews, D. 1963 Magnetic anomalies over oceanic ridges. *Nature* **199**, 947–949.

Vogt, J. & Glassmeier, K. H. 2000 On the location of trapped particle populations in quadrupole magnetospheres. *J. Geophys. res.* **105** (A6), 13,063–13,071.

Vogt, J., Zieger, B., Glassmeier, K.-H., Stadelmann, A., Kallenrode, M.-B., Sinnhuber, M. & Winkler, H. 2007 Energetic particles in the paleomagnetosphere: Reduced dipole configurations and quadrupolar contributions. *Journal of Geophysical Research: Space Physics* **112** (A6), A06216.

Vogt, J., Zieger, B., Stadelmann, A., Glassmeier, K.-H., Gombosi, T. I., Hansen, K. C. & Ridley, A. J. 2004 Mhd simulations of quadrupolar paleomagnetospheres. *Journal of Geophysical Research* **109**, A12221.

Voigt, G.-H. 1981 A mathematical magnetospheric field model with independent physical parameters. *Planetary and Space Science* **29** (1), 1–20.

Voigt, G.-H. 1995 *Handbook of Atmospheric Electrodynamics: Volume II*. CRC Press.

Watkins, N. D. & Goodell, H. G. 1967 Geomagnetic Polarity Change and Faunal Extinction in the Southern Ocean. *Science* **156** (3778), 1083–1087.

Watt, C. E. J. & Rankin, R. 2009 Electron Trapping in Shear Alfvén Waves that Power the Aurora. *Physical Review Letters* **102** (4), 045002.

Wei, Y., Pu, Z., Zong, Q., Wan, W., Ren, Z., Fraenz, M., Dubinin, E., Tian, F., Shi, Q. & Fu, S. 2014 Oxygen escape from the earth during geomagnetic reversals: Implications to mass extinction. *Earth and Planetary Science Letters* **394**, 94–98.

Weiland, J. 2012 *Stability and Transport in Magnetic Confinement Systems*, , vol. 71. Springer Science+Business Media New York.

Welling, D. T., Andrè, M., Dandouras, I., Delcourt, D., Fazakerley, A., Fontaine, D., Foster, J., Ilie, R., Kistler, L., Lee, J. H., Liemohn, M. W., Slavin, J. A., Wang, C.-P., Wiltberger, M. & Yau, A. 2015 The earth: Plasma sources, losses, and transport processes. *Space Science Reviews* **192** (1-4), 145–208.

Williams, I. & Fuller, M. 1981 Zonal harmonic models of reversal transition fields. *J. Geophys. Res.* **86**, 11657–11665.

Willis, D. M. & Young 1987 Equation for the field lines of an axisymmetric magnetic multipole. *Geophys. J. Royal Astron. Soc.* **89**, 1011–1022.

Winkler, H., Sinnhuber, M., Notholt, J., Kallenrode, M.-B., Steinhilber, F., Vogt, J., Zieger, B., Glassmeier, K.-H. & Stadelmann, A. 2008 Modeling impacts of geomagnetic field variations on middle atmospheric ozone responses to solar proton events on long timescales. *Journal of Geophysical Research (Atmospheres)* **113** (D2), D02302.

Yau, A. W. & Andrè, M. 1997 Sources of ion outflow in the high latitude ionosphere. *Space Science Reviews* **80** (1-2), 1–25.

Zarrouk, N. & Bennaceur, R. 2009 Extrapolating cosmic ray variations and impacts on life: Morlet wavelet analysis. *International Journal of Astrobiology* **8** (3), 169–174.

Zelenyi, L. M., Petrukovich, A. A., Budnick, E. Y., Romanov, S. A., Sergeev, V. A., Mukai, T., Yamamoto, T., Kokubun, S., Shiokawa, K., Deehr, C. S., Bỳchner, J. & Sandahl, I. 1998 Substorm onset models and observations. In *Substorms-4*, , vol. 238, p. 327. Kluwer Academic Publishers, Astrophysics and Space Science library.

Appendix A

For Electromagnetic Drift instability theory

A.1 Curvilinear coordinate system

The natural field-aligned coordinates system (ψ, y, χ) defined by

$$\vec{e}_\psi = [\vec{e}_y \times \vec{e}_\chi], \quad \vec{e}_y = \frac{\vec{J}_{eq}}{J_{eq}}, \quad \vec{e}_\chi = \frac{\vec{B}_{eq}}{B_{eq}}, \tag{A.1}$$

where $B_{eq}(\chi, \psi)$ and $J_{eq}(y)$ are the magnetic field and electric current at equilibrium. According to Tur *et al.* (2014), the scale factors in the curvilinear system are

$$h_\psi = \frac{1}{B_{eq}}, \quad h_y = 1, \quad h_\chi = JB_{eq} = \frac{1}{B_{eq}} \exp\left[-\mu_0 \int \frac{J_{eq}}{B_{eq}^2} \mathrm{d}\psi\right], \tag{A.2}$$

where J denotes the Jacobian of the coordinate transformation. The elementary length along the field line is given by

$$\mathrm{d}\ell = h_\chi \mathrm{d}\chi. \tag{A.3}$$

The nabla operator writes

$$\nabla = B_{eq} \frac{\partial}{\partial \psi} \vec{e}_\psi + \frac{\partial}{\partial y} \vec{e}_y + \frac{1}{JB_{eq}} \frac{\partial}{\partial \chi} \vec{e}_\chi. \tag{A.4}$$

The resolution of the parallel Ampere's law requires to compute the parallel component of the Laplacian of $\vec{a}_1$ using the algebraic formula $\Delta \vec{a} = \nabla(\nabla \cdot \vec{a}) - [\nabla \times [\nabla \times \vec{a}]]$ (see also eq. (38) of Tur *et al.* (2014))

$$[\Delta\vec{a}_1]_\parallel = -k_\perp^2\tilde{a}_\parallel + \frac{\mathrm{d}^2\tilde{a}_\parallel}{\mathrm{d}\ell^2} - \frac{\mathrm{d}}{\mathrm{d}\ell}\left(\frac{\mathrm{d}\ln B_{eq}}{\mathrm{d}\ell}\tilde{a}_\parallel\right). \tag{A.5}$$

Taking the Fourier component along the field line to get $j_\parallel$ also given by (3.42), the Ampere's law for the parallel current in the curvilinear system is

$$\mu_0 j_\parallel = \left[k_\perp^2 + \frac{\pi^2}{\ell_0^2}(1-\beta_0)\right]\alpha_1, \tag{A.6}$$

with coefficient $\beta_0 = -\frac{2}{\pi}\int_0^{\ell_0}\frac{\mathrm{d}\ln B_{eq}}{\mathrm{d}\ell}\sin\left(\pi\frac{\ell}{\ell_0}\right)\cos\left(\pi\frac{\ell}{\ell_0}\right)\mathrm{d}\ell$ is of the order of unity. This last expression for the laplacian may be simplified in our analysis since the wavelength is assumed to be of the order of the ion Larmor radius and $k_\perp \sim \pi/\rho_{Li} \sim 1200\pi/\ell_0$ given the parameters in table 3.1, thus

$$\mu_0 j_\parallel = k_\perp^2\alpha_1. \tag{A.7}$$

A.2 Expressions of some functions appearing in (3.56-3.59)

Introducing the variable ζ written in the dimensionless quantities x and $\epsilon = B_0/B_1$:

$$\zeta = \frac{\pi}{2}\sqrt{\frac{E-\mu\,B_0}{\mu\,B_1}} = \frac{\pi}{2}\sqrt{\frac{\pi^2}{x^2}-\epsilon},$$

the functions $\Gamma_{0,\ldots,4}(x)$ in the integrals (3.56-3.59) write

$$\begin{aligned}
\Gamma_0 &= \left(\frac{1}{2}J_0^2(\zeta) + J_2^2(\zeta)\right)\left[\frac{\pi^2}{x^2}+\epsilon\right] - J_0(\zeta)\,J_2(\zeta)\,\left[\frac{\pi^2}{x^2}-\epsilon\right]\\
\Gamma_1 &= -J_2^2(\zeta)\left[\frac{\pi^2}{x^2}+\epsilon\right] + \frac{1}{2}J_0(\zeta)\,J_2(\zeta)\left[\frac{\pi^2}{x^2}-\epsilon\right]\\
\Gamma_2 &= J_1(\zeta)\,J_2(\zeta)\left[\frac{\pi^2}{x^2}+\epsilon\right] - \frac{1}{2}J_0(\zeta)\,J_1(\zeta)\,\left[\frac{\pi^2}{x^2}-\epsilon\right]\\
\Gamma_3 &= \frac{1}{2}J_1(\zeta)\,J_2(\zeta)\left[\frac{\pi^2}{x^2}+\epsilon\right]\\
\Gamma_4 &= \frac{1}{2}J_1^2(\zeta)\,\left[\frac{\pi^2}{x^2}+\epsilon\right]
\end{aligned}$$

A.3 Drift Alfvén Waves

Consider a plasma slab with a density gradient and straight magnetic field lines. Electron motion along the magnetic field lines has a stabilizing influence on the modes, but is less efficient for cancelling space charge for small $k_\parallel$, i .e. we assume $k_\parallel \ll k_\perp$.

The parallel electron motion is quite different for different modes. We may here separate two classes — drift waves ($E_\parallel \neq 0$) and Magnetohydrodynamic (MHD) waves ($E_\parallel \approx 0$). In the first case the electrons are essentially free to cancel space charge by moving along the magnetic field while in the second case the parallel electron motion is strongly impeded either by a very small $k_\parallel$ or by electromagnetic induction. As long as the electrons are free to move along B_0 to cancel space charge, the drift wave is stable. There are, however, several effects that may limit the mobility of the electrons, e. g. electron ion collisions, Landau damping, electron inertia or inductance (Weiland, 2012).

A characteristic feature of drift waves is that their parallel phase velocity is between the ion and electron thermal velocities $V_{Ti} \leq \omega/k_\parallel \ll V_{Te}$. If a perturbations varying sinusoidally in time and along y, we obtain the simpliest possible dispersion relation for drift waves $\omega = k_\perp u_e$.

Hasegawa (1975) obtain the dispersion relation for drift Alfvén waves in the following form:

$$\begin{vmatrix} \frac{T_e}{T_i}\frac{k_\parallel}{k_\perp}\left(1-\frac{\omega_i^*}{\omega}\right)\left[1-e^{-\lambda_i}I_0(\lambda_i)\right] & \frac{m_e}{m_i}\frac{k_\parallel^2 v_{Te}^2}{\omega^2}\left(1-\frac{\omega_i^*}{\omega}\right)e^{-\lambda_i}I_0(\lambda_i)-\left(1-\frac{\omega_e^*}{\omega}\right) \\ -\frac{k_\perp k_\parallel c_A^2}{\omega_{ci}^2}\frac{m_e}{m_i} & \frac{m_e}{m_i}\left(1-\frac{\omega_i^*}{\omega}\right)e^{-\lambda_i}I_0(\lambda_i)-\left(1-\frac{\omega_e^*}{\omega}\right)\frac{\omega^2}{k_\parallel^2 v_{Te}^2}+\frac{k_\perp^2 c_A^2}{\omega_{ci}^2}\frac{m_e}{m_i} \end{vmatrix} = 0 \quad \text{(A.8)}$$

If $k_\perp \rho_{Li} \ll 1$ the ion contributions to $e^{-\lambda_i}I_0(\lambda_i)$ becomes negligible and the resultant dispersion relation simplifies to

$$\omega^2 - \omega\omega_i^* - k_\parallel^2 c_A^2 = \frac{T_e}{T_i}k_\perp^2\rho_{Li}^2 k_\parallel^2 c_A^2 \frac{\omega-\omega_i^*}{\omega-\omega_e^*}, \quad \text{(A.9)}$$

where $\rho_{Li} = T_i/(m_i\omega_{ci})$ is the ion Larmor radius, $c_A = c\omega_{ci}/\omega_{pi}$ is Alfvén speed. Assuming $k_y^2\rho_i^2 \ll 1$ we realise that (4.46/3.17) splits into two branches the electric drift wave branch with $\omega = \omega_e^* = k_\perp u_e$ and the electromagnetic drift wave branch or drift Alfvén branch.

A.4 Addition to Auroral Development

At 04:55 UT, the TH-A, TH-D and TH-E spacecrafts are located at (-9.23, 0.86, -3.01), (-10.87, 0.46, -3.5) R_E and (-10.21, 1.38, -3.22) R_E in the GSM coordinates, respectively. The midpoint coordinates between TH-A and TH-D spacecrafts is (-10.05, 0.66, -3.26). The separation distance between TH-E and midpoint is $(\triangle x, \triangle y, \triangle z) = (0.16, 0.72, 0.04)$ R_E, and the azimuthal separation distance is $\triangle R \sim 0.72$ R_E. The footprints of TH-A, TH-D and TH-E spacecrafts are located at (281° LON, 55.61° LAT) (282.9° LON, 56.21° LAT) (midpoint is 281.95° LON, 55.91° LAT) and (279.7° LON, 55.92° LAT), respectively. The TH-E and midpoint between TH-A and TH-D spacecrafts are roughly on the substorm initiation arc at 04:55 UT, and their separation distance is ~140.2 km. Assuming that the perpendicular wavelength scales as the width of the magnetic flux tube linking the ionosphere and magnetosphere, the ratio between ionospheric and magnetospheric perpendicular wavenumbers are $k_{Space} = 140.2/(0.74\ R_E)\ k_{Ion} \approx 0.03\ k_{Ion}$.

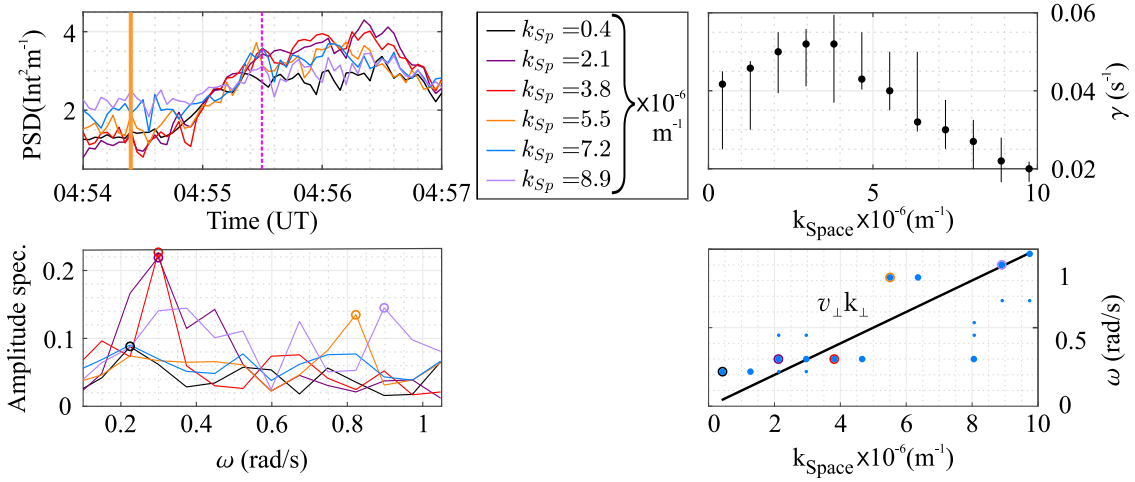

Figure A.1: **Top Left:** The log of the power from PSD for a single wave numbers k_{Space} against time to determine exponential growth rate γ. **Top Right:** Growth rate as a function of azimuthal wave number. **Below:** The observational dispersion relation calculated using Fast Fourier transform the time signals (04:55:30 – 04:56:45 UT) for each wavenumber k_{Space}.

The resulting power spectral density (PSD) can be used to decompose the signal into individual perpendicular wavenumbers, k_{Space}. Figure A.1 (top left) shows exponentially growing modes (with duration longer than 30 s) for each k_{Space}. We use a linear fitting method (Kalmoni *et al.*, 2015) to determine growth rate, γ. Figure A.1 (top right) shows γ as a function of k_{Space}, which peak at $\omega_r \sim 2 \cdot \pi/13\ s = 0.48$ rad/s and $k_{Space} = 3.8 \times 10^{-6}$/m or $\lambda_\perp = 1650$ km (in the ionosphere $k_{Ion} = 1.3 \times 10^{-4}$/m, $\lambda_{Ion} = 49.4$ km). For each individual wavenumber, a temporal frequency analysis (Fast Fourier transform the time

signals in Fig. A.1 (below right)) is performed to measure the real frequency, ω_r. Fig. A.1 (below right) summarizes the analysis results to create the observational dispersion relation. The relationship between ω_r and k_{Space} is linearly approximated with the magnetospheric phase speed $v_\perp \approx 127$ km/s corresponding the diamagnetic drift velocity $u_i = 130$ km/s for the ion density gradient $\nabla_x \ln n_i = 1/R_E$.

Appendix B

Area of open field line regions (polar caps and equatorial belt)

The dipole field line, the distance to which at the equator ($\theta = 90°$) is equal to $r = R_s$ (i. e. subsolar magnetopause standoff distance), crosses the exobase $r = r_{exo}$ at latitude defined as $1 = L\sin^2\theta$, where the parameter $L = R_s/r_{exo}$, whence $\theta_{exo} = \arcsin\sqrt{1/L}$. In the dipole field, the area of two polar caps at the exobase is

$$S_{dip} = 4\pi r_{exo}^2 \int_0^{\theta_{exo}} \sin\theta d\theta = 4\pi r_{exo}^2 \left(1 - \sqrt{1 - 1/L}\right) = 2\pi r_{exo}^2 \Theta_{dip}. \tag{B.1}$$

The quadrupole magnetic line equation that satisfies the condition $r = R_s$ at metastable latitudes ($\theta = 63.4°,\ 116.6°$) is expressed as $r^2 = R_s^2 \sin^2\theta\cos\theta/(0.8\sqrt{0.2})$. The latitudes of the intersection of exobase $r = r_{exo}$ and field lines are equal to $\theta_{1,2}^{exo} = \arccos(2/\sqrt{3}\cos\phi_{1,2})$,

$$\phi_{1,2} = \frac{1}{3}\arctan\sqrt{\frac{4}{27}\frac{L^4}{0.8^2 0.2} - 1} \mp \frac{\pi}{3}. \tag{B.2}$$

In the quadrupole field, the area of two polar caps and the equatorial belt at the exobase is

$$S_{quad} = 4\pi r_{exo}^2 \left(\int_0^{\theta_1^{exo}} \sin\theta d\theta + \int_{\theta_2^{exo}}^{\pi/2} \sin\theta d\theta\right) = \\ = 4\pi r_{exo}^2 \left(1 + \frac{2}{\sqrt{3}}\left(\cos\phi_2 - \cos\phi_1\right)\right) = 2\pi r_{exo}^2 \Theta_{quad}. \tag{B.3}$$

We did not take into account the system of currents, compressing the dayside magnetosphere (whose perturbed field lines are shown in Fig. 7.1) and pulling out its tail part, because it leads to an underestimation of the polar cap area (Gunell *et al.*, 2018), which is

actually shifted to the nightside and not uniformly compressed. We trace an unperturbed field line from the subsolar magnetopause down to the exobase and approximate the polar cap area by a circle centred on the pole at the exobase altitude.

Appendix C

Publications

- TSAREVA, O., FRUIT, G., LOUARN, P. & TUR, A. 2019 Electromagnetic drift instability in a two-dimensional magnetotail — the addition of bouncing electrons. *Journal of Plasma Physics* **85** (2), 905850212. DOI: 10.1017/S002237781900028X

- TSAREVA, O., FRUIT, G., LOUARN, P., JACQUEY, C. & TUR, A. 2020 Electromagnetic drift waves at substorm onset: Theory and Observations. *Journal of Geophysical Research (Space Physics)* **125**, e2020JA028063. DOI: 10.1029/2020JA028063

- TSAREVA, O. O., ZELENYI, L. M., MALOVA, H. V., PODLOZKO, M. V., POPOVA, E. P. & POPOV, V. YU. 2018 What expects humankind during the inversion of the Earth's magnetic field: threats imagined and real. *Physics-Uspekhi* **61** (2), 191-202. DOI: 10.3367/UFNe.2017.07.038190

- TSAREVA, O. O. 2019 Generalization of Störmer Theory for an Axisymmetric Superposition of Dipole and Quadrupole Fields. *Journal of Geophysical Research (Space Physics)* **124**, 2844-2853. DOI: 10.1029/2018JA026164

- TSAREVA, O. O., DUBININ, E. M., MALOVA, H. V., POPOV, V. YU. & ZELENYI, L. M. 2020 Atmospheric escape from the Earth during geomagnetic reversal. *Annals of Geophysics (Physics of the Atmosphere)* **63** (2), PA222, DOI: 10.4401/ag-8354

ABSTRACT OF THE DISSERTATION

Temporal variability of the Earth's magnetic field and its influence on the near-Earth space environment

The Earth's magnetic field undergoes strong temporal variabilities with characteristic periods as short as ten seconds (magnetospheric substorms triggering the polar aurora) and as long as a million years (geomagnetic reversals). Its temporal variations, although of very different origin and characteristics, affect the dynamics of the near-Earth space environment.

The first part of this thesis is dedicated to the development of a new kinetic theory of instabilities in the magnetospheric tail which could explain the origin of substorms. Starting from a known theory of drift instabilities linked to the presence of a pressure gradient in the magnetotail, the proposed model includes trapped bouncing electrons which can enter into resonance with drift-Alfvén instability modes if the density gradient in the tail becomes large. Taking this the bouncing motion into account significantly increases the growth rate of this universal instability. To try to validate this new model, an example of an auroral observation by the THEMIS mission (February 3, 2008) was analyzed. This auroral activation seems to have been triggered by a sudden compression of the magnetospheric tail towards 10 R_E significantly increasing the pressure gradient and causing significant fluctuations in the magnetic field. The orders of magnitude of the period and the growth rate of these oscillations are compatible with the dispersion curves deduced from the theoretical model.

Second part of the thesis is devoted to changes in the radiation situation on Earth, the radiation belts and the terrestrial atmosphere during Earth's magnetic field reversal. We calculated the variations in galactic cosmic proton flux during a geomagnetic reversal to infer the radiation doses to which human population and astronauts could be exposed. The radiation background should increase by a factor of about three during the solar minimum period, and the elevated radiation regions should be redistributed and their areas will apparently increase due to the dipole field decrease, such radiation doses are not dangerous for humans and other living creatures. Classical Störmer theory was generalized to the case of an axisymmetric superposition of dipole and quadrupole fields. We identified the allowed and forbidden regions of particle motion, and also the capture regions, which ensure the stable existence of radiation belts. A key role in protecting earthly life from radiation belongs to the atmosphere. Therefore we considered basic mechanisms of atmospheric particle acceleration and estimated the escape rates of ionospheric ions (H^+ and O^+). According to our estimates, the escape rates of atmospheric particles during the geomagnetic field reversal will increase by 2.5 times, which will not greatly change the density of the atmosphere.

RÉSUMÉ DE THÈSE

Variabilité temporelle du champ magnétique terrestre et son influence sur l'environnement spatial proche

Le champ magnétique terrestre connaît une forte variabilité temporelle avec des périodes caractéristiques aussi courtes que la dizaine de secondes (sous-orages magnétosphériques responsables du déclenchement des aurores polaires) et aussi longues que le million d'années (inversions de la polarité nord-sud). Ses variations temporelles, bien que d'origine et de caractéristiques très différentes, affectent la dynamique de l'environnement spatial proche de la Terre: précipitation de particules dans la haute atmosphère, modification des flux de particules cosmiques, échappement atmosphérique.

La première partie de cette thèse est dédiée au développement d'une nouvelle théorie cinétique des instabilités dans la queue magnétosphérique qui pourrait expliquer l'origine des sous-orages. En partant d'une théorie connue des instabilités de dérive liées à la présence d'un gradient de pression dans la queue magnétosphérique, le modéle proposé dans cette thèse inclut le mouvement de rebond des électrons piégés dans le champ géomagnétique qui peuvent entrer en résonance avec les modes de dérive (drift-Alfvén instability) si le gradient de densité dans la queue devient important. La prise en compte de ce mouvement de rebond augmente significativement le taux de croissance de cette instabilité universelle. Pour tenter de valider ce nouveau modèle, un exemple d'observation aurorale par la mission THEMIS (3 février 2008) a été analysé. Cet événement a été choisi car il correspond à un arc auroral isolé observé à la fois par les caméras All-sky situées au sol et par les satellites THEMIS orbitant à 10 R_E. Cette activation aurorale semble bien avoir été déclenchée par une soudaine compression de la queue magnétosphérique vers 10 R_E augmentant sensiblement le gradient de pression et provoquant des fluctuations importantes du champ magnétique. Les ordres de grandeur de la période et du taux de croissance de ces oscillations sont compatibles avec les courbes de dispersion déduites du modèle théorique.

La deuxième partie de la thèse étudie l'influence du renversement des polarités du champ magnétique sur l'environnement radiatif de la Terre. En particulier, nous avons calculé les variations du flux de protons cosmiques lors d'une inversion géomagnétique pour déduire les doses de rayonnement auxquelles la population humaine et les astronautes pourraient être exposés. Le fond de rayonnement devrait augmenter d'un facteur d'environ trois pendant la période minimale solaire, et les régions de rayonnement élevées devraient être redistribuées et leurs zones augmenteraient apparemment en raison de la diminution du champ dipolaire, ces

doses de rayonnement ne sont pas dangereuses pour les humains et autres créatures vivantes. Dans le même temps, pour les astronautes à bord de l'ISS en orbite à 400 km au-dessus du sol, pendant une période d'inversion, une augmentation du rayonnement de 14 fois peut être dangereuse. Sans aucun doute, dans ce cas, une correction des orbites des véhicules spatiaux serait nécessaire. La théorie classique de Stormer a été généralisée au cas d'une superposition axisymétrique de champs dipolaires et quadripolaires. Nous avons identifié les régions autorisées et interdites de mouvement des particules, ainsi que les régions de capture, qui assurent l'existence stable des ceintures de rayonnement. Un rôle clé dans la protection de la vie terrestre contre les radiations appartient à l'atmosphère. Par conséquent, nous avons considéré les mécanismes de base de l'accélération des particules atmosphériques et estimé les taux d'échappement des ions ionosphériques (H^+ et O^+). Selon nos estimations, les taux de fuite des particules atmosphériques lors de l'inversion du champ géomagnétique augmenteront de 2,5 fois, ce qui ne modifiera pas considérablement la densité de l'atmosphère.